Quantitative automated analysis of host-pathogen interactions

Dissertation

in Partial Fulfilment of the Requirements for the Degree of

"Doctor of Philosophy" (PhD)

Submitted to the Council of the Faculty of Biological Sciences

of Friedrich Schiller University Jena

by Ivan Belyaev, MSc. in Physics

born on 23.05.1983 in Angarsk,

USSR

The dissertation was defended on December 16, 2022
at Leibniz Institute on Aging — Fritz Lipmann Institute (FLI), Jena.

Disputation committee chair:

Prof. Dr. Zhao-Qi Wang, Leibniz Institute on Aging — Fritz Lipmann Institute (FLI), Jena.

Reviewers:

1. Prof. Dr. Marc Thilo Figge, Leibniz Institute for Natural Product Research and Infection Biology — Hans Knöll Institute, Jena.
2. Prof. Dr. Oliver Kurzai, Institute for Hygiene and Microbiology, Julius Maximilians University, Würzburg.
3. Prof. Dr. Matthias Gunzer, Institute of Experimental Immunology and Imaging at University Hospital, Essen.

Table of contents

Abbreviations 5

1 Introduction 7

1.1 Fungi and their pathogenicity 7

1.1.1 *Candida albicans* and *Candida glabrata* 11

1.1.2 *Aspergillus fumigatus* 11

1.2 Elements of antifungal host defence 12

1.3 Microscopy 14

1.3.1 Optical microscopy 15

1.3.2 Electron microscopy 16

1.3.3 Biological staining 17

1.4 Imaging 17

1.5 Automated image analysis 19

1.6 Aims and objectives of this work 21

2 Overview of manuscripts 23

3 Manuscripts 27

3.1 Enhanced segmentation of label-free cells for automated migration and interaction tracking 27

3.2 Automated characterisation of neutrophil activation phenotypes in *ex vivo* human *Candida* blood infections 40

3.3 Human neutrophils produce antifungal extracellular vesicles against *Aspergillus fumigatus* 53

4 Discussion 73

4.1 *C. albicans* and *C. glabrata* alter neutrophil morphodynamics differently 73

4.1.1 Neutrophil segmentation and tracking 73

4.1.2 Analysis of neutrophil morphodynamics 75

4.2 Human neutrophils produce antifungal extracellular vesicles against *A. fumigatus* ... 77

5 Summary ... 79

6 Zusammenfassung ... 81

Bibliography ... 85

A – Bir ... 85

Bon – Con ... 86

Cse – Goo ... 87

Gor – Ing ... 88

Inv – Lan ... 89

Las – Mok ... 90

Mur – Pfe ... 91

Pic – Sil ... 92

Sta – Wor ... 93

Wor – Z ... 94

Declaration on honour ... 96

Acknowledgements ... 97

Appendix ... 99

Abbreviations

2D — spatial two dimensional

3D — spatial three dimensional

ages — antifungal extracellular vesicles

AIA — automated image analysis

EVs — extracellular vesicles

Fovea — field of view

IFD — invasive fungal disease

IFI — invasive fungal infection

syn. — synonym

WHO — World Health Organization

Names of diseases are given according to the International Classification of Diseases, Tenth Revision (ICD-10, (World Health Organization (WHO) 1994)).

1 Introduction

Profound understanding of host-pathogen interaction is the cornerstone of proper disease diagnostics, cure and prevention. Alongside molecular mechanisms of such interrelationships, the spatiotemporal characteristics (*e.g.* cell growth, morphology, mutual positioning of interacting components) of undergoing processes are often in focus of interest. The standard way to acquire such information is microscopy imaging followed by quantitative image analysis. During the last century, a plethora of methods and techniques were invented to serve this need. Yet, there are many challenges due to the high diversity of biological objects and a broad spectrum of questions that might be being asked.

The current thesis represents an application of quantitative image analysis methods to biological problems. The scope of the investigations is quantitative measurements of effects that appear during or after interaction between some of the cellular components of the innate immune system and pathogenic fungi of a few species.

This chapter is organised as follows: Sections 1.1 and 1.2 briefly introduces the biological background and motivation of the topic of this thesis. The section describes fungi, their pathogenicity and neutrophils as the component of the antifungal immune response. Sections 1.3–1.5 shed light on bioimaging techniques used in this work, covering microscopy, biological labelling, image acquisition and automated image analysis (AIA).

1.1 Fungi and their pathogenicity

The fungal kingdom comprises a few million species (a proper estimation is a topic of discussion, see (Hawksworth and Lücking, 2017)) widely distributed in the environment, among which several hundreds of species are considered to be pathogenic for humans (Fisher *et al.,* 2016), causing different types of diseases — mycoses. The estimated burden of mycoses to the global human population is varying wildly in the number of cases and severity (Bongomin *et al.,* 2017): from mild chronic diseases of the hair, nail and skin affecting about one billion people to severe life-threatening conditions (invasive fungal diseases, IFDs) with high mortality (well above 30%, (Logan *et al.,* 2020)) caused by invasive fungal infections (IFIs) acquired by a few millions of people annually.

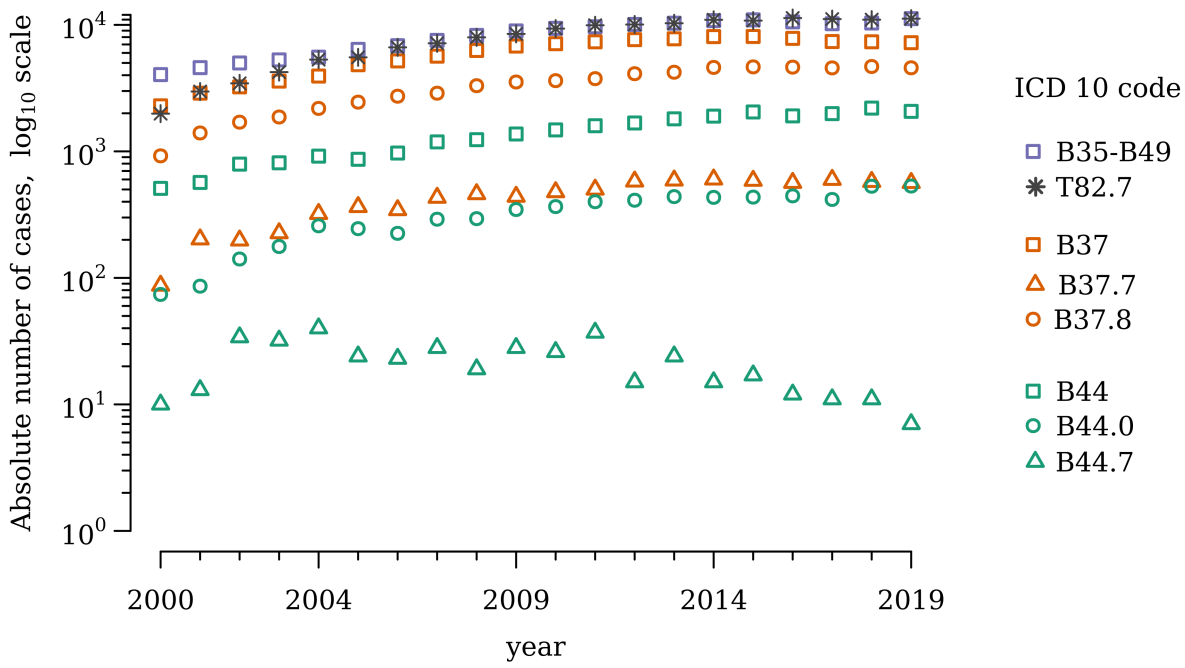

Fig. 1.1. Dynamics of some mycoses in Germany for the period 2000–2019. The ICD 10 code transcript: B35–B49 Mycoses, B37 Candidiasis, B37.8 Candidiasis of other sites, B37.7 Candidal sepsis, B44 Aspergillosis, B44.0 Invasive pulmonary aspergillosis, B44.7 Disseminated aspergillosis, T82.7 Infection and inflammatory reaction due to other cardiac and vascular devices, implants and grafts. Data acquired from the database of German Federal Health Monitoring System (Das Informationssystem der Gesundheitsberichterstattung des Bundes) located at the web-portal https://www.gbe-bund.de/, [Home > Diseases/Health Problems > Diseases in General > Table (ad hoc): Diagnostic data of the hospitals by place of residence (ICD10-3-digits, from 2000), [accessed 2022 Mar 10]]

Paradoxically, the rising number of patients with IFD (*e.g.* trends in Germany represented in Fig. 1.1) is caused by advances in life-saving technologies because the predisposing factors leading to IFD include (Brown *et al.,* 2012; Enoch *et al.,* 2017) immunosuppressive therapy, which is necessary for patients with transplanted organs, and long-term use of broad spectrum antibiotics, affecting the equilibrium of the microbial flora. Also, prolonged hospitalisation and the usage of medical indwelling devices and central venous catheters further increase the risk of such infec-tions. For ins-tance, in Germany (see Fig. 1.1) the annual absolute number of candidal sepsis (B37.7) cases has the same tendency as the number of infection cases caused by indwelling devices (T82.7), the cause relation will be described in the further chapter. Another cohort at risk includes (Bongomin *et al.,* 2017) people with other immune deficiencies (innate, caused by HIV or chemotherapy) as well as hav-ing poorly controlled diabetes, tuberculosis, chronic obstructive pulmonary disease (COPD), asthma, cystic fibrosis, and, recently, patients with moderate/severe form of COVID-19 infection (Hughes et al., 2020; Casalini

et al., 2021; Nucci *et al.,* 2021; Basile *et al.,* 2022). Those factors vary between countries, regions, and even hospi-tals, which, alongside sophisticated diagnostic work-up, complicate control and cure of IFDs (von Lilienfeld-Toal *et al.,* 2019; Donnelly *et al.,* 2020; Lass-Flörll *et al.,* 2021).

Epidemiology of mycoses is complicated, partially due to persistent neglect of fungi as major pathogens by both the public and health authorities(Brown *et al.,* 2012; Fisher *et al.,* 2016; Almeida *et al.,* 2019; Rodrigues and Nosanchuk 2020), which leads to a lack of accurate statistics for some diseases. Such a problem persists even in well-developed countries like the Netherlands (Buil *et al.,* 2020) or Germany, where IFDs do not belong to the list of reportable infectious diseases (Ruhnke*et al.,* 2015; von Lilienfeld-Toal *et al.,* 2019)).

An additional aspect, which complicates the analysis of IFDs dynamics based on public data, is the absence of corresponding nosological units in the current Tenth revision of the International Classification of Diseases (ICD-10, (World Health Organization (WHO) 1994)). While some IFD names can be found in literature or health authorities' reports and guidelines, in the statistical data, it might be hidden in larger groups: *e.g.* invasive candidiasis could be reported as B37 Candidiasis or B37.8 Candidiasis of other sites. This situation will be improved with the introduction of a new version of this document (ICD-11, (World Health Organization (WHO) 2019)) into practice. For instance, as shown in the diagram for *Candida* infections in Fig. 1.2, IFDs were separated into independent categories. It will improve the quality of health information and reflect excellent advances made in under-standing fungal diseases fundamentals (Salazar and Brown 2018a) alongside accumulated clinical practice and improved diagnostics(Consortium OPATHY and Gabaldón 2019).

According to standard criteria (Donnelly*et al.,* 2020), an IFD is confirmed when at least one of the following conditions is met:

- a presence of fungal cells or hyphae accompanied by evidence of associated tissue damage are seen during microscopic examination of a patient's sterile, under health condition, tissue specimen;
- the infectious agent is recovered by culture from such tissue or blood;
- the infectious agent is detected by serological diagnostics;
- the infectious agent is detected by tissue nucleic acid diagnostics.

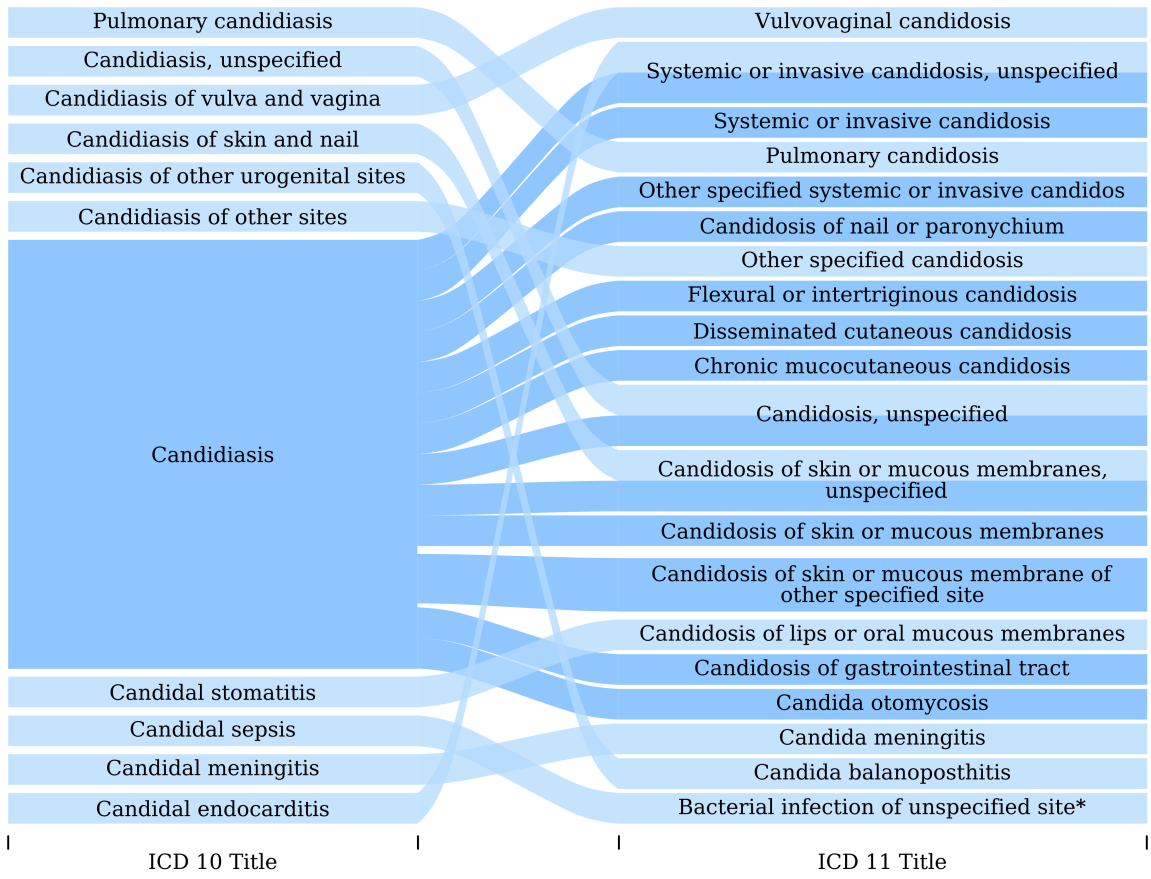

Fig. 1.2. A comparison of nomenclatures of *Candida* infections in two consequent versions of International Classification of Diseases (ICD). * stands for 'not limited by *Candida*'. The diagram is based on information from ICD 10 / ICD 11 mapping tables located at: https://icd.who.int/browse11/Downloads/Download?fileName=mapping.zip

In conjunction with host factors and clinical features, those indicators are recommended to use in clinical trials, epidemiologic studies, and the evaluation of diagnostic tests.

An IFD starts after a successful fungal invasion. To establish IFI, a fungus must fulfil the four criteria (Köhler*et al.,* 2017): thermal resistance at human body temperature, locomotion through or ability to circumvent host defence barriers, lysis and absorption of human tissues, and resistance to immune response. Only a tiny fraction of fungal species has developed this combination. However, this minor group from the kingdom *Fungi* have become a major threat for the immunocompromised people.

The objectives of the current work are associated with three pathogenic fungal species with different biology that have the most significant contribution to the number of IFD cases.

1.1.1 *Candida albicans* and *Candida glabrata*

Candida is a genus of yeasts from the *Ascomycota* phylum and the leading cause of IFD. Most of the invasive candidiasis (~ 65%–75%, varying is region-dependent) are associated with *C. albicans* and *C. glabrata* . Both species are harmless commensals of healthy humans but turn pathogenic once local or systemic host defence defects occur.

For both fungi, the infection process starts from adhesion to host cells by ex-pressing specific adhesins (Brunke and Hube 2013). After attachment, the next step in *Candida* pathogenesis is invasion, typically into epithelial cell layers and then into the deepest tissues and bloodstream. For *C. albicans,* invasion can occur via two mechanisms: induced endocytosis by host cells or active penetration by fungus hyphae using physical forces and biologically active compounds, which is considered the dominant route of invasion for this specie. In contras,t *C. glabrata* grows typically only in the yeast form. A possible route to reach the bloodstream is the accidental or iatrogenic breach of natural barriers via trauma, catheters, surgery or parenteral nutrition. Also, there is a difference in the nutrition process: *C. albicans* can consume a broader range of compounds than *C. glabrata* and can more effectively counteract a decay of avai-lable micronutrients, which the host actively limits during infections. Such plasticity allows *C. albicans* to successfully colonise many different and changing host niches, while *C. glabrata* is striving for a more stable environment. In addition, biological and eco-logical differences of these species could manifest in their interactions with the human immune system (Duggan *et al.,* 2015; Johnson *et al.,* 2016, 2017).

1.1.2 *Aspergillus fumigatus*

Another group from the *Ascomycota* phylum, which is capable of infecting hu-mans, is composed of *Aspergillus* species. These species cause a broad spectrum of diseases in humans: from allergies to highly aggressive invasive aspergillosis (Latgé 1999). Most cases of that severe IFD[1] is caused by only single specie — *A. fumigatus* — a ubiquitous soil-dwelling saprophyte, which utilises humans as only an incidental substrate on which is possible to grow. The most common entrance of this infectious agent is epithelia of the respiratory tract since *A. fumigatus* relies on air currents when disseminating spores (conidia).

[1]The burden on the global human population is conservatively estimated as more than 3×10^5 cases annually with a mortality rate 30%–80% (Bongomin *et al.,* 2017).

Conidia of *A. fumigatus* native (wild) form are pigmented and echinulate sphe-roidal structures of 2–3 μm in diameter (Latgé 1999), which are present in indoor and outdoor environments at concentrations ranging between 1 and 100 conidia per m^3 but can reach up to 4×10^7 conidia per m^3 in aerosols from composting facilities (Wéry 2014). The average person is estimated to inhale between ~ 10^2 and ~ 10^4 of the conidia each day (Köhler *et al.,* 2017). Like most other aerosol particles from inhalable air, the majority of the inhaled conidia are captured in the mucus and washed out of the respiratory tract through the mucous epithelium's ciliary action. The remaining conidia would be phagocytosed by epithelial cells or tissue-resident phagocytic im-mune cells (predominantly macrophages). Conidia that escaped clearance start swelling, followed by germination on the epithelial surface, which triggers a host danger response pathway mediated by the release of antimicrobial effectors and alarmins to initiate inflammatory responses and timely neutrophil recruitment (Latgé and Chamilos 2019), which will eliminate hyphae. The outcome of this pro-cess depends on the human immune status.

The success of the fungal invasion and growth in a susceptible host is associated with several properties of A. fumigatus, which it has developed to survive in a harsh soil environment (Köhler et al., 2017). First off, this fungus is well-adapted to high temperatures (above 40 °C) and can decompose and digest human body tissues. Then, thigmotropism, the ability to sense and follow contours, and the ability of hyphae to survive fragmentation pave the way for angioinvasion and dissemination to highly perfused organs, including the brain, the eyes and the kidneys. Another component of success is the ability of A. fumi-gatus to mediate a human immune response (Stanzani et al., 2005) using defensive toxins, which evolutionary developed to counteract protozoans, as well as melanins (pyomelanin and 1,8-dihydroxynaphthalene (syn. DHN) melanin), with which that fungus coats its conidia for protecting from sunlight and oxidative stress.

1.2 Elements of antifungal host defence

The bodies of vertebrates are protected from infectious agents, their toxins, and the damage they cause, by barrier tissues and immune system, composed of various effector cells and molecules (Murphy and Weaver 2016). The scope of the present work is constrained by the most numerous and significant effector cell population involved in the control of many fungal infections (Salazar and Brown, 2018) — polymorphonuclear neutrophilic granulocytes (neutrophils, (Murphy and Weaver, 2016)). These are the relatively

short-leaving, highly mobile phagocytic cells of leukocytes myeloid lineage, which are abundant in the bloodstream and, according to recent discoveries (Nicolás-Ávila *et al.,* 2017; Hidalgo *et al.,* 2019), resident at varying numbers in other healthy, not only hematopoietic, tissues. Along with other tissue-resident immune cells and epithelial cells, such tissue-resident neutrophils contribute to the most immediate immune reaction. The latest part of that is recruiting other immune cells by secreting cytokines and chemokines that trigger those recruiters' extravasation from vicinal blood vessels and attract them to the infection site (Murphy and Weaver 2016).

To combat pathogens, the neutrophils' antimicrobial armamentarium, in addition to phagocytosis, includes several other components: reactive oxygen species, antimicrobial peptides, extracellular vesicles (EVs) and neutrophil extracellular traps (NETs) (Brinkmann *et al.,* 2004; Urban *et al.,* 2006; Amulic *et al.,* 2012; Kolaczkowska and Kubes 2013; Johnson *et al.,* 2017; Allen *et al.,* 2020). While most listed entities are used by neutrophils specifically for pathogen elimination, the functions of EVs — a heterogeneous group of cell-derived, lipid-bilayer-enclosed particles (Russell *et al.,* 2019) — are more diverse and not associated with immune response only. Such particles are released by cells of prokaryotic and eukaryotic organisms for removing waste products from the cell, sharing nutrition, carrying and transferring bioactive molecules and information, both intercellular and inter-organismal.

According to the current consensus, EVs can be classified into two distinct classes, determined by two major sites of EVs biogenesis (Van Niel *et al.,* 2018; Russell *et al.,* 2019): exosomes, which originated from the endosomal system, and microvesicles (or ectosomes), shed directly from the plasma membrane. Depending on the parent cell type and state, EVs will display a set of cell-type-specific proteins that account for their specific fates and functions (Van Niel *et al.,* 2018; Russell *et al.,* 2019). For instance, unstimulated neutrophils release spontaneous EVs with anti-inflammatory effects, while the presence of pathogens or their metabolites induces the production of pro-inflammatory EVs loaded with antimicrobial compounds (Kolonics *et al.,* 2020). However, EVs' phenotype-function interconnections, especially the molecular cargos responsible for specific antimicrobial actions of EVs during infection, remain poorly described (Russell *et al.,* 2019; Brakhage *et al.,* 2021).

The strategy of neutrophils response is orchestrated by biochemical and physical cues that deliver information about the properties of confronted pathogen and the surrounding microenvironment (Huse 2017; Ley *et al.,* 2018). However, during millions of years of co-evolution, some pathogens, particularly fungi, have

developed mechanisms of reducing or even evading immune response (Maza*et al.,* 2017; Kernien*et al.,* 2020). To uncover spatiotemporal aspects of this complex host-pathogen interplay, a microscopy examination is required.

1.3 Microscopy

Microscopy is the broad class of instruments and methods used in multiple fields of biology and medicine, which allow acquiring information about biological objects in a wide range of scales from ~1 mm up to ≈1.5 Å (Kato *et al.,* 2019). The goal of a microscopy procedure is to form an image of an object of interest with increased size, resolved minute specimen details, and the contrast that is sufficient to render the specimen visible to the detector[2] (Murphy *et al.,* 2022). Consequently, the resulting image quality can be characterised via magnification and resolution. The third fundamental characteristic of an image — contrast — describes a difference in luminance or colour between an object of interest and its immediate background, *i.e.* any entities surrounding that object. The influence of those characteristics is illustrated in Fig. 1.3.

The choice of the appropriate microscopy technique is determined by the object's properties and the type of information that needs to be captured. Two major groups of those techniques are most frequently used to investigate a host-pathogen interaction on a cellular and sub-cellular level.

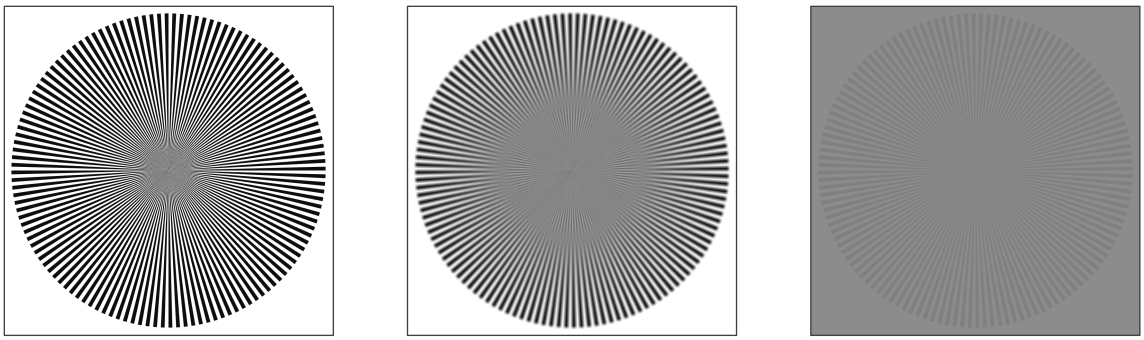

a) b) c)

Fig. 1.3. A synthetic illustration of the influence of optical instrument characteristics on the acquired image. a) The image acquired with an instrument with high spatial resolution and contrast. b) The image acquired with the same magnification as a) but with a lower spatial resolution, resulting in image blurring. c) The image acquired with lower contrast. The Siemens star pattern was generated using the code by Hans Strasburger located at [accessed 2022 Mar 10]: http://hans-strasburger.userweb.mwn.de/siemens_star.html

[2] a digital or analogue camera, or the human eye

1.3.1 Optical microscopy

Optical microscopy (OM), also referred to as light microscopy, utilises electro-magnetic waves of the visible spectrum (visible light) and their ability to interact with a specimen through various mechanisms: reflection from the surface, absorption, refraction, polarisation, diffraction and fluorescence. This family of microscopy has several branches.

The transmitted light microscopy with brightfield illumination is historically the first microscopy technique, which has been widely used for the last three centuries for investigations in the microworld. It is suitable for observing specimens that alter the transmitted light by adsorption/reflection. However, in many cases, there is a negligible difference in light absorption between objects of interest and their sur-rounding environment, *e.g.* living cells and nutrient medium, or their intracellular components and plasma membranes, which makes these entities barely detectable and observers can only rely on scattered light.

At the same time, there always exist relative phase shifts among light waves governed by refractive index differences between parts of the observed specimen. This information can be captured by polarised light microscopy, which converts such a shift to brightness changes in the rendered image. There are two most common techniques which serve this purpose: phase contrast (PhC, (Zernike 1938, 1942)) and differential interference contrast microscopy (DIC, (Nomarski 1955, 1960; Allen *et al.,* 1969)). PhC microscopy produces image intensity values that vary as a function of the speci-men's optical path length magnitude, whereas DIC utilises optical path length gradi-ents for contrast rendering. A primary advantage of DIC over PhC is utilising the instrument at the full numerical aperture, producing images without the ‘halo’ effect, and improved axial resolution (Lang 1971; Murphy and Davidson 2012b). In addition, it allows performing optical sectioning.

However, in many cases, information acquired with transmitted light techniques is not enough. To grasp information about the spatial localisation of a specific type of molecule, a fluorescence — the ability of some molecules, not necessarily molecules of interest, to absorb and subsequently reradiate light — can be employed. Fluores-cence microscopy (FM) is the largest and most intensively developing branch of OM techniques. It has become an essential tool in biology and the biomedical sciences. The most significant part of FM comprehends super-resolution techniques, which allow optical imaging with resolution beyond the diffraction limit. Some of them can reveal the presence of a single molecule or even resolve sub-molecular structures (e.g. (Weisenburger et al., 2017)). Here it is necessary

to mention that with any of such techniques, a direct image observation is not possible; it requires a detector and a computer to synthesise an image. All fluorescence methods require the presence of synthetic or naturally occurring in the specimen target-specific fluorescent molecules[3] with a high quantum yield[4], known spectra of absorption[5] and reradiation[6] (Murphy and Davidson 2012a).

1.3.2 Electron microscopy

A plethora of optical microscopy techniques have been developed to shed light on the microworld. However, light is not the only possible carrier of information about a specimen. To acquire information from the scales beyond what can be attained with light, different electron microscopy (EM) techniques can be used. There are two major ones.

Transmission electron microscopy (TEM) is a microscopy technique where an image is formed from the interaction (absorption, scattering, polarisation, diffrac-tion) of the electrons with the sample as the beam is transmitted through the specimen. There are many TEM variations that differ in image contrast formation. These techniques cover a broad range of magnification from $\sim 10^2$ to $\sim 10^6$ with resolution up to 1.5 Å in a case with cryogenic transmission electron microscopy (cryoTEM, (Kato *et al.,* 2019)), which allows studying not only subcellular components but also perform *in situ* analysis of biological macromolecules (*e.g.* membrane proteins) and reveal their structure.

Another technique is scanning electron microscopy (SEM), which uses a focused beam of electrons and scans the surface in a raster scan pattern. The energy exchange between the electron beam and the specimen results in a three-component response, composed of high-energy reflected electrons, emitted secondary low-energy electrons and emitted electromagnetic radiation, each of which can be detected independently. The resulting image is a map of a signal's intensity detected in the raster's nodes, *i.e.* topographical map of the surface. This opens the possibility of reconstructing a relief of scanned surface (Mignot 2018). With this technique it is possible to achieve a resolution higher than 1 nm.

In biological applications for most techniques, sample fixation and staining with heavy metals are necessary. For TEM, it is also required to have ultra-thin (0.1 μm) slices of the analysed specimen.

---

[3] termed fluorophores or fluorochromes

[4] defined as the ratio of photon absorption to emission

[5] syn. excitation

[6] syn. emission

1.3.3 Biological staining

Biological staining is a procedure of some biological specimen entity (anything from an ion to a tissue) labelling by attaching or depositing in its vicinity a marker with specific property (Richard W. Dapson *et al.,* 2021). It is commonly a chromo-genic agent (*e.g.* dye, fluorophore, pigment) for an OM or heavy metal particles (atoms, nanoparticles) for an EM. The purpose of biological staining is the contrast enhancement of target entities.

The staining procedure and used compounds are always task- and target-specific. During that procedure design and application, several aspects must be considered. First off, the degree to which a target entity is stained compared with non-target adjacent structures (selectivity) and the degree to which a staining procedure allows to detect of small amounts of a target component (sensitivity) (Horobin 2002; Richard W. Dapson *et al.,* 2021). While physico-chemical properties of interacting molecules only determine selectivity of staining, its sensitivity is inex-tricably linked with a chosen imaging technique. Nevertheless, both characteristics can be adjusted during the staining process (Horobin 2002). Another group of factors related to living samples stained with fluoro-chromes. It is the cytotoxicity of stains and the photocytotoxicity of some fluorescent re-porters, which tend to react with molecular oxygen to produce free radicals that can damage the chemical structure and alter biological functions of proximal biomolecules after photoexcitation (Dixit and Cyr 2003; Jensen 2012; Birch*et al.,* 2017; Cavaco*et al.,* 2020). These effects disrupt cell functions or even induce cell death during the imaging process. Additional altering factors can be cell receptors' occupation by antibodies used for immunostaining (Cseresnyes et al., 2020). All this necessitates further development of label-free imaging techniques and appropriate method of image analysis.

1.4 Imaging

To document and further numerical analysis, an optical image formed by an optical system of a microscope needs to be captured. Nowadays, different digital detectors are used for this purpose. In the simplest case of an achromatic detector, a detected two-dimensional (2D) digital image can be considered as the rectangular matrix of size $M \times N$, which contains the result of discretisa-tion and quantisation of intensity of the optical image (Gonzalez and Woods, 2018). The number of elements in that matrix (called pixels) is defined in the

discretisation process and depends either on the number of possible positions of a sensor (number of raster mesh nodes) in case of detection by a single sensor, or the number of possible positions and number of sensors in case of a sensor strip array, or the number of sensors in the 2D detector array. This parameter contributes to the spatial resolution of the acquired image (see Fig. 1.4).

A single sensor delivers an analogue response signal carrying brightness information. To represent it in a digital form a quantisation is required. During this process, input analogue (continues) values from a sensor are mapped to output values in a finite discrete set of non-negative integer values that typically contains $L = 2^k$ equally spaced elements with values in $\{0, ..., L - 1\}$. This parameter defines brightness resolution — the possibility to detect the lowest difference in brightness between two spots.

An image, pixels of which can have up to 2^k levels of brightness, is called 'k-bit image'. This number is defined by the detector's analogue-to-digital converter (ADC) architecture. Often, 8-bit or 16-bit representation is used; however, the chosen range can be utilised only partially (*e. g.,* for a 12-bit output of ADC, a 16-bit representation will be used). It is evident that the highest bit representation allows achieving better brightness resolution, higher signal to noise ratio (which is essential for fluorescent imaging) and provides more flexibility for image processing operations.

To study spatial properties of biological objects in three dimensions, 2D imaging techniques in conjunction with optical cross-section are used. Another irreplaceable method for studying processes in live systems is time-lapse imaging, where image acquisition is performed with any of the above-mentioned OM methods

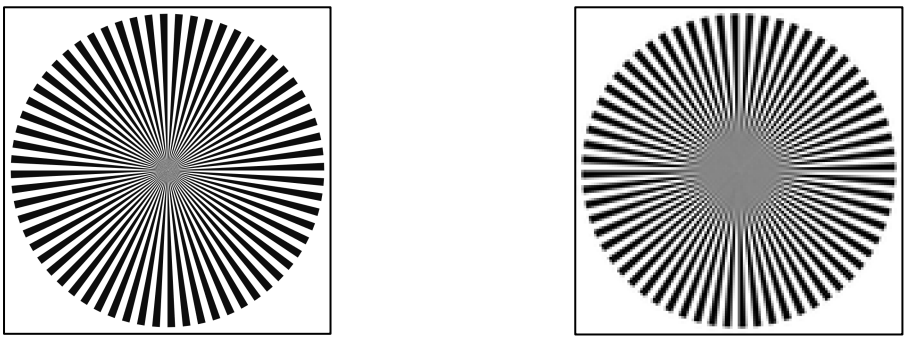

a) b)

Fig. 1.4. A synthetic illustration of the influence of detector resolution. a) The image acquired using a detector with a resolution matched the optical resolution of the microscope. b) The image acquired with the same magnification as a) but using a low-resolution detector.

at regular time intervals. The time step is usually defined by kinetic of observing the process and must, according to the sampling theorem[7] and Nyquist's discovery (Nyquist interval), be at least two times shorter than characteristic time after which changes in observing system can be detected.

1.5 Automated image analysis

Automated image analysis (AIA) has become an irreplaceable toolkit in biolog-ical research, especially for high throughput experiments. Most often, AIA aiming entities attribution (classification), localisation, counting, measurement and temporal characterisation. In comparison with a human operator, it allows to extract meaningful information from imaging data much faster, with high consistency and without operator errors, *i.e.* once an algorithm is designed, its output does not depend on operator experience. However, in most cases, AIA designed in assumption that uniformity of imaging procedures has been maintained between experiments and all possible mistakes during image acquisition were avoided (North 2006).

A generic AIA workflow algorithm is composed of the following core operational blocks: (i) image pre-processing, (ii) objects segmentation and, if necessary, tracking, (iii) features extraction, and (iv) analysis. Depending on the task and used approach, some blocks can be omitted or merged into one. Considering the diversity of such studies, further description will be constrained by cell and cell population analysis.

The purpose of pre-processing (i) is the transformation of an image in such a way that the resulting image is more suitable than the raw one for further processing. These operations may include noise reduction, contrast enhancement, illumination cor-rection, image sharpening and deconvolution, which is particularly important in the case of fluorescence images.

The segmentation (ii) partitions an image into individual objects (cells/sub-cellular components and background). Additionally, a tracking procedure can be employed if temporal changes in detected objects are to be investigated. To perform any analysis, segmented cells needs to be described (iii) in some way.

Depending on the purpose of analysis and cell peculiarities, such a description (feature space) may include information about cell shape, pixels colour/ spectral composition and/or their distribution patterns, texture, structural or surro-

[7] widely known as the Whittaker–Kotel'nikov–Shannon theorem (Meijering 2002)

unding elements (membrane, nuclei etc.). In case of cellular motility phenotyping or morphodynamic analysis a tracking data must be used.

In the most straightforward, trajectory-focused, approach only coordinates of segmented cell centroids are used to perform cell motility phenotyping via cellular trajectories description or migration speed distribution (*e.g.* (Beltman *et al.,* 2009; Mokhtari *et al.,* 2013; Letendre *et al.,* 2015; Svenssون*et al.,* 2018)).

In a more advanced, morphology-focused approach (Held *et al.,* 2010; Driscoll *et al.,* 2011; Gordonov *et al.,* 2016), for each segmented cell and at each time point, morphological features are extracted based on which a morphological state is identified. After feature extraction the subsequent temporal analysis is performed. Such an analysis usually assumes that cell morphology dictates by distinct cellular states and then investigate how the morphological states evolve (*e.g.* cellular morphodynamics in mi-tosis). The morphology-focused feature extraction could be performed considering a cell as a whole object or utilises descriptors of subcellular component movement, *e.g.* plasma membrane (Machacek and Danuser 2006; Tsygankov *et al.,* 2014; Barry *et al.,* 2015; Ma *et al.,* 2018; Imoto *et al.,* 2021), which can raise amount of information about intracellular processes available for the analysis. However, such detailed description is hardly suitable for use in high-throughput live cell experiments where tens or hundreds of cells need to be imaged simultaneously, because this approach requires imaging with a high magnification as well as a high spatial and temporal resolution, which would permit accurate detection of subcellular components.

While trajectory-focused or morphology-focused analysis operates with individual cells, the third approach is focused on description of cell population as a single object which evolving over the time (e.g. (Taylor et al., 2013)).

Based on extracted features, a cell population can be analysed (iv). In most cases, the analysis can follow either of three ways. The first one, exploratory analysis, is used to reveal the cell population's structure by identifying a group of cells (data clustering) that are similar in some sense, followed by identification of biologically relevant basis for their similarities within detected clusters and divergence between them. The second scenario implies a quantitative comparison of morphological cell characteristics in popu-

populations under different experimental conditions. The third way lies in detecting specific predefined phenotypes (i.e. classification) joint with statistical analysis of detected groups. Generally, the AIA workflow algorithm design is heuristic, and a certain amount of trials and errors usually is required before a variant, which yields acceptable results, is selected. A vigorously growing since 1960th multitude of image processing and computer vision algorithms (Gonzalez and Woods 2018), making the choice of basic algorithms and methods, which would be used for a particular problem solving, largely subjective. Nowadays, researchers often tend to choose deep-neural-networks-based approaches (Goodfellow *et al.,* 2016), which are shown to be quite effective in clas-sification (or labelling) problems and implemented in some ready-to-use tools designed explicitly for biomedical images (*e.g.* CellPose (Stringer *et al.,* 2021), InstantDL (Waibel *et al.,* 2021)). However, despite the favour of researchers acquired by those techniques, the classical image analysis and computer vision algorithms are still in demand for at least exploratory or comparative analysis based on interpretable des-criptors (*e.g.* a comparison of morphology between cell populations).

1.6 Aims and objectives of this work

This work aims to broaden knowledge about the neutrophil biology in their interaction with fungi species that most frequently causes IFDs. The questions that were addressed include the alteration of neutrophil morphology after interaction with *Candida* fungi (see Chapter 1.1.1), revealing factors which modulate the production and composition of neutrophil-derived EVs (see Chapter 1.2) and analysing their activity against *A. fumigatus* (see Chapter 1.1.2). Alongside fundamental interests, those questions have important applied aspects in the medicine of IFD. In particular, for diagnostic purposes and infection process monitoring.

The objectives of this work include the acquisition of quantitative evidence of different changes in neutrophils morphodynamics after interaction with *C. albicans* or *C. glabrata* and their metabolites in whole blood infection assay. Another part of the work is devoted to the quantitative analysis of the influence of neutrophil-derived extracellular vesicles (EVs) on the deve-lopment of *A. fumigatus* hyphae and their interaction with developed hyphae.

The objectives of this work were achieved by:

1. the development of effective segmentation and tracking algorithm which is capable of working with low-contrast cell images, produces accurate cell contours and provides data about positions of clusters, which would improve further analysis;
2. the development of a new stack of evaluation procedures to demonstrate the effectiveness of segmentation and tracking algorithm in nuances;
3. the development of novel workflow algorithm for analysis of neutrophil continuous morphological spectrum without consensus-based manual annotation;
4. the development of an algorithm for analysis of *A. fumigatus* hyphae growth using 2D transmitted light microscopy data;
5. the spatial analysis of the interaction of EVs with *A. fumigatus* hyphae based on 4D (spatial coordinates and colour) microscopy data.

2 Overview of manuscripts

Received: 23 March 2021 | Accepted: 25 May 2021
DOI: 10.1002/cyto.a.24466

COMPUTATIONAL ARTICLE

ISAC CYTOMETRY Journal of Quantitative Cell Science PART A

Enhanced segmentation of label-free cells for automated migration and interaction tracking

Ivan Belyaev[1,2] | Jan-Philipp Praetorius[1,2] | Anna Medyukhina[1,3] | Marc Thilo Figge[1,4]

Status

Published in Cytometry Part A, 2021; 99: 1218–1229.

Summary

We present a fully revised version of our algorithm for migration and interac-tion tracking (AMIT), which includes a novel segmentation approach and a new cluster detection and splitting method. We demonstrate that it can detect almost all cells within the field of view and provides accurate splitting of transient clusters in label-free time-lapse microscopy data. Furthermore, the substantially improved ex-traction of cell migration information by the revised version of AMIT is more than two orders of magnitude faster than the previous implementation, which makes it feasible to process time-lapse microscopy data at higher spatial and temporal resolutions.

Computational and Structural Biotechnology Journal 20 (2022) 2297–2308

ELSEVIER

COMPUTATIONAL ANDSTRUCTURAL BIOTECHNOLOGY JOURNAL

journal homepage: www.elsevier.com/locate/csbj

Automated characterisation of neutrophil activation phenotypes in *ex vivo* human *Candida* blood infections

Ivan Belyaev [a,b,1], Alessandra Marolda [c,1], Jan-Philipp Praetorius [a,b], Arjun Sarkar [a,b], Anna Medyukhina [a,d], Kerstin Hünniger [c,e], Oliver Kurzai [c,e,f,*,2], Marc Thilo Figge [a,g,*,2]

Status

Published in Computational and Structural Biotechnology Journal, 2022; 20: 2297-2708.

Summary

In this feasibility study, we presented a method for the quantitative assessment of static and dynamic changes in external morphology of neutrophils that have been exposed to pathogens or their metabolites based on label-free time-lapse microscopy data. As the model system, we used *in vitro* whole blood infection assay with *C. albicans* and *C. glabrata* as infectious agents. The method utilises a 1-class classifier as the novelty detector, which allows identifying cells in an infected sample which differ from cells in non-infected (mock) samples. Then we demonstrated that using this information it is possible to identify infection scenarios for *C. albicans* and *C. glabrata* with accuracies well above 75%, while the accuracy of identifying mock-infected samples reached 100%.

AMERICAN SOCIETY FOR MICROBIOLOGY | mBio®

RESEARCH ARTICLE
Host-Microbe Biology

Human Neutrophils Produce Antifungal Extracellular Vesicles against *Aspergillus fumigatus*

Iordana A. Shopova,[a,b] Ivan Belyaev,[c,i] Prasad Dasari,[d] Susanne Jahreis,[e] Maria C. Stroe,[a,b] Zoltán Cseresnyés,[c] Ann-Kathrin Zimmermann,[a,b] Anna Medyukhina,[c] Carl-Magnus Svensson,[c] Thomas Krüger,[b] Viktória Szeifert,[f] Sandor Nietzsche,[g] Theresia Conrad,[h] Matthew G. Blango,[b] Olaf Kniemeyer,[b] Marie von Lilienfeld-Toal,[e] Peter F. Zipfel,[a,d] Erzsébet Ligeti,[f] Marc Thilo Figge,[a,c] Axel A. Brakhage[a,b]

Status

Published in mBio, 2020; Vol. 11, Issue 2, e00596-20.

Summary

Here we provide the first *ex vivo* insights into neutrophil-derived extracellular vesicle formation by human neutrophils confronted with the *A. fumigatus*. We uncover a novel role of the conidial pigment DHN melanin in the modulation of the kinetics of the release and the protein cargo of neutrophil-derived EVs secreted by neutrophils in response to *A. fumigatus* presence. We demonstrate that these EVs are enriched in antimicrobial peptides and exhibit dose- and strain-dependent fungistatic effects via inhibiting the hyphal growth and promoting cell damage by delivering antifungal cargo.

3 Manuscripts

3.1 Enhanced segmentation of label-free cells for automated migration and interaction tracking

FORMULAR 1

Manuskript Nr. (laufende Nummer in der Dissertation) **1**

Titel des Manuskriptes: Enhanced segmentation of label-free cells for automated migration and interaction tracking.

Autoren: Belyaev I., Praetorius J.-P., Medyukhina A., Figge M.T.

Bibliographische Informationen (falls publiziert oder zur Publikation angenommen: Zitat):

Cytom Part A, 2021; 99(12): 1218–29. DOI: 10.1002/cyto.a.24466

Der Kandidat / Die Kandidatin ist (bitte ankreuzen)

☐ Erstautor/-in, ☒ Ko-Erstautor/-in, ☐ Korresp. Autor/-in, ☐ Koautor/-in.

Status (falls nicht publiziert; „zur Publikation eingereicht“, „in Vorbereitung“):

Anteile (in %) der Autoren / der Autorinnen an der Publikation (anzugeben ab 20%)

Autor/-in	**Konzeptionell**	**Datenanalyse**	**Experimentell**	**Verfassen des Manuskriptes**	**Bereitstellung von Material**
Belyaev I.	50	50	40	35	0
Praetorius J.-P.	30	50	60	35	0
Medyukhina A.	10	0	0	10	0
Figge M.T.	10	0	0	20	100
Total:	100	100	100	100	100

Received: 23 March 2021 | Accepted: 25 May 2021
DOI: 10.1002/cyto.a.24466

COMPUTATIONAL ARTICLE

ISAC CYTOMETRY Journal of Quantitative Cell Science PART A

Enhanced segmentation of label-free cells for automated migration and interaction tracking

Ivan Belyaev[1,2] | Jan-Philipp Praetorius[1,2] | Anna Medyukhina[1,3] | Marc Thilo Figge[1,4]

[1]Applied Systems Biology, Leibniz Institute for Natural Product Research and Infection Biology – Hans Knöll Institute (HKI), Jena, Germany

[2]Faculty of Biological Sciences, Friedrich Schiller University Jena, Jena, Germany

[3]Center for Bioimage Informatics, St. Jude Children's Research Hospital, Memphis, Tennessee, USA

[4]Institute of Microbiology, Faculty of Biological Sciences, Friedrich Schiller University Jena, Jena, Germany

Correspondence
Marc Thilo Figge, Applied Systems Biology, Leibniz Institute for Natural Product Research and Infection Biology – Hans Knöll Institute (HKI), Jena, Germany.
Email: thilo.figge@leibniz-hki.de

Funding information
CRC/TR 124 FungiNet, Grant/Award Number: 210879364; Leibniz ScienceCampus InfectoOptics

Abstract

In biomedical research, the migration behavior of cells and interactions between various cell types are frequently studied subjects. An automated and quantitative analysis of time-lapse microscopy data is an essential component of these studies, especially when characteristic migration patterns need to be identified. Plenty of software tools have been developed to serve this need. However, the majority of algorithms is designed for fluorescently labeled cells, even though it is well-known that fluorescent labels can substantially interfere with the physiological behavior of interacting cells. We here present a fully revised version of our algorithm for migration and interaction tracking (AMIT), which includes a novel segmentation approach. This approach allows segmenting label-free cells with high accuracy and also enables detecting almost all cells within the field of view. With regard to cell tracking, we designed and implemented a new method for cluster detection and splitting. This method does not rely on any geometrical characteristics of individual objects inside a cluster but relies on monitoring the events of cell–cell fusion from and cluster fission into single cells forward and backward in time. We demonstrate that focusing on these events provides accurate splitting of transient clusters. Furthermore, the substantially improved quantitative analysis of cell migration by the revised version of AMIT is more than two orders of magnitude faster than the previous implementation, which makes it feasible to process video data at higher spatial and temporal resolutions.

KEYWORDS
image processing, label-free imaging, segmentation, tracking

1 | INTRODUCTION

Image-based systems biology is a modern approach that comprises (i) automated analysis of experimental image data, (ii) quantification of biological processes in the image data, and (iii) mathematical modeling

Ivan Belyaev and Jan-Philipp Praetorius contributed equally.

This is an open access article under the terms of the Creative Commons Attribution-NonCommercial-NoDerivs License, which permits use and distribution in any medium, provided the original work is properly cited, the use is non-commercial and no modifications or adaptations are made.
© 2021 The Authors. *Cytometry Part A* published by Wiley Periodicals LLC on behalf of International Society for Advancement of Cytometry.

and computer simulation of the biological system to generate new hypotheses that can be tested in experiment [1]. To make optimal use of this iterative cycle between experiment and theory, it is absolutely necessary to work as accurately as possible in each of these three areas. In this study, we focus on improving the automated analysis of image data and, in particular, on the enhanced and fast segmentation of label-free cells for automated tracking in live-cell imaging data.

Existing cell segmentation and tracking approaches (for an overview see [2, 3]) often rely on fluorescent staining of cells. However, it is well known that staining of cells may provoke cell death during time-lapse imaging sessions and may directly affect their interaction behavior (see, for example [4]). Such observations give rise to the development of methods that are capable of analyzing label-free microscopy data. In practice, this is realized along two different directions that are based on either classical image processing (CIP) techniques or machine learning (ML) approaches. Supervised ML algorithms of deep neural networks are known to be extremely data hungry, because the success of the training process strongly depends on the quantity of training data as well as on the quality of their annotation. While training of deep neural networks can be realized in an automatized fashion, that is, based on training data with fluorescently labeled cells in combination with third party software [5], this is not an option in cases where the viability, appearance and interaction behavior of cells is altered by the fluorescent labeling. Therefore, in such situations the training data must be annotated manually, which is known to be a very subjective, error-prone, and time-consuming process. The high-quality annotation of a sufficient data volume is typically the main bottleneck of realizing deep learning approaches [6, 7]. In contrast, approaches based on unsupervised ML as well as CIP do not have such restrictions, but do require careful engineering of various parameters, for example, for thresholding or morphological filtering. This calibration procedure, which can benefit as well from some annotated image data, makes unsupervised ML and CIP the methods of choice for exploratory analyses and/or experiments with restricted data volumes. Following such an approach, we developed an algorithm for migration and interaction tracking (AMIT) that enables tracking of label-free immune cells in time-lapse microscopy data (video data).

The first version of AMIT [8, 9]—referred to as AMIT-v1—was extended by its second version—referred to as AMIT-v2—for the enhanced recognition of cell tracks as a whole by the identification and improvement of various sources for track fragmentation [10]: (i) detection of spreading cells with low contrast and (ii) optimization of the gap size parameter value, which defines the acceptable number of missing cell positions between fragments of the same track. The enhanced track recognition in AMIT-v2 yielded a significant increase in performance over AMIT-v1; for example, the average length of cell tracks was increased by more than a factor 2 [10].

However, a third source of track fragmentation has not yet been addressed: high cell densities can lead to frequent cell–cell contacts that then appear as transient clusters in image sequences. Splitting these clusters inevitably results into occasional mismatching of track fragments when trying to resolve the composition of the cellular cluster. The difficulty with this source of error is that it cannot be solved by fine-tuning the parameters, because it is inherently related to the nature of the implemented segmentation algorithm. In previous versions of AMIT, cell segmentation relied on a Gaussian mixture model (GMM) in the space of variances of pixel intensities in space and time. For example, variances in the pixel intensity are low in space and time for background pixels, whereas pixels associated with moving cells strongly vary both in their spatial and temporal intensities. This ML-supported image analysis is very well suited for the tracking of label-free cells with a high degree of morphological variability as individual objects. However, the analysis is less well-suited for accurate segmentation of cell borders and for splitting clusters of cells; one of the reasons being that this pixel-based approach may require down-sampling of high-resolution image data to limit computation times. As a consequence, low-contrast peripheral structures, such as lamellipodia, can give rise to track fragmentation due to missing nearest-neighbor associations between objects in consecutive image frames as well as incorrect estimation of the cell centroid. Additionally, under-detection of cellular processes may induce distortions in the quantitative analyses of cell morphology.

To prevent these shortcomings and to ensure a more accurate follow-up analysis, we have revised this algorithm once more. The revised version, which we refer to as AMIT-v3, includes an entirely new segmentation approach that can accurately segment label-free cells in high-resolution transmitted-light bright-field microscopy images at significantly reduced computation times.

2 | MATERIALS AND METHODS

2.1 | Segmentation and tracking in previous versions of AMIT

We advanced AMIT-v1 [8, 9] to AMIT-v2 [10] by improving the recognition of whole tracks. We briefly summarize the segmentation and tracking of cells by the following six steps:

1. Regionsofinterest (ROIs) are detected and assigned by a GMM according to the spatiotemporal variances of pixel intensities to the classes: ‘background’, ‘static objects’,or ‘moving objects’.
2. All ROIs of the class ‘moving objects’ are distinguished by a second GMM based on their area into one of the three classes: ‘noise’, ‘single cells’, or ‘cell clusters’.
3. Cellscandynamically change their morphological state, for example, appearing as spreading cells [11, 12]. In the previous step, this morphological state is observed to be associated with low contrast ‘static objects’ and altered motility characteristics. Spreading cells are therefore segmented by an additional procedure, similar to step 2, where input images are generated from a disjunction of masks for ‘static objects’ and ‘moving objects’. All ROIs that are detected in this way, but are not obtained from step 2, are considered and treated as spreading cells.
4. AllROIsof the classes ‘single cells’ and ‘spreading cells’ are tracked across consecutive time frames by the nearest-neighbor association (NNA) approach.

5. ROIsof the class 'cell clusters' are split into single cells via ellipse fitting, where the number of cells in a cluster is inferred from the area size of the cluster under consideration and the number of its overlapping single cells in the preceding and/or subsequent time frames. The tracklets of the split cells are joined to the tracklets of their corresponding single cells.
6. Celltracklets are linked into longer tracks by optimizing a distance graph. A user-defined parameter for the maximum gap size limits the acceptable number of missing cell positions between fragments of the same track.

2.2 | Revision of the segmentation algorithm in AMIT-v3

The detection of ROIs is extended by a newly designed segmentation approach that forms the core of AMIT-v3. This algorithm works with single-channel grayscale images, processes every frame of a video individually, and consists of four steps:

1. image contrast enhancement using top- and bottom-hat transformations,
2. suppression of background variation by an adaptive Wiener filter,
3. detection of regions with relatively high intensity variation by utilizing a standard deviation filter followed by a binarization with a hard threshold,
4. morphological filtering to suppress objects on the frame borders, remove small objects, and smooth object contours by erosion and opening.

The procedural independence of single frame processing allows for the parallel processing of images.

The intermediate results of the segmentation process are shown in Figure S1. The detailed descriptions of the applied operations can be found elsewhere [13]. The binarization threshold as the most critical parameter can be adjusted using a visual tool accessible in the activated debug mode. The parameters of other filters operators (except the Wiener filter, see Table S1) can be changed via configuration file. Current default parameters allow acceptable segmentation (see Section 3) for bright-field microscopy images with a resolution ~0.4 μm/pixel. To increase the precision of the segmentation for a particular experimental setup, fine-tuning of these parameters can be done with manually segmented data. An example of such optimization is shown in the Appendix S1.

AMIT-v3 can deal with situations where imaging dishes contain structural elements, for example, grid lines, which need to be removed in order to avoid segmentation artifacts. Detailed information on this removal of grid structures is provided in the Appendix S1.

2.3 | Revision of the tracking algorithm in AMIT-v3

After revision of the segmentation algorithm, we altered the conceptual dependence of tracking in previous AMIT versions on the object type, that is, on whether the object is a single non-spreading cell, a single spreading cell, or a cluster. This revision was necessary, because the GMM that classifies objects based on their area occasionally confuses spreading cells with cell clusters. In addition, it may occur that two or occasionally more cells overlap and cannot be separated from each other by the image processing methods implemented in AMIT-v2, which can lead to erroneous identifications. To address these situations and improve the detection of tracks as a whole, we implemented a new method in AMIT-v3, allowing the user to choose via a configuration file between the new cluster detection method and the old GMM-based approach.

The new cluster detection method in AMIT-v3 is based on the fusion-and-fission-tracking of ROIs and is organized as follows: All frames of a video are analyzed one after the other in subsequent pairs: (1st, 2nd), (2nd, 3rd), and so on. Within each pair of frames, the predecessors-successors relationship for each segmented ROI is analyzed and recorded. We consider a ROI as a cluster, if (i) it overlaps with at least two ROIs from the previous frame and (ii) its size of intersection with each of them exceeds a certain threshold that is defined by the user. The choice of this threshold depends on the time resolution of time-lapse imaging as well as the activity of the cells. This allows preventing false overlap detections for data with low time resolution (see Figure S2). Each joining or splitting event leads to an ID change for the current ROI. The result is a set of tracklets in which each object is assigned a type, that is, a 'single cell' or a 'cell cluster'. Based on this information, a map of detected clusters is generated for each frame. A second set of cluster maps is produced by the same sequence of operations but for the images in reversed order. In the end, the final maps of clusters are generated for each frame by combining the clusters identified in the forward and backward maps.

We illustrate this algorithm using synthetic examples. In the initial step, every object in the first frame is detected and labeled by a unique ID resulting in a label matrix L0 (Figure 1(A)). The maximal ID value for this frame is stored in a variable countIDs to count the number of unique tracks. In addition, the list of pixels of each object with the corresponding ID is collected and stored in the structure objList0.

In the next step, the same sequence of operations is applied to the second frame and the results are stored in the corresponding label matrix L1 (Figure 1(B)) and list objList1. Object labels in L0 and L1 are independent in this step. Next, for every object on L1 the intersection (Isc) with objects from L0 is analyzed and informs the decision about the current object's ID, because several different outcomes are possible (Figure 1(C), (D)). If Isc is empty (case I), the value of countIDs is incremented and the ROI receives an ID = countID. This case corresponds to the first appearance of a cell within the imaging area. A new ID is also assigned if Isc encloses at least two elements with ID>0 (case III), which is indicative for clustering of cells. If Isc consists of one element only (cases II and IV), a respective ROI on L1 inherits the ID of this element. Finally, the uniqueness of the IDs on L1 is checked. If more than one ROI has the same ID, which is indicative for cluster splitting (Figure 1(D), case IV), then every ROI receives a new ID (Figure 1(E)) and the value of countIDs is incremented. During this analysis, the information about clustering and cluster splitting events

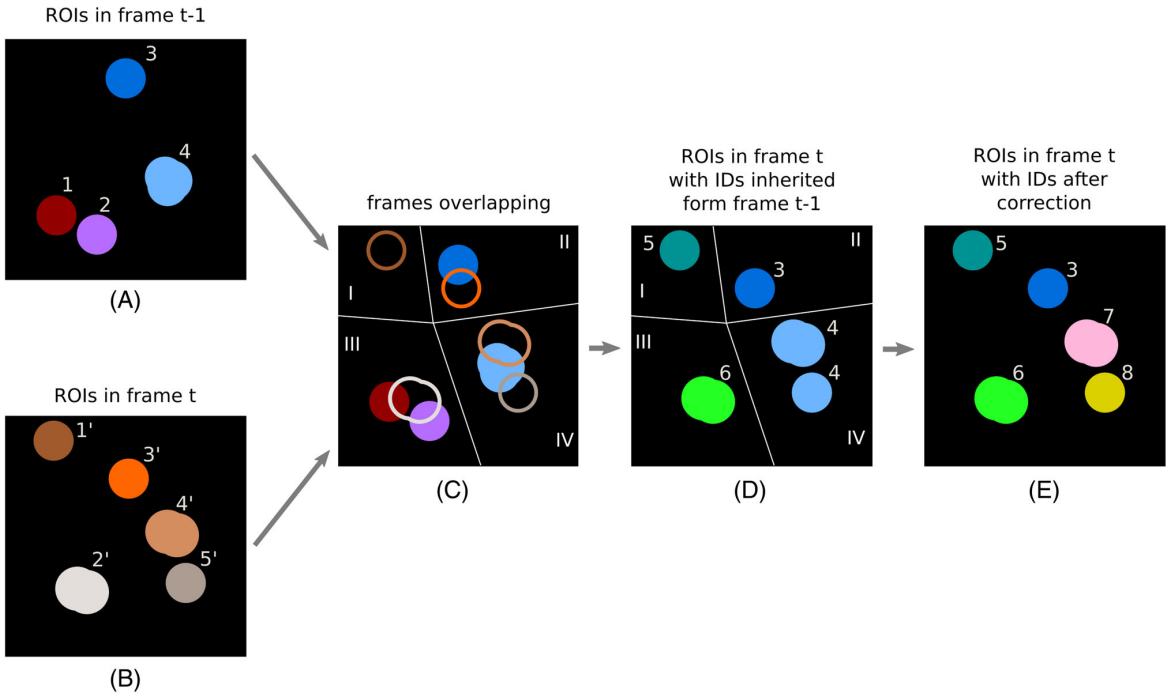

FIGURE 1 The scheme of cluster detection for two consecutive frames. (A) The first frame with all ROIs labeled (L0). (B) The second labeled frame (L1). (C) Intersection of the two frames, where only object contours are shown for the second frame. (D) The second frame with object IDs inherited from the first frame. (E) Final labels for the second frame after enforcing uniqueness of the object IDs. The ROI with ID = 6 will be identified as a cluster. Roman numbers I–IV indicate different cases for ID assignment

is stored in the list objList1. Later it will be combined with objList0 to have a temporary database of all ROIs. This step is repeated for each pair of consecutive frames. Then, all pixels of ROIs identified as clusters are placed as foreground in corresponding pre-initialized empty frames. In the same way, the maps of the detected clusters are built for the image sequence in backward order. The algorithm provides an image for each frame, in which all already segmented ROI are identified as single cell or cluster.

In the last step, the inclusive disjunction (logical OR) of each map of the forward projection is formed with the corresponding map of the backward projection to obtain the final map of clusters for each frame (Figure S3). In addition, the number of cells forming a detected cluster is recorded.

2.4 | AMIT-v3 applies hierarchical cluster splitting based on watershed segmentation

Previous versions of AMIT could not deal with splitting clusters consisting of more than just a few cells. This resulted in artifacts prohibiting the recognition of whole tracks, which prevented a correct quantitative analysis. The reason for this issue is associated with the incorrect assignment of cell IDs in two consecutive frames, which was based on a bipartition graph, that is, cells within a cluster were associated to those cells that were the closest in the previous frame. We observed that artifacts are likely to occur for clusters of more than four cells. In cases where the assignment between a single cell and its predecessor objects was incorrect, the track ends abruptly, and a new track starts in the next frame.

To prevent the occurrence of incorrect assignments of cells within a cluster, we followed an entirely new approach in AMIT-v3. We developed a hierarchical algorithm consisting of several steps (Figure 2). An important requirement for this approach is the accurate detection of clusters as well as the correct determination of the number of cells within each cluster. The number of cells within a cluster forms the basis for further splitting by watershed segmentation. Every cluster is processed independently within an area restricted by the corresponding bounding box using the cut-out of the original grayscale image. The three steps of the hierarchical cluster splitting are detailed in the subsequent sections.

2.4.1 | Step 1: Single-cell segmentation

The first step of hierarchical cluster splitting deals with the analysis of cases where boundaries between cells within a cluster are easily distinguishable. On the cut-out of the respective grayscale image, contrast enhancement will be performed to emphasize the boundaries of every cell. To restrict the noise level, Gaussian filtering is applied, followed by Canny edge detection of the cell boundaries and

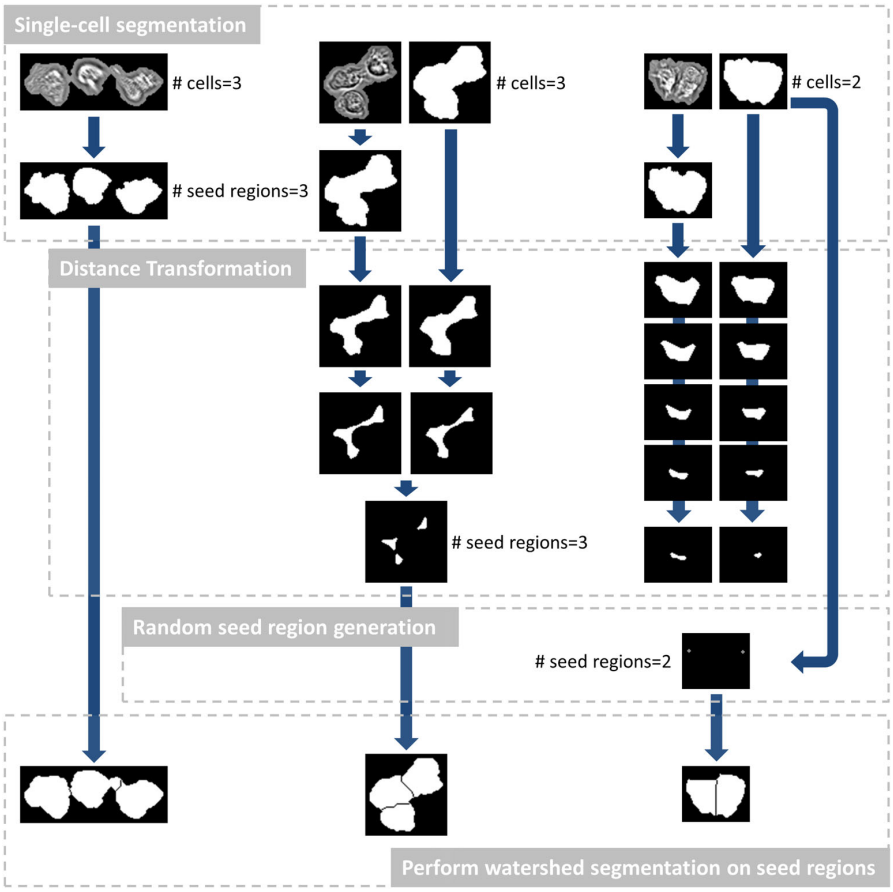

FIGURE 2 Pipeline of the hierarchical cluster splitting based on watershed segmentation. The input image is obtained from an overlay of the binary mask with the original grayscale image. The process is aborted when the number of seed regions that can be clearly distinguished corresponds to the known number of single cells within the underlying cluster. These seed regions are then used for watershed segmentation and allow for the cluster splitting [Color figure can be viewed at wileyonlinelibrary.com]

morphological closing and opening operations to fill holes and to remove small artifacts. To ensure that the detected objects overlap with the original binary cluster detection region, a binary overlap is performed between these two images. At this point, the number of underlying objects resulting from the single-cell segmentation will be compared with the number of known cells for the corresponding cluster. In case the two numbers are equal, watershed segmentation will be executed with seed regions as obtained from the single-cell segmentation (see Figure 2, left column).

2.4.2 | Step 2: Distance transformation

In cases where the membrane of the respective cells within a cluster is blurred or not detectable, single-cell segmentation alone is not enough to obtain the correct number of seed regions. Sometimes only, a tiny connection remains between two or more cells within a cluster. For these and all other remaining connections, where the number of seed regions does not match the known number of single cells within a cluster, a distance transformation is applied. This procedure requires a binary image as input and computes for each foreground pixel the distance to the next background pixel with an appropriate distance metric. In order to substantiate step 2 qualitatively, the distance transformation is performed on both the original binary image and the resulting mask from step 1. The results of the two parallel processes usually differ only very slightly and usually reach the required number of markers, so that step 2 is aborted, and a watershed segmentation is performed. In AMIT-v3, we used Euclidean distance metric and then normalized all distances relative to the maximum distance. Next, we thresholded all distances by setting the associated pixels to background pixels, if the underlying distance from the foreground to the next background pixel is shorter than a certain threshold. Here we chose a threshold of 40% of the normalized distances. For some clusters, especially for those that are circular-shaped, this step must be repeated until the number of seed regions matches the number of known cells within a cluster, or until the number of repetitions reaches a predefined maximal number. In most cases, the required number of seed regions for a cluster is achieved by the distance transformation and the splitting process can be completed (see Figure 2, central column).

2.4.3 | Step 3: Random seed region generation

However, in some cases, the required number of seed regions may not be obtained, and, in these cases, we randomly generate seed regions according to the known number of cells within the cluster

under consideration (see Figure 2, right column). For up to five known cells in a cluster, the random seed regions are extracted from the top/bottom/right/left-most point and the center point inside the cluster. If there are more cells in the cluster, the additionally required seed regions are extracted completely randomly from the cluster. This procedure is, however, just an exception handling if the conventional methods do not work and was rarely necessary for the data analyzed in this work.

Once all seed regions have been initialized, we perform cluster splitting through the watershed segmentation. The obtained seed regions are used as markers for a marker-based watershed segmentation, which is performed on the original binary mask of the current cut-out image. This results in splitting the cut-out mask into as many regions as there are cells in the cluster, as known from the cluster detection algorithm. Finally, the split cut-out image is placed at its respective position within the original full-size image.

In previous versions of AMIT, handling of single cells and clusters was done differently. For cell clusters, a graph-based splitting and tracking was performed, which occasionally lead to artifacts in situations with more than four individual cells within a cluster. In contrast, a reliable and simple NNA method was used for single cells. Our new approach is based on splitting all existing clusters into single cells. All single cells are then tracked by the NNA method, making the error-prone graph-based approach obsolete.

2.5 | Statistical analysis

For the statistical analysis of the differences between the two algorithms AMIT-v2 and AMIT-v3 as well as between the three algorithms MU-Lux-CZ, SegNet and AMIT-v3, we applied the Quade comparison test with post-hoc analysis [14]. We apply this test, because all the data that need to be compared have a non-replicated complete block design, where the algorithms define groups in the data and blocks are formed either by individual cells in the context of segmentation or by videos in the context of tracking. The null-hypothesis of this test is that, apart from individual properties of the analyzed objects (corresponding to the individual cells in the context of segmentation or videos in the context of tracking), the location parameter of an analyzed property distribution is the same for each algorithm. For comparisons of more than two groups, the obtained p values were adjusted by the Holm method [15]. All operations were done using the R package "PMCMRplus" [16].

The pairwise dissimilarity between segmentation characteristics of AMIT-v3 in comparison to the other algorithms were computed using the R implementation [17] of Hedges' g effect size statistics [18] for paired measurements [19]. The ranges of effect size magnitudes are referred to as *negligible* $|g| < 0.2$, *small* for $|g| < 0.5$, *medium* for $|g| < 0.8$ and *large* for $|g| \geq 0.8$ [20].

2.6 | Data and software availability

The data set in this study comprises seven videos of polymorphonuclear neutrophils (PMN) obtained by bright-field time-lapse microscopy, which is provided as Supplementary Data Set 1 for download at: https://asbdata.hki-jena.de/BelyaevPraetoriusEtAl2020_CytoA/Supplementary_Data_Set_1.zip

Each video comprises 1 h of recording and includes a manually tracked ground truth, which was generated in our previous study [8]. Manually segmented images for 300 cells from three different videos with various average intensities are provided as Supplementary Data Set 2 for download at: https://asbdata.hki-jena.de/BelyaevPraetoriusEtAl2020_CytoA/Supplementary_Data_Set_2.zip.

The third version of our Algorithm for Migration and Interaction Tracking (AMIT-v3) is available as open-source C++ implementation from GitHub: https://github.com/applied-systems-biology/amit.

Results of the Cell Track Challenge can be found at the corresponding website: http://celltrackingchallenge.net/participants/HKI-GE/.

3 | RESULTS

To evaluate the performance of AMIT-v3, we present the results of a quantitative comparison with AMIT-v2 regarding the accuracy of segmentation, capability to detect every ROI, and the tracking quality. The video data for migrating PMN at various cell densities (see Figure S4) are provided as Supplementary Data Set 1, and the evaluation metrics are presented in Figure 3. The choice of parameters for segmentation and tracking algorithms was determined based on two videos (1 and 4) that serve as training data sets for our evaluation. Video 4 contains the most common special cases (spreading and non-spreading cells, colliding cells and small clusters), while video 1 contains the grid lines (hemocytometer grid) mentioned in the methods chapter. Therefore, five out of the seven videos for which we presented evaluation results can be counted as a test set.

The segmentation accuracy was evaluated by comparing the results generated by AMIT-v2 and AMIT-v3 with those obtained from manually segmented images. The manually segmented images represent the ground truth (GT) data and consist of 300 cell images from three different videos with various average intensities (Supplementary Data Set 2). To make the GT data set as diverse as possible and to avoid self-correlation, every 10th–15th frame from each set was chosen corresponding to time gaps between images of about 2 min for a time step of 10 s between consecutive frames. For the quantitative characterization of the segmentation accuracy, we computed the following three complementary measures: Jaccard index, relative over-detected area (OA) and relative under-detected area (UA). The computation of these measures is depicted in Figure 3(A) indicating that high values for the Jaccard index and low values for OA and UA are desirable. As can be seen in Figure 4, the segmentation accuracy as measured by the Jaccard index for AMIT-v3 is significantly higher compared to AMIT-v2, which is driven by UA values being much lower for AMIT-v3 with a *large* effect size (see Table S3). In Figure 5, we show a typical example for the segmentation of a single cell in several subsequent frames. It is clear that AMIT-v3 provides more consistent high-quality results and allows the extraction of morphological information with only minimal distortions. Based on visual inspection

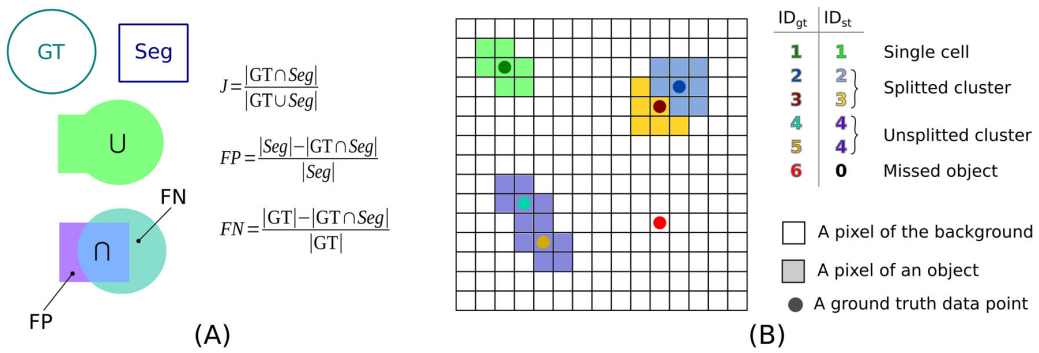

FIGURE 3 Evaluation metrics for the quantitative validation of AMIT-v3. (A) Schematic calculation of the segmentation accuracy measures: Jaccard index (J), relative over-detected area (OA) and relative under-detected area (UA). GT stands for manually annotated ROIs and Seg represents the automated segmentation. (B) Scheme of assignment of GT tracks and system tracks (ST) for a single video frame. The background pixels are assigned ID = 0

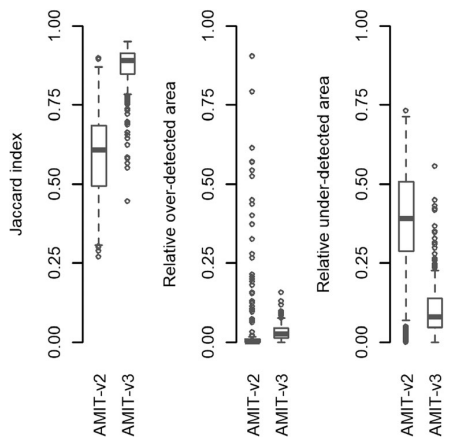

FIGURE 4 Results of the evaluation of segmentation accuracy for two test videos. The distributions represent the accumulation of GT objects. The length of whiskers corresponds to one interquartile range. All characteristics are significantly different ($p \ll 10^{-6}$) between AMIT-v2 and AMIT-v3. The effect size for the Jaccard index and UA is *large*, whereas for OA it is *negligible* (for details see Sections 2 and 2.5 and Table S3)

in comparison with the ground truth segmentation and the segmentation provided by AMIT-v3 (see Figure S11), it can be concluded that the values for OA and UA will further decrease with increasing image resolution.

In addition to the improved cell shape recognition, our new segmentation method detects more ROIs in every video, which is indicative for the increase of the total coverage ratio (Figure 6(A)), that is, the ratio between a number of GT points associated with any ROI and a total number of GT points. There were only a few non-associated points per video that typically are scattered near the frame borders. For videos 1 to 3, the majority of missing points are localized on grid lines, because the separation of cells from grid lines is not always successful. This can also be seen in the aggregated plots of detected positions in Figure S5.

Next, we evaluated the performance of cluster detection that is based on the fusion-and-fission-tracking of ROIs (see Section 2) instead of the area-based GMM classifier. It was done by first determining GT clusters as ROI on segmented images enclosing at least two GT points. Then, we compared this data with the output of the cluster detection routine and counted the number of clusters that were truly positive, falsely positive and falsely negative detected. Based on these values we calculated the precision and recall characterizing the performance of the cluster detector. As can be seen in Figure 6(B), for most videos, the majority of clusters were detected correctly. We only encountered issues with detecting and splitting the clusters that (i) exist from the first frame or until the last frame or (ii) involve complex cell interactions as the one exemplified in Figure S6.

We then compared the results produced by the tracking procedures of AMIT-v2 and AMIT-v3 relative to the GT data. While existing evaluation approaches do only allow for measuring the performance of the tracking part [10, 21], we here designed a new tracking evaluation tool, which enables validation of the trajectory reconstruction and the segmentation simultaneously. The procedure is based on the fact that for perfect tracking, every segmented ROI at every time point should enclose only one GT track point. There are three input arguments: GT tracks, tracking data with the list of associated ROI pixels, that is, the system tracks (ST) generated by the two versions of AMIT, and a 2D array of zeros (an empty frame L) with the size equal to the single frame size. All data from the first to the last time point are processed iteratively in the following way: For each time point, all entries of ST with respective time values are selected. Then, the convex hulls of the corresponding ROI in L are filled by their IDs. Afterwards, every GT point for the current time frame is associated with a ST or the background (ID = 0) as depicted in Figure 3(B). Next, all pixels in the temporary label image L are set to zero and the process is repeated for the next time point. The result is a table of ST-GT associations, which allows computing two quality measures for the tracking results [10]: (i) the track fragmentation error (TFE), which is the average number of ST associated to a single GT track, and (ii) the track

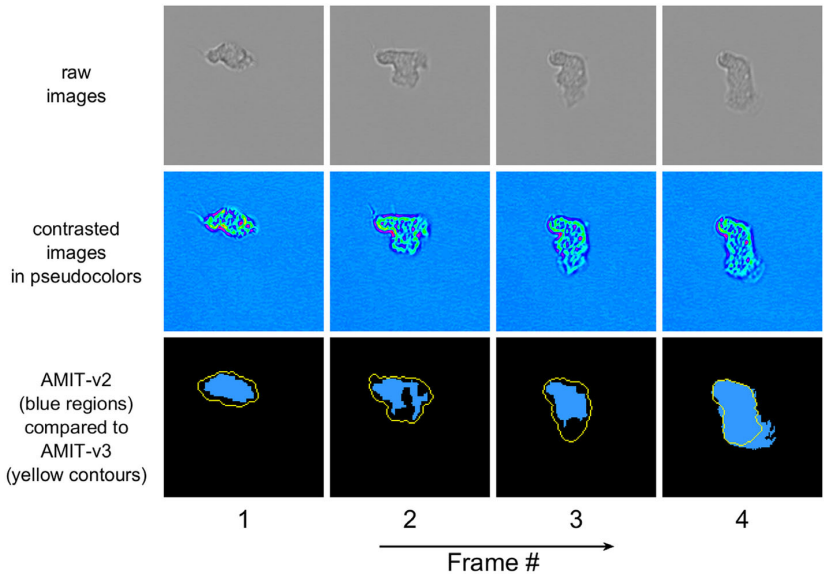

FIGURE 5 Comparison of single cell segmentation within four consecutive time frames (1–4). In the upper row, the original images are shown. The middle row represents the original images in pseudocolors after contrast enhancement. In the bottom row, segmentation results of AMIT-v2 (solid blue masks) and AMIT-v3 (yellow outlines) are shown for visual comparison exemplifying the improvement by the new segmentation algorithm

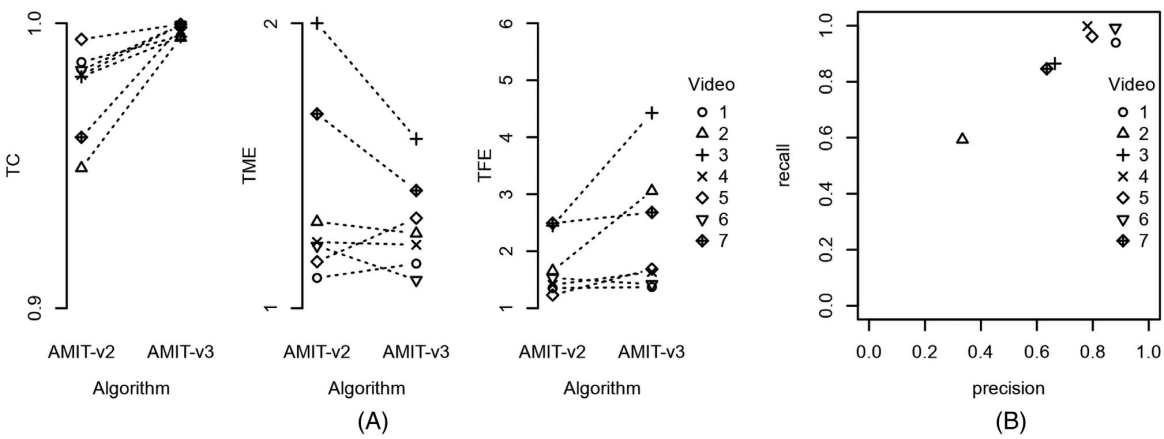

FIGURE 6 (A) Comparison of the object detection ability by the total coverage (TC) rate and tracking performance by the track merging error (TME) and the track fragmentation error (TFE). The statistical difference between AMIT-v2 and AMIT-v3 for TC has p-value $p = 0.013$ and for TFE $p = 0.065$, while this is only $p = 0.265$ for TME for the test data (videos 2, 3, 5–7). For details see Sections 2 and 2.5. (B) Cluster detection quality of AMIT-v3 in terms of recall and precision

merging error (TME), which indicates the average number of GT tracks associated with single ST. For a fair comparison of the two AMIT versions, we used convex hulls of segmented ROIs within the procedure of associating ST and GT. This allows eliminating the differences in cases where AMIT-v2 detects only peripheral structures of cells (see Figure 5, second column).

For a perfect tracking procedure, every ST track must be associated to only one GT and must have the same duration as the entire GT track; thus, perfect tracking would yield: TFE = 1 and TME = 1. As shown in Figure 6(A), the average TFE increases for AMIT-v3. There are two sources of that type of error: clusters that enter and leave the field of view as such (Figure S3) and clusters composed of overlaying cells (for an example see Video S1). For the latter case, the 3rd step in the cluster splitting procedure was applied (see Section 2), which implies random seed regions placement for the subsequent watershed segmentation. Of course, random seed regions for the cluster splitting algorithm cannot guarantee correct cluster splitting. Also, if long-lasting clusters exist for an extended time, the splitting procedure generates ROIs that might not overlap in consequent frames. As a result, the tracking procedure generates several short tracks for cells within such a cluster. At the same time, with AMIT-v3 we were able to acquire tracks with comparable or better average TME (Figure 6(A)) compared to AMIT-v2. In addition, due to improved cell detection in AMIT-v3, we were able to detect substantially more track fragments (see Figures S7 and S8). All these improvements make the tracking results of AMIT-v3 more reliable and more accurately reflecting the reality.

Going beyond the comparison between AMIT-v3 and AMIT-v2, we took part in the Cell Tracking Challenge (CTC: http://celltrackingchallenge.net/) [3, 22], where various microscopy data sets generated by different imaging modalities are provided as training and test sets. For the training set a manual annotation is provided by the CTC organizers as ground truth, which was obtained via manual annotation by independent experts with a background in biology. Once an algorithm's parameters have been adjusted utilizing the training set, the tracking results for the test set can be submitted to the CTC organizers for evaluation. The algorithm's performance is evaluated for cell segmentation and tracking by three generalized measures ranging from 0 (lowest) to 1 (highest) scores. These measures are [21]: (i) segmentation accuracy (SEG), which is based on Jaccard index and indicates how well the segmented regions of the cells match the actual cell boundaries, (ii) detection accuracy (DET), which scores detection and linking errors, and (iii) tracking accuracy (TRA), which evaluates the ability of the algorithm to track objects over time. For the evaluation of AMIT-v3 we have chosen two data sets that are referred to as Fluo-N2DH-GOWT1 and PhC-C2DH-U373, respectively, and all values given below were taken from the CTC website in March 2021.

The first data set on GFP-labeled mouse stem cells was recorded with a time step of 5 minutes over 92 frames and with a spatial resolution of 0.24 μm per pixel. According to the CTC organizers, the performance of AMIT-v3 on the test data yielded the following values for the three performance measures: SEG = 0.820, DET = 0.837 and TRA = 0.833. Even though these values are lower than those for the best three algorithms in the CTC (with performance measures between 0.91 and 0.98), this outcome can be easily explained by the following main reason: The mother-daughter association of dividing cells is not captured by AMIT-v3, as this algorithm was developed for migration scenarios of non-mitotic cells and thus without capturing mother-daughter associations.

We applied AMIT-v3 to the second data set of the CTC, which contains glioblastoma astrocytoma U373 cells that were recorded by transmitted-light phase-contrast microscopy with a time step of 15 minutes over 115 frames and with a spatial resolution of 0.65 μm per pixel. In this case, the CTC organizers evaluated the results of cell tracking on the test data by the performance measures with values: SEG = 0.615, DET = 0.981 and TRA = 0.978. The best three algorithms in the CTC have values for the segmentation accuracy SEG = 0.922–0.924 and the relatively low score for AMIT-v3 is directly related to the relatively low resolution of the images, which in some cases led to low intensity variations between the cell contour and the background. For the training set we utilized parameter values that prevent the over splitting of cells; however, these parameter values must have led to false positives associated with background pixels that were erroneously assigned pixels of cells. On the other hand, AMIT-v3 performed very well on the cell detection and tracking as can be seen from the high values of DET and TRA being close to those for the best three algorithms in the CTC with ranges DET = 0.984–0.991 and TRA = 0.979–0.982 for this data set of non-dividing cells.

Next, we performed the comparison in a reversed way by applying two established algorithms to our in-house video data: (i) Algorithm MU_Lux-CZ [23], which combines a marker-controlled watershed transformation with a convolutional neural network (CNN) and was rated one of the best algorithms in the CTC challenge. (ii) Algorithm SegNet [24], which is a widely used deep convolutional encoder-decoder architecture for image segmentation. Both algorithms are learning-based approaches and necessarily require training data. These were obtained by manually annotating 300 cells that were randomly chosen from three different videos of our in-house data. As we used these three videos also for the evaluation of the algorithms' performance, it needs to be stressed that the two neural network approaches should have a clear advantage compared to AMIT-v3, because for the latter the training set includes cells from only one video, whereas in the training of the neural networks we used the 300 annotated single cells from three different videos. We trained the two algorithms individually for each of our three in-house video data. To prevent overfitting associated with the small amount of training samples, we performed data augmentation during the training process. We then compared both algorithms with AMIT-v3 (see Figure 4 and Figure S13). The Jaccard index as the most import metric for an algorithm's segmentation performance reveals that AMIT-v3 performed significantly better ($p \ll 10^{-5}$) than MU-Lux-CZ (with *large* effect size) and SegNet (with *medium* effect size) (see Figure S13A, Table S3). The relatively high Jaccard index for AMIT-v3 is mainly due to the relatively low OA value. In addition, visual inspection of the results revealed that the applied learning-based methods either completely miss some ROIs, as is the case for MU-Lux-CZ, or split a single ROI into several ROIs, as frequently observed for SegNet. A quantitative analysis reveals that MU-Lux-CZ overlooks roughly 20% of the cells from the training set, whereas SegNet splits about 40% of the cells into more than one ROI (see Figure 13B).

4 | DISCUSSION

This computational article describes a method of cell segmentation that considerably improves our algorithm for migration and interaction tracking (AMIT) with regard to tracking of label-free immune cells in bright-field time-lapse microscopy images. A recently identified source of track fragmentation is associated with high cell densities leading to frequent cell–cell contacts that then appear as transient clusters in image sequences [10]. The splitting of these clusters inevitably results in occasional mismatching of track fragments when trying to resolve the cellular cluster composition. The difficulty with this source of error is that it cannot be solved by fine-tuning the algorithm parameters, because it is inherently related to the nature of the implemented segmentation algorithm in previous versions of AMIT. The new algorithm for cell segmentation in AMIT-v3 is associated with a noticeably increased Jaccard index (see Figure 4) and the fast and robust detection of virtually all cells within the field of view. As a consequence, substantial improvement at the level of cell segmentation enabled us to simplify the subsequent tracking procedure by skipping the

previously used optimization procedure for a distance graph and leading to a reduction of the TME in AMIT-v3 (see Figure 6(A) and Figure S9A).

Fragmentation of tracks into seemingly independent tracklets makes it impossible to follow cells over sufficiently long periods of time to study particular interaction events at the individual cell level. This prohibits the identification and quantification of cause-effect relations, for example, in the context of rare events like dumping of pathogens that were phagocytosed by PMN [25] or in order to quantitatively distinguish the immune response against various pathogens in a comparative fashion [26]. In this regard, the newly implemented cell segmentation in AMIT-v3 offers entirely new possibilities for advanced bioimage analysis of cell characteristics [27]. In the future, this feature needs to be extended for studies of interactions between immune cells and pathogens, because the qualitative and quantitative impact of labeling cell membranes was recently shown in the context of host-pathogen interactions [4]. While this analysis was done only for endpoint images of phagocytosis assays, we expect that a segmentation approach similar to the Hessian-based filtering [28], which has been shown to be successful in large-scale phagocytosis studies [29], can also be applied to host-pathogen interaction dynamics in AMIT. Another option for tracking host-pathogen interactions in a label-free manner may be pursued by the application of deep learning methods.

Once the whole tracks of migrating cells are reconstructed by AMIT, various possibilities for further quantitative analyses exist [30], such as computing a range of measures to distinguish [31–36] and model [34, 37–40] migration behavior. Moreover, the enhanced segmentation by AMIT-v3 enables a more accurate analysis of cell shape dynamics, for example, based on Fourier transformation of the cellular segmentation outline in 2D [41, 42] or spherical harmonics transformation of the cell surface in 3D [43].

Thus, AMIT-v3 yields whole tracks over long periods of time and allows extracting cell morphology at each time step. Remaining errors in the cell tracking are rare, but may be the result of long-lasting clusters of many cells. This limitation is due to multiple fusion and fission of interacting cells that are in close vicinity (for an example see Video S1), which makes it difficult—even by visual inspection for identifying ground truth tracks—to determine the correct number of cells in such clusters and to split them. To tackle these exceptional situations, we implemented a heuristic approach based on hierarchical cluster splitting method. However, it might still not be possible to correctly estimate the position of every cell within a cluster. If this turns out to be the case, we recommend excluding long-lasting clusters based on the list of clusters that is provided by AMIT-v3. Another limiting factor is associated with clusters that exist from the first frame or until the last frame (see Figure S6). These will be detected as single cells by the design of the cluster detection procedure. Generally, in order to avoid that these exceptional situations occur, it is recommended that image acquisition will always be performed with the technically highest possible temporal and spatial resolution. As high-resolution imaging will improve the segmentation accuracy, this will be indirectly beneficial for the cluster detection and splitting (see Figure S9B and
C). This recommendation is supported by the fact that the computational performance of AMIT-v3 is tremendously improved compared to previous versions of AMIT. For the same hardware configuration (Intel Core i7-4790, 16 GB RAM) we observed computation times to be reduced by a factor of ∼600 per video. Since memory resources are not increased in AMIT-v3, this opens the possibility to analyze high-resolution images on average workstations or even laptops. The main reason for this improvement over previous versions of AMIT as well as other recently published algorithms [44–46] is that ROI segmentation in AMIT-v3 does not anymore rely on a computationally expensive pixel-wise approach. Thus, high-throughput experiments may be performed with high resolution and will still be automatically analyzed within acceptable computation times. Another factor which contributes to high performance of AMIT-v3 is that it is implemented in the machine-oriented programming language C++. This will also allow for the possibility to integrate AMIT into high-performance frameworks like MISA++ [47], which combines highly efficient C++ algorithms with user-friendly plugins for ImageJ application via standardized components for parallelization and handling of data and parameters.

In summary, AMIT-v3 is capable to track cells in 2D image data that contain fluorescently labeled as well as unlabeled cells generated by various microscopy techniques, such as bright-field, differential interference contrast or phase contrast imaging. Moreover, our algorithm can be adjusted to any experimental data set with relative ease for two reasons: (i) AMITV-v3 does not require data annotation, which is mandatory for learning-based approaches [5] and (ii) AMIT-v3 requires only two main parameters that can be interactively adjusted, that is, the thresholds for segmentation and for the Canny filter during tracking. Since AMIT-v3 was developed for monitoring migration scenarios [8, 10] as well as host-pathogen confrontation assays [9] of non-mitotic cells, we did not expect it to achieve a top ranking in the CTC challenge on datasets where mother-daughter association of dividing cells occurs, although it still performed satisfactorily. Furthermore, AMIT-v3 proved to be the best method on the in-house data compared to two established ML-based approaches. These features make AMIT-v3 an excellent choice for exploratory analyses and experiments with limited amounts of image data for unlabeled cells.

ACKNOWLEDGMENTS

This work was supported by the Leibniz ScienceCampus InfectoOptics Jena, which is financed by the funding line Strategic Networking of the Leibniz-Gemeinschaft. Furthermore, we received financial support from the German Research Foundation (DFG) through the CRC/TR 124 FungiNet with project number 210879364 (Project B4 to MTF). Open access funding enabled and organized by Projekt DEAL.

CONFLICT OF INTEREST

The authors declare that no conflict of interest exists.

ORCID

Jan-Philipp Praetorius https://orcid.org/0000-0002-1828-8351
Marc Thilo Figge https://orcid.org/0000-0002-4044-9166

REFERENCES

1. Medyukhina A, Timme S, Mokhtari Z, Figge MT. Image-based systems biology of infection. Cytometry A. 2015;87:462–70.
2. MasuzzoP, Van Troys M, Ampe C, Martens L. Taking aim at moving targets in computational cell migration. Trends Cell Biol. 2016;26: 88–110.
3. UlmanV, Maška M, Magnusson KEG, Ronneberger O, Haubold C, Harder N, et al. An objective comparison of cell-tracking algorithms. Nat Methods. 2017;14:1141–52.
4. CseresnyesZ, Hassan MIA, Dahse H-M, Voigt K, Figge MT. Quantitative impact of cell membrane fluorescence labeling on phagocytosis measurements in confrontation assays. Front Microbiol. 2020;11: 1193.
5. SadanandanSK, Ranefall P, Le Guyader S, Wählby C. Automated training of deep convolutional neural networks for cell segmentation. Sci Rep. 2017;7:7860.
6. Min S, Lee B, Yoon S. Deep learning in bioinformatics. Brief Bioinform. 2017;18(5):851–869.
7. Goodfellow I, Bengio Y, Courville A. Deep Learning. Cambridge, MA: MIT Press; 2016.
8. BrandesS, Mokhtari Z, Essig F, Hünniger K, Kurzai O, Figge MT. Automated segmentation and tracking of non-rigid objects in time-lapse microscopy videos of polymorphonuclear neutrophils. Med Image Anal. 2015;20:34–51.
9. BrandesS, Dietrich S, Hünniger K, Kurzai O, Figge MT. Migration and interaction tracking for quantitative analysis of phagocyte–pathogen confrontation assays. Med Image Anal. 2017;36:172–83.
10. Al-ZabenN, Medyukhina A, Dietrich S, Marolda A, Hünniger K, Kurzai O, et al. Automated tracking of label-free cells with enhanced recognition of whole tracks. Sci Rep. 2019;9:3317.
11. BoylesJ, Bainton DF. Changing patterns of plasma membrane- associated filaments during the initial phases of polymorphonuclear leukocyte adherence. J Cell Biol. 1979;82:347–68.
12. Henry SJ, Chen CS, Crocker JC, Hammer DA. Protrusive and contractile forces of spreading human neutrophils. Biophys J. 2015;109:699–709.
13. Gonzalez RC, Woods RE. Digital image processing. 3rd ed. Italy: Pearson/Prentice Hall; 2008.
14. Quade D. Using weighted rankings in the analysis of complete blocks with additive block effects. J Am Stat Assoc. 1979;74:680–3.
15. Holm S. A simple sequentially Rejective multiple test procedure. Scand J Stat. 1979;6:65–70.
16. Pohlert T. Calculate Pairwise Multiple Comparisons of Mean Rank Sums Extended [R package PMCMRplus version 1.7.1]; 2020.
17. Torchiano M. Effsize—a package for efficient effect size computation; 2016.
18. Hedges LV, Olkin I. Statistical methods for meta-analysis. Orlando: Academic Press Inc (Verlag); 1985.
19. GibbonsRD, Hedeker DR, Davis JM. Estimation of effect size from a series of experiments involving paired comparisons. J Educ Stat. 1993;18:271–9.
20. Cohen J. A power primer. Psychol Bull. 1992;112:155–9.
21. MatulaP, Maska M, Sorokin DV, Matula P, Ortiz-De-Solorzano C, Kozubek M. Cell tracking accuracy measurement based on comparison of acyclic oriented graphs. PLoS One. 2015;10:e0144959.
22. Maška M, Ulman V, Svoboda D, Matula P, Matula P, Ederra C, et al. A benchmark for comparison of cell tracking algorithms. Bioinformatics. 2014;30:1609–17.
23. Lux F, Matula P. Cell segmentation by combining marker-controlled watershed and deep learning. arXiv. 2004;01607v1.
24. BadrinarayananV, Kendall A, Cipolla R. SegNet: a deep convolutional encoder-decoder architecture for image segmentation. IEEE Trans Pattern Anal Mach Intell. 2017;39:2481–95.
25. EssigF, Hünniger K, Dietrich S, Figge MT, Kurzai O. Human neutrophils dump *Candida glabrata* after intracellular killing. Fungal Genet Biol. 2015;84:37–40.
26. DugganS, Essig F, Hünniger K, Mokhtari Z, Bauer L, Lehnert T, et al. Neutrophil activation by *Candida glabrata* but not *Candida albicans* promotes fungal uptake by monocytes. Cell Microbiol. 2015;17:1259–76.
27. Figge MT. Quantitative bioimage analysis of cell characteristics. Cytometry A. 2018;93:278–80.
28. CseresnyesZ, Kraibooj K, Figge MT. Hessian-based quantitative image analysis of host-pathogen confrontation assays. Cytometry A. 2018;93:346–56.
29. HassanMIA, Cseresnyes Z, Al-Zaben N, Dahse HM, Vilela de Oliveira RJ, Walther G, et al. The geographical region of origin determines the phagocytic vulnerability of Lichtheimia strains. Environ Microbiol. 2019;21:4563–81.
30. SvenssonCM, Medyukhina A, Belyaev I, Al-Zaben N, Figge MT. Untangling cell tracks: quantifying cell migration by time lapse image data analysis. Cytometry A. 2018;93:357–70.
31. SbalzariniIF, Koumoutsakos P. Feature point tracking and trajectory analysis for video imaging in cell biology. J Struct Biol. 2005;151: 182–95.
32. Beltman JB, Marée AFM, De Boer RJ. Analysing immune cell migration. Nat Rev Immunol. 2009;9:789–98.
33. MokhtariZ, Mech F, Zitzmann C, Hasenberg M, Gunzer M, Figge MT. Automated characterization and parameter-free classification of cell tracks based on local migration behavior. PLoS One. 2013;8:e80808.
34. TaylorHB, Liepe J, Barthen C, Bugeon L, Huvet M, Kirk PDW, et al. P38 and JNK have opposing effects on persistence of in vivo leukocyte migration in zebrafish. Immunol Cell Biol. 2013;91:60–9.
35. MasuzzoP, Huyck L, Simiczyjew A, Ampe C, Martens L, Van Troys M. An end-to-end software solution for the analysis of high-throughput single-cell migration data. Sci Rep. 2017;7:1–13.
36. WortellMN, Dannenberg K, Berry JC, Miller MJ, Textor J. CelltrackR: an R package for fast and flexible analysis of immune cell migration data. bioRxiv. 2019;15:670505.
37. VanHaastert PJM, Postmay M. Biased random walk by stochastic fluctuations of chemoattractant-receptor interactions at the lower limit of detection. Biophys J. 2007;93:1787–96.
38. BeaucheminC, Dixit NM, Perelson AS. Characterizing T cell movement within lymph nodes in the absence of antigen. J Immunol. 2007; 178:5505–12.
39. NishimuraSI, Ueda M, Sasai M. Non-Brownian dynamics and strategy of amoeboid cell locomotion. Phys Rev E Stat Nonlinear Soft Matter Phys. 2012;85:041909.
40. Guisoni N, Mazzitello KI, Diambra L. Modeling active cell movement with the Potts model. Front Phys. 2018;6(JUN):61.
41. KriegelFL, Köhler R, Bayat-Sarmadi J, Bayerl S, Hauser AE, Niesner R, et al. Morphology-based distinction between healthy and pathological cells utilizing Fourier transforms and self-organizing maps. J Visual Exp. 2018;140:e58543.
42. Kriegel FL, Köhler R, Bayat-Sarmadi J, Bayerl S, Hauser AE, Niesner R, et al. Cell shape characterization and classification with discrete Fourier transforms and self-organizing maps. Cytometry A. 2018;93:323–33.
43. MedyukhinaA, Blickensdorf M, Cseresnyés Z, Ruef N, Stein JV, Figge MT. Dynamic spherical harmonics approach for shape classification of migrating cells. Sci Rep. 2020;10:1–12.
44. VanValen DA, Kudo T, Lane KM, Macklin DN, Quach NT, DeFelice MM, et al. Deep learning automates the quantitative analysis of individual cells in live-cell imaging experiments Meier-Schellersheim M, editor. PLoS Comput Biol. 2016;12:e1005177.
45. HilsenbeckO, Schwarzfischer M, Loeffler D, Dimopoulos S, Hastreiter S, Marr C, et al. fastER: a user-friendly tool for ultrafast and robust cell segmentation in large-scale microscopy murphy R, editor. Bioinformatics. 2017;33:2020–8.
46. TsaiHF, Gajda J, Sloan TFW, Rares A, Shen AQ. Usiigaci: instance-aware cell tracking in stain-free phase contrast microscopy enabled by machine learning. SoftwareX. 2019;9:230–7.

ISAC CYTOMETRY Journal of Quantitative Cell Science PART A

47. Gerst R, Medyukhina A, Figge MT. MISA++: a standardized interface for automated bioimage analysis. SoftwareX. 2020;11:100405.

SUPPORTING INFORMATION

Additional supporting information may be found online in the Supporting Information section at the end of this article.

How to cite this article: Belyaev I, Praetorius J-P, Medyukhina A, Figge MT. Enhanced segmentation of label-free cells for automated migration and interaction tracking. Cytometry. 2021;99:1218–1229. https://doi.org/10.1002/cyto.a.24466

3.2 Automated characterisation of neutrophil activation phenotypes in *ex vivo* human *Candida* blood infections

FORMULAR 1

Manuskript Nr. (laufende Nummer in der Dissertation) **2**

Titel des Manuskriptes: Automated characterisation of neutrophil activation phenotypes in *ex vivo* human *Candida* blood infections.

Autoren: Belyaev I., Marolda A., Praetorius J.-P., Sarkar A., Medyukhina A., Hünniger K., Kurzai O., Figge M.T.

Bibliographische Informationen (falls publiziert oder zur Publikation angenommen: Zitat):

Comput Struct Biotechnol J, 2022; 20: 2297–308.

Der Kandidat / Die Kandidatin ist (bitte ankreuzen)

☐ Erstautor/-in, ☒ Ko-Erstautor/-in, ☐ Korresp. Autor/-in, ☐ Koautor/-in.

Status (falls nicht publiziert; „zur Publikation eingereicht“, „in Vorbereitung“):

Anteile (in %) der Autoren / der Autorinnen an der Publikation (anzugeben ab 20%)

Autor/-in	**Konzeptionell**	**Datenanalyse**	**Experimentell**	**Verfassen des Manuskriptes**	**Bereitstellung von Material**
Belyaev I.	25	50	20	40	0
Marolda A.	35	20	60	20	0
Praetorius J.-P.	5	15	10	5	0
Sarkar A.	5	15	10	5	0
Medyukhina A.	5	0	0	0	0
Hünniger K.	5	0	0	10	0
Kurzai O.	10	0	0	10	50
Figge M.T.	10	0	0	10	50
Total:	100	100	100	100	100

Computational and Structural Biotechnology Journal 20 (2022) 2297–2308

ELSEVIER

COMPUTATIONAL AND STRUCTURAL BIOTECHNOLOGY JOURNAL

journal homepage: www.elsevier.com/locate/csbj

Automated characterisation of neutrophil activation phenotypes in *ex vivo* human *Candida* blood infections

Ivan Belyaev [a,b,1], Alessandra Marolda [c,1], Jan-Philipp Praetorius [a,b], Arjun Sarkar [a,b], Anna Medyukhina [a,d], Kerstin Hünniger [c,e], Oliver Kurzai [c,e,f,*,2], Marc Thilo Figge [a,g,*,2]

[a] Applied Systems Biology, Leibniz Institute for Natural Product Research and Infection Biology – Hans-Knöll-Institute, Jena, Germany
[b] Faculty of Biological Sciences, Friedrich-Schiller-University Jena, Germany
[c] Fungal Septomics, Leibniz Institute for Natural Product Research and Infection Biology –Hans-Knöll-Institute, Jena, Germany
[d] Center for Bioimage Informatics, St. Jude Children's Research Hospital, Memphis, TN
[e] Institute for Hygiene and Microbiology, University of Würzburg, Würzburg, Germany
[f] Center for Sepsis Control and Care (CSCC), Jena University Hospital, Jena, Germany
[g] Institute of Microbiology, Faculty of Biological Sciences, Friedrich-Schiller-University Jena, Germany

ARTICLE INFO

Article history:
Received 21 January 2022
Received in revised form 4 May 2022
Accepted 5 May 2022
Available online 10 May 2022

Keywords:
Candida infection
Bloodstream infection
Whole blood infection model
Image analysis
Machine learning
Diagnostic markers

ABSTRACT

Rapid identification of pathogens is required for early diagnosis and treatment of life-threatening bloodstream infections in humans. This requirement is driving the current developments of molecular diagnostic tools identifying pathogens from human whole blood after successful isolation and cultivation. An alternative approach is to determine pathogen-specific signatures from human host immune cells that have been exposed to pathogens. We hypothesise that activated immune cells, such as neutrophils, may exhibit a characteristic behaviour — for instance in terms of their speed, dynamic cell morphology — that allows (i) identifying the type of pathogen indirectly and (ii) providing information on therapeutic efficacy. In this feasibility study, we propose a method for the quantitative assessment of static and morphodynamic features of neutrophils based on label-free time-lapse imaging data. We investigate neutrophil activation phenotypes after confrontation with fungal pathogens and isolation from a human whole-blood assay. In particular, we applied a machine learning supported approach to time-lapse microscopy data from different infection scenarios and were able to distinguish between *Candida albicans* and *C. glabrata* infection scenarios with test accuracies well above 75%, and to identify pathogen-free samples with accuracy reaching 100%. These results significantly exceed the test accuracies achieved using state-of-the-art deep neural networks to classify neutrophils by their morphodynamics.

© 2022 The Authors. Published by Elsevier B.V. on behalf of Research Network of Computational and Structural Biotechnology. This is an open access article under the CC BY-NC-ND license (http://creativecommons.org/licenses/by-nc-nd/4.0/).

1. Introduction

Candida bloodstream infections (BSI) are the most common form of invasive candidiasis and constitute the fourth leading cause of nosocomial invasive infections in Intensive Care Units (ICUs) patients in the US [1]. The study on Extended Prevalence of Infection in Intensive Care (EPIC II) revealed that the prevalence of *Candida* BSI was 6.9 per 1000 patients with an associated mortality rate of around 43% compared to 27% caused by bacterial BSI [2]. Among hospitalised patients, *Candida* species present the most frequent isolated fungal BSI pathogens [3]. In particular, *C. albicans* and *C. glabrata* are responsible for the majority of *Candida* cases worldwide, where *C. albicans* is the predominant species with 50% of cases, while *C. glabrata* is responsible for 15–25% of invasive *Candida* infections in the US and Northern Europe [4]. These statistical data imply that methods for the fast and reliable diagnosis are urgently needed to allow for an early start of targeted treatments.

Various animal models have been used to study invasive *Candida* infections, such as fruit fly, zebrafish and mouse. In contrast, human whole-blood infection (WBI) models enable analysing host-pathogen interactions in a setting similar to *in vivo* BSI [5]. The human WBI models allowed (i) identifying virulence factors [6], (ii) analysing immune responses including time-resolved data

* Corresponding authors at: Fungal Septomics, Leibniz Institute for Natural Product Research and Infection Biology –Hans-Knöll-Institute, Jena, Germany (O. Kurzai). Applied Systems Biology, Leibniz Institute for Natural Product Research and Infection Biology – Hans-Knöll-Institute, Jena, Germany (M.T. Figge).

E-mail addresses: oliver.kurzai@leibniz-hki.de (O. Kurzai), thilo.figge@leibniz-hki.de (M.T. Figge).

[1] Authors contributed equally.
[2] Authors contributed equally.

https://doi.org/10.1016/j.csbj.2022.05.007
2001-0370/© 2022 The Authors. Published by Elsevier B.V. on behalf of Research Network of Computational and Structural Biotechnology.
This is an open access article under the CC BY-NC-ND license (http://creativecommons.org/licenses/by-nc-nd/4.0/).

on immune cell activation and pathogen status [7], and (iii) testing potential therapeutic approaches [8,9]. We have previously studied BSI by combining the human WBI model with the quantification of immune processes by virtual infection modelling [5,10]. In this context, we found that neutrophils play a central role in the defence against *C. albicans* BSI. Moreover, we have performed extensive comparative analyses for the two species *C. albicans* and *C. glabrata* and found that they are differentially recognised by neutrophils using live cell imaging combined with automated image analysis [11–14] and computational modelling [15–18]. This motivated us to study the possibility of automatically identifying the type of pathogen in BSI based on neutrophil morphological properties.

In this feasibility study, we combine the human WBI model with live cell imaging of primary neutrophils and computational analysis to extract features that allow us to detect BSI caused by *C. albicans* and *C. glabrata*. The central hypothesis is that (i) neutrophils in a human WBI model respond with morphological changes to the presence of pathogens and (ii) these changes are pathogen-specific. To advance the development of rapid and reliable diagnostic methods, we are investigating the potential of the automated characterisation of neutrophil activation phenotypes for human *Candida* BSI. From a technical point of view, this study exploits our recent developments regarding the analysis of live cell imaging data with respect to tracking of unlabelled cells over extended times [19] and segmenting cells with high accuracy for dynamical changes of their morphology (morphodynamics) [20]. Features of immune cells under different stimuli that have been previously studied include (i) changes in cell size [21], (ii) modifications of membrane topography [22,23] and (iii) variations in the migration behaviour [24]. Our study utilizes features based on the cell morphodynamics and provides a fully automated pipeline based on live cell imaging data of unlabelled primary neutrophils in order to distinguish the two scenarios of *Candida* BSI.

2. Materials and Methods

2.1. Ethics statement

This study was conducted in accordance with the Declaration of Helsinki. All protocols were approved by the Ethics Committee, University Hospital Jena (permit number: 273–12/09).

2.2. Fungal strains and culture

GFP-expressing *C. albicans* [5] and *C. glabrata* [25] strains were routinely used in all experiments. *C. albicans* and *C. glabrata* were seeded in yeast extract–peptone–dextrose medium (YPD medium: 2% D-glucose, 1% peptone, and 0.5% yeast extract, in water) and grown overnight at 30 °C and 37 °C, respectively, in a shaking incubator. Both fungal species were reseeded in fresh YPD medium, grown until they reach the mid-log phase followed by harvesting in HBSS.

2.3. Whole-blood infection model

To avoid anticoagulation and not influence complement activation, human peripheral blood from healthy donors was drawn in Hirudin S-monovettes® (Sarstedt) after informed consent. Whole-blood infection assay was performed as described previously, using an inoculum that allows rapid innate immune activation but precludes unspecific effects on adaptive immune cells [5]. In brief, HBSS (mock-infected control), *C. albicans* or *C. glabrata* were added in a final concentration of 1×10^6 fungal cells per 1 ml of whole blood and then incubated for 1 h at 37 °C on a rolling mixer. After incubation, samples were used directly for neutrophil isolation with sequential live cells imaging of neutrophils.

2.4. Isolation of human neutrophils

Untouched neutrophils were isolated from either mock- or *Candida*-infected blood using MACSxpress Whole Blood Neutrophil Isolation Kit according to the instructions from the manufacturer (Miltenyi Biotec). Remaining erythrocytes were lysed for 5 min with ACK Lysing Buffer (Life Technologies) and purity of neutrophils was checked at flow cytometry to be >95% (see Supplementary Fig. 1). For this, neutrophils were stained with mouse anti-human CD66b antibody (BD Biosciences Cat# 561649, RRID: AB_10897169) for 20 min at 4 °C and measured with the BD FACSCanto™ II system and the BD FACSDiva™ software (both BD Biosciences). In parallel, staining with the appropriate isotype control antibody (BD Biosciences Cat# 560861, RRID: AB_10926214) was performed to ensure specificity of antibody binding. FlowJo10 software was used for analysis. Obtained neutrophils were resuspended in RPMI 1640 with 5% heat-inactivated human serum and used for live cell imaging.

2.5. Live cell imaging and Time-lapse microscopy

Live cell imaging was performed by adding 4×10^5 neutrophils isolated either from mock-, *C. albicans*- or *C. glabrata*-infected human blood in a μ-dish (ibidi) in a total volume of 2 ml RPMI 1640 containing 5% heat-inactivated human serum. 2.5 ng/ml of propidium iodide (PI, Sigma) was added into the medium to distinguish viable cells from dead ones. PI stains only nucleic acids in dying cells characterized by leak in the plasma membrane. Therefore, death of a neutrophil or a fungal cell can be identified in the video by the respective cell/fungus turning red fluorescent. Neutrophils were incubated in an environmental control chamber at 37 °C and 5% CO_2. Images were acquired every 7 s with a Zeiss LSM 780 confocal microscope, which was focused on the bottom of the dish. Cells behaviour was monitored with a 20x microscope objective (Zeiss Plan-APOCHROMAT 20x/0.8NA) using a differential interference contrast (DIC) setting with illumination by 488 nm laser. Image size was 2048 by 2048 px with the scale 0.208 μm/px.

2.6. Segmentation and tracking of neutrophils

For cell detection and tracking we used our Algorithm for Migration and Interaction Tracking (AMIT, [13,14,19]) in its latest release of the third version [20] that is available from our GitHub repository: https://github.com/applied-systems-biology/amit. AMIT enables automated segmentation and tracking of label-free cells from microscopy data. In addition, it provides the possibility to eliminate track segments associated with long-lasting clusters of cells that may be indistinguishable by eye. This post-processing procedure is necessary, because the extraction of unbiased information about the morphology of individual cells inside such clusters is impossible. The maximal possible track duration is about 30 min corresponding to the 260 frames of recorded video with a frame rate of about one frame per seven seconds.

2.7. Measurement of neutrophil speed

The instantaneous cell speed was calculated from consecutive time steps in μm/min for each cell track. These instantaneous speed values were used to compute the arithmetic mean speed value per cell. The latter was collected from all cell tracks of a video as a representative speed value distribution. In addition, for every video, the set of instantaneous cell speeds was split into two sub-

sets by a cell morphology detector. As explained in detail below, this detector distinguishes between cells with non-spreading morphology (N-morphology) and spreading morphology (S-morphology) and enables to numerically distinguish the measured neutrophil speed for these two morphology states.

2.8. Extraction of gradient-based cell features

For each frame in a video from time-lapse microscopy, we applied a morphological contrast enhancement [26] and contrast-limited adaptive histogram equalisation [27] as a pre-processing step, followed by gradient detection with the Sobel operator [28] to compute an intensity gradient magnitude map per image. Afterwards, all values were normalised to the maximal value of the gradient amplitude for a given video (see Supplementary Fig. 2) and for each previously segmented neutrophil, the value range of [10th, 80th] percentiles in the pixel intensity was used as a descriptor of cell surface roughness. This feature is also referred to as pHG-descriptor, since it is based on the percentiles of the histogram for the normalised gradient magnitudes.

2.9. Data set organisation and sampling procedures

After cell tracking and feature extraction, each video was represented by a track file consisting of a table that contains the description of each cell at every time point. The various analyses of the video data were then made based on this table.

For the evaluation of the robustness of the N-morphology detector, we performed Monte-Carlo simulations by randomly selecting 1.8×10^3 cells per iteration from every video of the mock-infected samples. These were used in the calibration set, while the video data of samples infected by *Candida* composed the test set. The number of 1.8×10^3 cells was chosen, because it corresponds approximately to the number of cells in the episodes of the first 5 min of the video with lowest cell concentration. Including data from each donor was necessary for the compensation of variations between videos regarding illumination issues that were not fully compensated during extraction of gradient-based cell features.

In the population-based analysis of snapshots, information about each video was split into two parts corresponding, respectively, to the first 42 frames ($\sim$ 5-minutes-episodes) and the following 218 frames ($\sim$ 25-minutes-episodes) of a video. Then, for the N-morphology detector calibration, we randomly selected the 1.8×10^3 cells from the 5-minutes-episodes of each video of mock-infected samples. The 25-minutes-episodes composed the test set and was used for the estimation of spreading cell fraction in each sample (see subsection 3.3) and instantaneous speed analysis (see subsection 3.4).

The morphodynamics analysis was performed on the complete videos (30 min) of *Candida*-infected samples. In these analyses of tracked cells, we compared characteristic distributions (see subsections 3.4 and 3.5). In order to reduce the influence of individual samples we used a fixed number of instances (complete cell tracks or track fragments) that were randomly selected from each video in the following way: (i) the characteristics of interest were sorted in ascending order, where multiway sorting was applied in the case of more than one descriptor; (ii) the desired number of instances was derived by generating random indexes from a uniform distribution covering the whole range of the initial vector indices. This strategy yields statistically representative sampling.

2.10. Detection of cells with N-morphology

For the detection of cells based on specific descriptors, a single-class classifier was created using the method of Data Driven Soft Independent Modelling of Class Analogy (DD SIMCA) [29,30], which is a modification [31] of the classical SIMCA [32] approach. SIMCA is a well-known tool for pattern recognition in many research and industrial applications (for example, see [33–38]). The DD SIMCA method utilises a decomposition of data by principal component analysis (PCA) [39] for a description of the target class data structure within a multicollinear feature space combined with the statistics of two distances that are used to characterise variability inside the calibration set (see Supplementary Fig. 3). The first distance refers to the position of an object (the point in a multivariate feature space which represents a real object) relative to the model (orthogonal distance, OD) and the second distance refers the displacement between the projection of the object onto the model and the centre of this model (score distance, SD). The statistics of these distances are used to establish two rules: (i) a decision rule for the detection of extreme/unusual objects, *i.e.* objects that do not follow major trends in the calibration data grasped by the principal components, and (ii) an acceptance rule for the classification of new objects. Both rules impose a comparison of the respective statistics of the distances with regard to critical values. While the classical SIMCA relies on F-statistics of OD and utilises parameters of the calibration data set (number of samples and variables) together with the number of chosen components in the PCA model for the computation of critical values, the DD SIMCA employs scaled chi-squared distributions of OD and SD for the calibration set in the estimation of critical values. Respecting the data structure makes the latter method more suitable for statistical unmixing of multivariate distributions of data.

In the present study, we applied this method in the following unsupervised way: (i) PCA was performed for the whole calibration data set comprising cells from mock-infected samples with N-morphology being the dominant form. The analysis of PCA results revealed that the first and second principle components are enough to describe more than 90% of total variation in data on mock-infected samples (see Supplementary Fig. 3). We therefore limited the number of principle components in the model to two. (ii) An outlier border was determined using the outlier significance level $\gamma = 0.01$, which specifies the probability that at least one point from the data will be erroneously considered as an outlier [30]. (iii) All data points beyond the outlier border were considered to be outliers and were removed from the calibration data set, *i.e.* we performed multidimensional distribution unmixing and obtained a representative purified population of cells with N-morphology. This filtered calibration set was then used for the final model calibration and acceptance area determination. (iv) In the classification procedure, all data points within the acceptance area were assigned to be cells with N-morphology, while all other cells were considered to have S-morphology.

All operations were done using the R package 'mdatools' [40].

2.11. Automated classification of infection scenarios

To automatically classify the various infection scenarios, we applied a two-step procedure: (i) each instance, *i.e.* a video frame in the population-based analysis of snapshots or a cell track in the morphodynamics analysis, was classified by a Bayesian classifier [41] after pre-calibration by a calibration set. (ii) A video was assigned to a certain infection scenario based on a majority voting by the individually classified instances.

We used the R package 'naivebayes' [42] to perform the Bayesian classification (in case of multiple descriptors a naïve form).

2.12. Comparison of cell characteristics for different infection scenarios

We used the multiple quantile comparison method [43]. This method utilises a combination of the Harrell-Davis quantile estimator [44] and a bootstrapping to determine the confidence interval (CI) for the difference between quantiles of the distributions to be compared. The difference in certain quantiles of any two distributions is considered to be significant in frequentist sense at confidence level α.

All computations were done with the R package 'WRS2′ [45].

2.13. Multiple group comparison test

In cases where the data have a non-replicated complete block design we used the Quade test with post-hoc analysis [46]. This method is a generalisation of the signed paired rank test for three or more groups, where the null-hypothesis says that, apart from donor effects, the location parameter of the analysed property is the same for each infection scenario. The obtained p-values were adjusted by the Holm method [47].

All operations were done using the R package "PMCMRplus" [48].

2.14. Effect size statistics

To numerically characterise a magnitude of difference between conditions and be able to compare it between different characteristics (median fraction of spreading cells per frame and average speed) we used the common language effect size (CLES), which expresses the probability that a randomly selected score from one group will be greater than a randomly sampled score from another one [49]. The values were computed with the R package 'canprot' [50] using empirical probability density functions.

In addition, we computed the difference between distributions via Hedges g effect size statistics [51] for paired measurements [52] and computed the standard deviations for each group individually. For this we used the R package 'effsize' [53].

2.15. Confidence intervals for proportions

We applied the method of Wilson's confidence interval computation for single proportions [54,55] using the R package 'PropCIs' [56]. The input arguments included: (i) confidence level α (probability of type I error, set to $\alpha = 0.05$), (ii) total number Θ of entities to be examined and (iii) number of 'successes' θ. For the interval estimation of the fraction of cells with morphodynamics that is considered to be specific for a true infection scenario in a given sample, θ corresponds to the number of such cells among all Θ examined cells. See the following sub-section for more details.

2.16. Post-hoc analysis of errors of type II

In addition to Wilson's confidence intervals we computed the probability for making an error of type II regarding the evaluation of two alternative hypotheses about pathogen-specific morphodynamics. The null-hypothesis corresponds to the statement that a pathogen-specific morphodynamics does not exist; therefore, fractions of cells with *C. albicans*- and *C. glabrata*-specific morphodynamics are expected to be equal 0.5 in each sample. The alternative corresponds to the hypothesis that a pathogen-specific morphodynamics does exist; therefore, observed fractions of cells with specific morphodynamics for a given infection scenario must be greater than 0.5. For samples where the detected fraction of cells specific for a given pathogen is less than 0.5, the probability of error type II for a given set of hypotheses cannot be computed.

The probability was computed using a one-sample single side test for proportions [57] as implemented in the R package 'MKPower' [58].

3. Results

Our results are based on time-lapse imaging data of live unlabelled neutrophils, recorded over a period of 30 min with a frame rate of about one frame per seven seconds (260 frames in total) (for details see subsection 2.5). These cells were isolated from human whole-blood infection (WBI) assays (see subsection 2.3) with either of two *Candida* species — *C. albicans* or *C. glabrata* — and were compared to neutrophils from mock-infected blood. In total we have acquired blood samples from 9 healthy donors that were each subdivided to separately study and compare the three infection scenarios.

3.1. Neutrophils exhibit morphological signatures induced by pathogen-interaction in human whole blood

Visual inspection of the video data revealed the existence of two types of dynamically appearing cell morphologies. In Fig. 1, we provide a typical example for a neutrophil that dynamically changes its morphology into the state of a spreading cell (S-morphology) and back into the morphology of a non-spreading cell (N-morphology) via a sequence of intermediate states. Thus, in a first approximation, the cell population $C(t_i)$ in video frame i can be considered as a mixed distribution of cells composed of two morphologies: $C(t_i) = S(t_i) + N(t_i)$, where $S(t_i)$ and $N(t_i)$ denote the number of cells with S- and N-morphology, respectively, at time point t_i. The fraction of cells exhibiting S-morphology is defined by.

$$\sigma(t_i) \equiv S(t_i)/C(t_i) \tag{1}$$

with $0 \leq \sigma(t_i) < 1$. In agreement with previous findings that peculiar morphological patterns are a sign of neutrophil activation [23], we observed that cells with S-morphology were only rarely present ($\sigma(t_i) \ll 1$) among neutrophils isolated from mock-infected blood (see Supplementary video set 1). In contrast, the occurrence of cells with S-morphology was observed more frequently and for a larger cell fraction after confrontation with either *C. albicans* or *C. glabrata*. This observation motivated us to design a workflow for the automated identification of neutrophil morphology and the quantitative comparison of infection scenarios by the occurrence of cells with S-morphology.

3.2. Automated classification yields highly robust predictions of neutrophil morphology

We performed the segmentation and tracking of neutrophils with our software tool AMIT [13,14], which was recently enhanced to recognise whole cell tracks [19]) and to additionally extract morphological information on dynamically changing cell shapes [20]. In particular, the distinction between S- and N-morphology of neutrophils required the identification of descriptors that are sensitive to the size and surface texture of cells and robust against varying and uneven illumination in the images as well as against inaccuracies in the cell segmentation. Considering these requirements as well as the non-rigidness of neutrophil shapes, two adequate descriptors were identified: (i) the cell's footprint area and (ii) the intensity-gradient of segmented neutrophils (for details see subsection 2.8).

Using these descriptors, we built a one-class classifier for neutrophils with N-morphology acting as a novelty detector, *i.e.* all cells rejected by the classifier were considered to be cells with S-

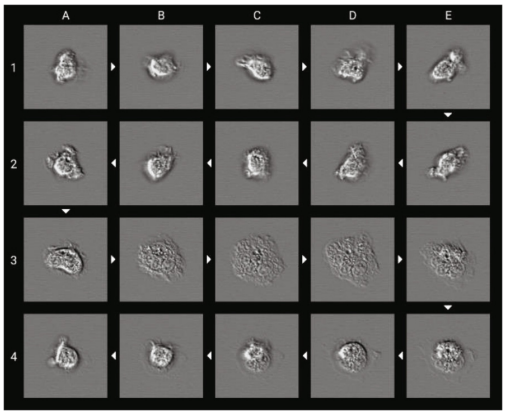

Fig. 1. Time-dependent change of a single neutrophil during 20 consecutive frames (arrows indicate the time ordering). Cells in sub-images B3–E3 can be considered as spreading cells (S-morphology).

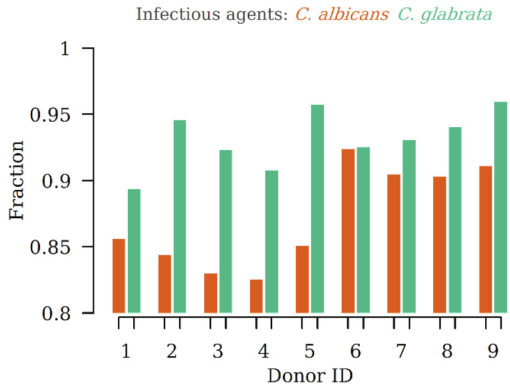

Fig. 2. Fraction of cells repeatedly identified as exhibiting S-morphology in each repetition of the Monte-Carlo simulations. Each sample includes O(10^4) segmented cell images.

morphology. This approach elegantly circumvents the necessity of manual distinction between S- and N-morphology for every cell, which is labour-intensive and could easily result in a bias of the classifier. Thus, we here use our observational knowledge that neutrophils with N-morphology are the predominant type within mock-infected samples. The one-class classifier corresponds to a statistical procedure for the unmixing of the morphology distribution and allows the estimation of $\sigma(t_i)$ for every frame in a video (for details see subsection 2.10).

The robustness of our classifier regarding estimation of $\sigma(t_i)$ was checked by performing Monte-Carlo simulations with 10^3 repetitions, where the N-morphology detector was calibrated using an equal number of randomly selected cells from each mock-infected sample (for details see subsection 2.9). This detector was used for cell classification in videos with neutrophils isolated from *C. albicans* and *C. glabrata* WBI. For every cell the received labels, *i.e.* S- or N-morphology, were recorded before counting how often each cell was assigned to be a cell with S-morphology. We then analysed the statistics of cells being associated with that class in at least one of iteration during the simulations (Fig. 2). For every infected sample, more than 80% of such cells received that label 10^3 times (Fig. 2, see also Supplementary Fig. 4). This supports the robustness of the classifier outcome with regard to providing a trustworthy estimate of $\sigma(t_i)$. Supplementary video set 2 visualises the classification results from a single iteration for various videos.

3.3. Donor variability obscures predictions based on classification by neutrophil morphology

Based on our one-class classifier, we addressed our hypothesis that the three scenarios — mock-infection, *C. albicans* infection and *C. glabrata* infection — may be distinguishable by the frequency of neutrophils occurring in the S- or N-morphology. For this analysis every video was divided into two episodes with durations of 5 and 25 min, which were used for the calibration of the N-morphology detector and for the characterisation of samples via the distributions of values $\{\sigma(t_i)\}$ (for details see subsection 2.9). Taking into account fluctuations of $\sigma(t_i)$ caused by cell migration in and out of the field of view, we focused on the median as the indicator of central tendency of the $\{\sigma(t_i)\}$-distribution for the 25-minutes-episodes. The classification results are summarised per donor in Fig. 3a and reveal quantitative differences between the three infection scenarios (see Fig. 3b and Table 1). The statistical differences per infection scenario support our hypothesis regarding the pathogen-specific morphological changes of neutrophils in a human WBI assay.

Next, we implemented a Bayesian classifier with majority voting to identify infection scenarios based on $\{\sigma(t_i)\}$-distributions (for details see subsection 2.11). We performed simulations with leave-one-out cross-validation (LOOCV) [41], where we performed 9^3 iterations for the three infection scenarios with nine samples each by fixing one sample from every infection scenario as test sample and using all other samples for classifier calibration. This approach allows imitating large sample populations and measuring the classifier performance in the case of low sample numbers.

The classifier was evaluated by the observed successful classification ratio (OSCR), which equals the fraction of correctly assigned samples for a given class. As can be seen in Fig. 3c, our classification procedure recognises mock-infected samples with OSCR = 1, which confirms that the classifier can successfully distinguish infected and non-infected samples. However, as can be inferred from Fig. 3a, distinguishing between different infection scenarios is obscured by the donor variability. In fact, for *C. albicans* infection we obtained the reduced value of OSCR = 0.89, while for *C. glabrata* infection the performance dropped to OSCR = 0.67. As shown in Fig. 3b, the medians of the $\{\sigma(t_i)\}$-distributions were not suited for achieving a clear distinction between the two infection scenarios. The LOOCV reveals that this is also true for the mock-infected samples (see Fig. 3d), as can be seen from the reduction of the certainty measure by about 11% (compare Fig. 3c and d). Nevertheless, these overall promising findings prompted us to advance our analysis from a population-based analysis of snapshots to the analysis of individual cell tracks including aspects of morphodynamics.

3.4. Neutrophil speed is inadequate for discrimination of Candida infection scenarios

Visual inspection of the video data gives the impression that, depending on the infection scenario with either of the two *Candida* species, the morphodynamics of neutrophils may be different (see Supplementary video set 1). In particular, neutrophils seem to (i) experience differently long episodes in the state of S-morphology and (ii) migrate slower when in the state of S-morphology compared to N-morphology. We hypothesised that a specific morphodynamics behaviour of neutrophils may be induced upon contact with a particular pathogen in human whole blood and speculated that the discrimination of infection scenarios may be improved by accounting for dynamic effects.

I. Belyaev, A. Marolda, Jan-Philipp Praetorius et al. Computational and Structural Biotechnology Journal 20 (2022) 2297–2308

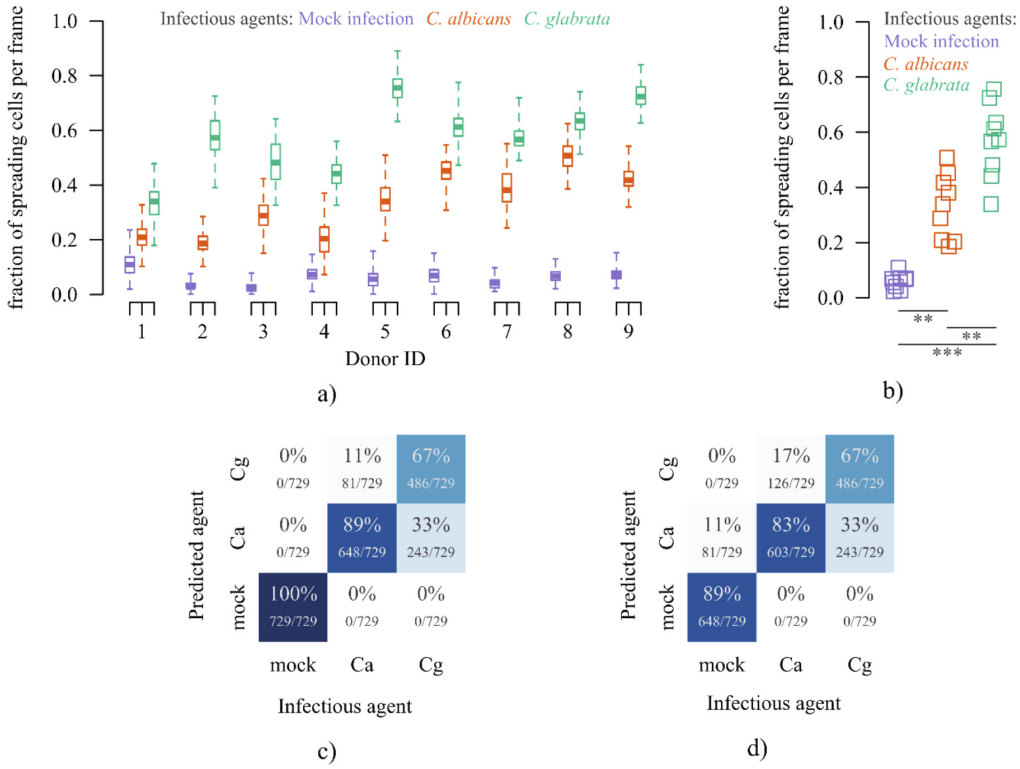

Fig. 3. a) Box diagrams for the fraction of spreading cells per video frame (260 frames in total) for each donor. b) Median value of the distributions in a) per donor. ** $p = 0.0027$, *** $p \ll 10^{-4}$ (Quade test with post-hoc analysis and p adjustment by Holm). The effect size statistics is listed in the Table 1. c) Confusion matrix for the results of the Bayesian classifications based on individual frames. Each cell of the matrix represents the ratio of proper sample classifications (numerator) for given infection scenarios over all iterations (denominator). d) Confusion matrix for the results of a sample classification based on description of whole video data.

Table 1
Comparison of effect sizes expressed via common language effect size (CLES) and Hedge's $|g|$ for median fraction of spreading cells ($CLES_{frac}$, $|g_{frac}|$) and for average speed per sample ($CLES_{speed}$, $|g_{speed}|$). Details about calculations are described in paragraph *Effect size statistics* in Materials and Methods section.

Pair for comparison	$CLES_{frac}$	$CLES_{speed}$	$\lvert g_{frac}\rvert$	$\lvert g_{speed}\rvert$
'mock'–'*C. albicans*'	1	0.91	3.18	1.58
'mock'–'*C. glabrata*'	1	0.94	5.47	2.13
'*C. albicans*'–'*C. glabrata*'	0.90	0.63	1.67	0.35

To quantify these observations, we first computed the average speed for each neutrophil from its individual cell track for each donor and infection scenario. However, as shown in Fig. 4a, there is no evidence for a clear pathogen-specific impact on the average neutrophil speed. On first sight, this finding may seem contradictory to a previous study where the average neutrophil speed was reported to be a suitable discrimination feature [24]. However, while that study was performed in the context of the myelodysplastic syndrome, the sample average neutrophil speed (Fig. 4b) is evidently not an adequate discrimination feature in the present context of *Candida* BSI, because this measure appears to be less pathogen-sensitive than the dynamic change in cell morphology (Fig. 3b). This was also confirmed by a quantitative comparison of effect size measures (see Table 1 and subsection 2.14) and considering our results on the morphology-based classification of infection scenarios (Fig. 3d).

Thus, while a speed-based classification of infection scenarios will not yield acceptable accuracies, we still wanted to validate our impression from the visual inspection that there are differences in the morphodynamics of neutrophils for the two *Candida* species. To this end, neutrophils were first classified as being either in the S- or N-morphology followed by the computation of the instantaneous speed distributions for each infection scenario with the two *Candida* species. As can be seen in Fig. 5a and b, the majority of neutrophils with S-morphology are indeed statistically slower, which has also been confirmed by a comparison of the distributions using the multiple quantile comparison method [59] to compute the difference Δ between consecutive percentiles of the respective distributions for the two *Candida* infection scenarios (Fig. 5c). Another evidence for a speed difference between spreading cells and non-spreading ones is a near-monotonical decline (Spearman's $\rho = -0.74$) of the average speed per cell with increasing fraction of spreading cells (Fig. 5d). Thus, while the visual impression could be confirmed, we still have to conclude that neutrophil speed is not an adequate feature for discrimination of WBI with different *Candida* species.

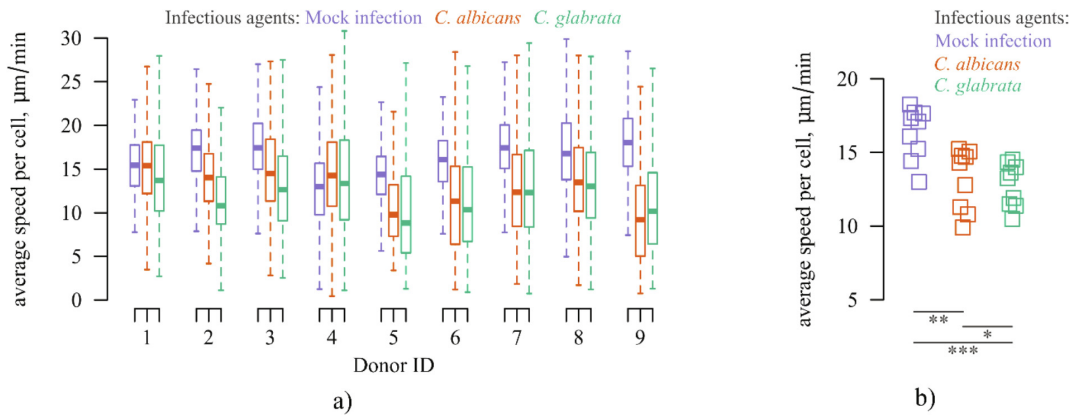

Fig. 4. Diagrams of the average speed per cell (a) and per donor (b). The number of data points per sample is O(10^4), length of whiskers is not larger than 1.5 interquartile interval. For data in (b) the Quade statistical test was applied with post-hoc analysis and p adjustment by Holm: * p = 0.1265, ** p = 0.0224, *** p = 0.0011. The effect size statistics is listed in the Table 1.

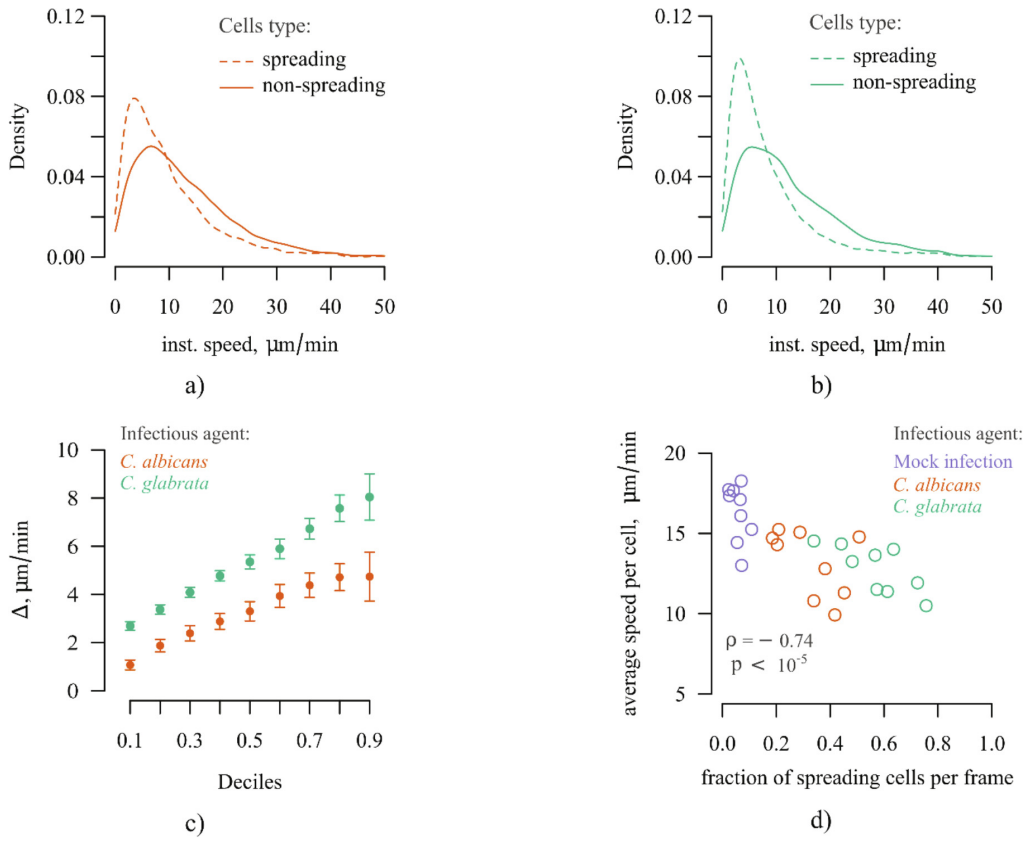

Fig. 5. Distributions of instantaneous speed for spreading and non-spreading neutrophils for a joint sample sets after confrontation with (a) *C. albicans* and (b) *C. glabrata*. Each joint sample set (represented by an individual curve) includes 9×10^3 data points composed of data from randomly selected 1×10^3 spreading cells (dashed lines) or an equal amount of non-spreading cells (solid lines) from each video. c) Shift functions presented by the difference between deciles of distributions in (a) and (b), respectively. The whiskers indicating the 0.95 bootstrap CI (for details see subsection *Comparison of cell characteristics for different infection scenarios* in the Materials and Methods section). d) Scatter diagram demonstrating the correlation between the median fraction of spreading cells per frame and median average speed per cell for the same sample.

3.5. Evidence for the existence of pathogen-specific morphodynamics of neutrophils

Next, we computed neutrophil morphodynamic features based on the information from the previous classification of neutrophil morphology states. Using this information every tracked cell can be characterised by a frequency of transitions to the spreading state, the total amount of time a cell exists in that state, and the duration of its longest spreading episode. Here, in order to reduce too short cell tracks and by that the noise in the data, we restricted the analysis to cells that were observed for at least 90 s (13 frames) and that switched at least once to the spreading morphology with a maximal duration of at least 28 s (4 frames). These restrictions excluded only 20% of neutrophils in samples infected by the *Candida* species (see Supplementary Fig. 5). As shown in Fig. 6, the visual impression that neutrophils tend to exhibit the S-morphology for longer episodes after confrontation with *C. glabrata* compared to the infection with *C. albicans* could be quantitatively confirmed. As can be seen in Fig. 6, the total duration of spreading episodes per track (Fig. 6b) and the maximal duration of spreading episodes per track (Fig. 6c) showed statistical differences between infection scenarios. These were considered relevant for distinguishing between infection scenarios, although these characteristics may be susceptible to donor-specific variability (see Supplementary Fig. 6). To perform the classification task based on neutrophil morphodynamics, we used a combination of naïve Bayes classifier for individual track classification followed by a majority voting for the whole sample classification (for details see subsection 2.11). Thus, a test sample was assigned to one of the infection scenarios based on majority fraction of tracked cells being identified as *C. albicans*-specific or *C. glabrata*-specific. For classifier evaluation, we used the LOOCV per condition sampling procedure (with 9^2 iterations in total).

Using this morphodynamics-based classification we reached OSCR = 1 for the *C. albicans*-infected samples, which is higher than in the population-based analysis of snapshots. However, for the *C. glabrata*-infected samples the OSCR remains roughly the same: OSCR = 0.63. Since the maximal duration of spreading episodes per track is a characteristic that is robust against track fragmentation, which may be caused by track interruptions due to long-lasting clusters, we also used this feature alone in the Bayesian classifier. The OSCR raised to OSCR = 0.78 for *C. glabrata*, while the quantitative results for *C. albicans* remained the same (Fig. 7a). Finally, in Fig. 7b the typical detected fraction (mean value over all iterations) of cells with morphodynamics specific for the true infection scenario is shown for every donor and infection scenario. In addition, for every infection sample we performed an interval estimation (defined via Wilson's confidence

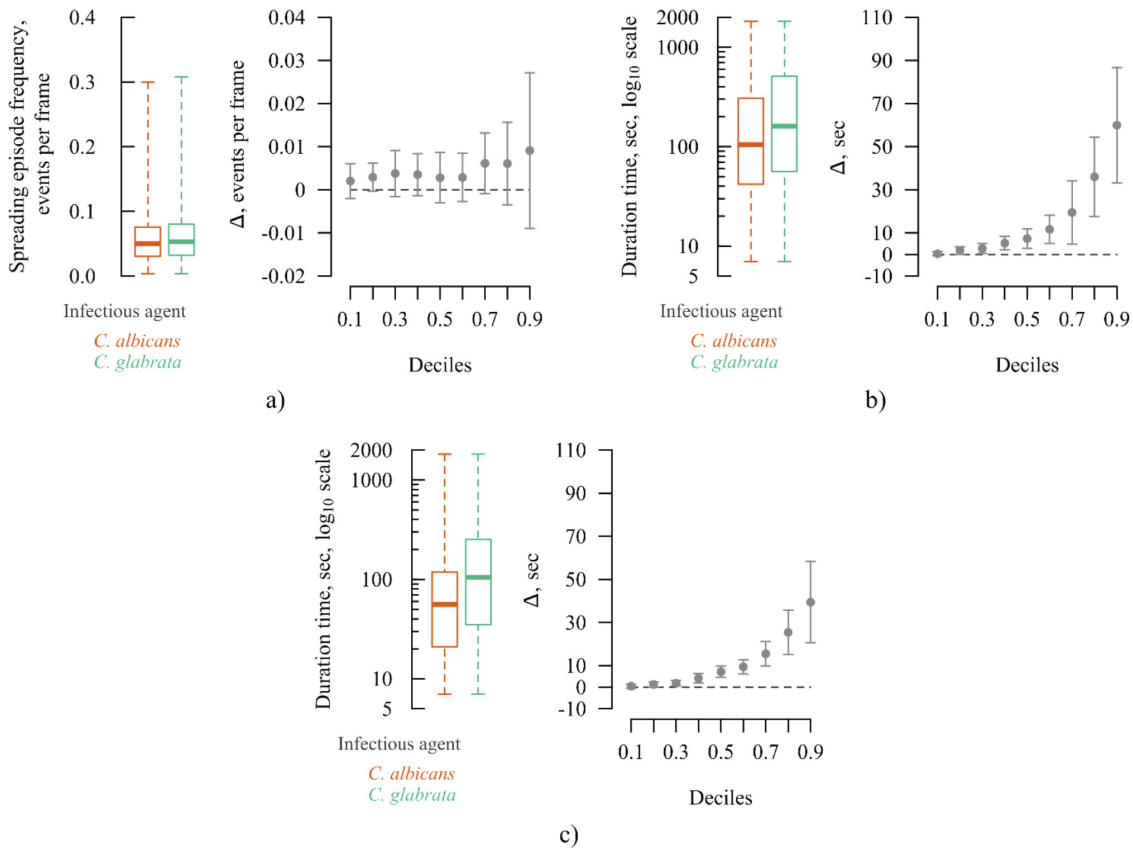

Fig. 6. Comparison of morphodynamics descriptors for joint populations of *C. albicans*- or *C. glabrata*-infected neutrophils by a box plot with whiskers indicating the whole range of values as well as decile-difference diagrams with whiskers indicating 0.95 bootstrap CI (see subsection *Comparison of cell characteristics for different infection scenarios* in the Materials and Methods section). All diagrams were built using balanced sampling (for details see subsection *Data set organisation and sampling procedures* in the Materials and Methods section). a) Distributions of the normalised number of transitions between non-spreading and spreading state. b) Distributions of the total amount of time that cells remain in state with S-morphology. c) Distributions of durations of the longest spreading episode per cell track.

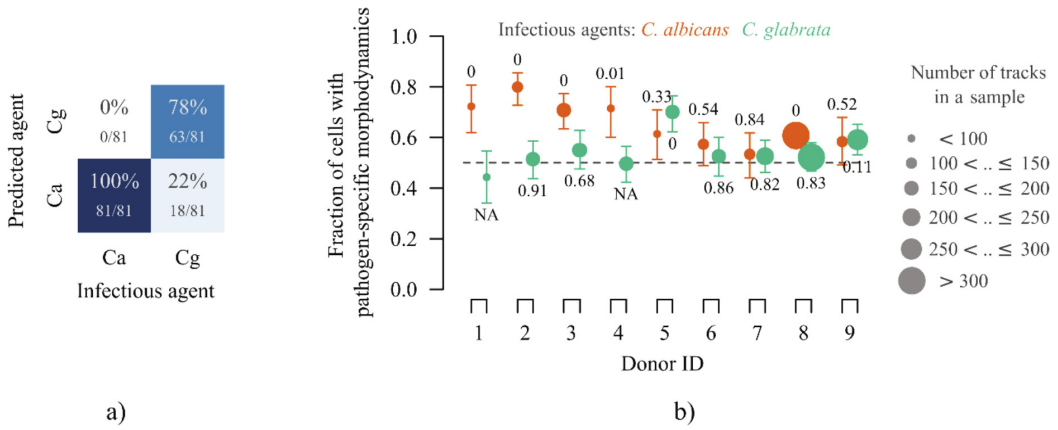

Fig. 7. a) Confusion matrix for sample classification results based on the fraction of neutrophil tracks with pathogen-specific morphodynamics. b) The typically detected fraction of cells with pathogen-specific morphodynamics in a given sample. The mean value is computed over all iterations and the whiskers indicate 0.95 CI for the detected fraction (see *Confidence intervals for proportions* in the Materials and Methods section). The number indicates a probability of the error type II for fraction of neutrophils with *C. albicans*- or *C. glabrata*-specific morphodynamics in a given sample. The symbol NA was used where the computation of this probability is not possible. For further details see subsection *Post-hoc analysis of errors of type II* in the Materials and Methods section.

interval, for details see subsection 2.15) of the fraction of cells with morphodynamics that can be considered specific for the true infection scenario. For instance, for the *C. glabrata*-infected sample from the donor with ID 2, which was represented by about 200 cells in the video, ∼52% of all cells were characterised by the morphodynamics analysis to be specific for the *C. glabrata* rather than the *C. albicans* infection scenario. However, the corresponding confidence interval extends to values below 50% indicating that there is a probability that the fraction of cells in the whole blood sample with *C. glabrata*-specific morphodynamics equals that of *C. albicans*. We in fact estimated this probability to equal 91% in the case of blood donor with ID 2 (for details see subsection 2.16). In contrast, for blood donors with ID 5 and ID 9, this probability is estimated to be 0% and 11%, respectively. Moreover, for six out of the nine blood donors, the probability of having an equal number of cells showing *C. glabrata* and *C. ablicans* morphodynamics for a true infection scenario with *C. albicans* is well below 35%.

Taken together, while we cannot rule out misclassifications of infection scenarios with *C. albicans* and *C. glabrata*, taking into account the morphodynamics of neutrophils does improve the classification accuracy (Fig. 7b) compared to the static analysis (Fig. 3c) from 67% to 78% for *C. glabrata* and from 89% to 100% for *C. albicans*.

3.6. White-box approach passes deep neural network challenge

Finally, we challenged our white-box approach for identifying the pathogen-specific morphodynamics of neutrophils based on the two descriptors 'neutrophil footprint area' and 'intracellular intensity-gradient'. To this end, we applied state-of-the-art deep neural network technique by evaluating the classification results of a long short-term memory (LSTM) network [60] for data from the nine donors with a leave-one-out cross-validation (LOOCV) [41] (see *Blood sample classification using Deep Learning techniques* in the Supplementary materials). Overall, we achieved test accuracies (ACC) well below 65% from 7000 image sequences obtained from each class (two infection scenarios and the mock-infected samples). In particular, this LSTM-based-approach yielded only moderate values of ACC = 0.7 for mock-infected samples, ACC = 0.63 for *C. albicans*-infected and ACC = 0.48 for *C. glabrata*-infected samples. The corresponding confusion matrix (Supplementary Fig. 8e) reveals the difficulties of the LSTM to discriminate the neutrophil morphodynamics between infection scenarios with *C. glabrata* and *C. albicans*.

4. Discussion

The application of imaging technologies is an essential component of disease diagnosis and treatment monitoring of patients with life-threatening bloodstream infections. It encompasses a wide range of tools and methods utilised to examine an organism at different levels ranging from the detection of infection foci in a whole organ by computed tomography to identifying pathogens by means of microscopy with high spatial and temporal resolution. In particular, modern label-free methods have a promising potential in the future, among which various types of spectral imaging including Raman spectroscopy, Fourier transform infrared (FTIR) spectroscopy, or matrix-assisted laser desorption/ionization time-of-flight mass spectrometry (MALDI-ToF MS) providing information about the molecular composition of individual cells. Even though the efficiency of these spectroscopy techniques has been demonstrated for fungal cultures (e.g., [61–63]), limitations for their application in the rapid identification of pathogens in human blood remain. In particular, methods based on cell cultivation require more than 24–48 h, which can lead to fatal delays in initiating pathogen-specific therapy. Moreover, for pathogen concentrations in the sample well below the observed median concentration in clinical samples, which is only 1 CFU/mL for *Candida* bloodstream infections [64], cell cultivation for pathogens may not even be successful. Therefore, since immune cells like neutrophils must have sensed the infection-causing pathogens in patient blood, these interactions are hypothesised to induce measurable changes in the readily available neutrophils that may allow for the indirect identification of pathogens. For example, as was recently shown applying Raman spectroscopy, neutrophils that were first isolated from human whole-blood and subsequently confronted *in vitro* with Gram-positive bacteria (*Staphylococcus aureus*), Gram-negative bacteria (*Escherichia coli*), and fungal pathogens (*C. albicans*) could be distinguished by their molecular

fingerprint [65]. The present study advances along these lines while optimizing various aspects: (i) we investigated activation phenotypes of isolated neutrophils after confrontation with pathogens in the human whole-blood assay to more realistically mimic pathogen detection for bloodstream infections, (ii) we focused on fungal pathogens and the distinction of two species from the *Candida* genus that require different treatment strategies, and (iii) we decided for the commonly available imaging technique of time-lapse microscopy to investigate the pathogen-specific morphodynamics of neutrophils as activation phenotype.

We developed an effective method for the automated comparative analysis of morphological and behavioural changes in neutrophils using live-cell imaging data. As a model system we used the human WBI assays with two most common fungal bloodstream pathogens — *C. albicans* and *C. glabrata*. We started with visual inspection of the acquired videos revealing that in *Candida*-infected samples neutrophils with spreading (S-) morphology appear more often, whereas in mock-infected samples neutrophils with non-spreading (N-) morphology is the dominant morphotype. Based on this observation, we constructed an N-morphology detector (one-class classifier), which was calibrated fully automatically and, therefore, free from operator errors. We could also demonstrate that the classifier outcome is weakly depending on the cells used in the calibration (Fig. 2 and Supplementary Fig. 4). Using this classifier, we were able to estimate the fraction of neutrophils with S-morphology over the whole observation period (Fig. 3). In addition, we showed that the fraction of neutrophils with S-morphology is statistically higher for infection scenarios with *C. glabrata* (Fig. 3b), suggesting the possibility for rapid differentiation between blood samples infected by the two *Candida* species (Fig. 3c and d).

Based on the classifier outcome and the tracking data, we performed an extended analysis of the behaviour of neutrophils from *Candida*-infected samples. We showed that in our experimental conditions the average neutrophil speed per sample is not a reliable marker of infection (Fig. 4), although there is a difference in neutrophil speed when comparing N- and S-morphology (Fig. 5). In contrast, regarding the morphodynamics of neutrophils, we quantitatively confirmed the observation that long-lasting spreading episodes are more often appearing for infection scenarios with *C. glabrata* than *C. albicans* (Fig. 6), which leads to the improvement of infection recognition in our WBI assays (Fig. 7a). However, we cannot assert an observation of pathogen-specific morphodynamics of neutrophils unequivocally due to sample and donor variabilities (Fig. 7b) as well as the number of blood samples. For example, as indicated by a power analysis (significance level $\alpha = 0.05$, expected power of 0.8), approximately 1000 blood donors would be required for a statistically definitive conclusion that at least 54% of neutrophils, which corresponds to the average fraction detected in our experiments, exhibit *C. glabrata*-specific morphodynamics in a *C. glabrata*-infected sample. While recruiting this large number of blood donors is clearly beyond the scope of our feasibility study, we inferred the following analysis pipeline for the best classification results: (i) calibration of the one-class classifier based on static features of neutrophils from non-infected samples, (ii) classification of samples being infected or not based on the fraction of spreading cells, (iii) including neutrophil morphodynamics to distinguish between samples from different infection scenarios.

In this study, we applied our Algorithm for Migration and Interaction Tracking (AMIT, [13,14,19]) in its latest release of the third version [20]. The performance of AMIT with regard to the automated segmentation and tracking of label-free neutrophils was previously found to outcompete established learning-based algorithms [20], such as MU_Lux-CZ [66] and SegNet [67]. Nevertheless, in the present study we checked whether deep neural networks can improve the distinction of infection scenarios by *C. albicans* and *C. glabrata* based on a long short-term memory (LSTM) network [60], which we applied to classify the time-series of neutrophils with dynamically changing morphology. However, this black-box-approach yielded relatively moderate test accuracies (ACC) with values well below 65% compared to our white-box approach that is based on the two descriptors 'neutrophil footprint area' and 'intracellular intensity-gradient' and achieved values well above 75% for the two infection scenarios and 100% for mock-infected samples. We speculate that this may be explained by peculiarities of the LSTM network architecture, which may be unable to grasp sufficient information about aperiodic spreading events from relatively short sequences.

In further studies, instead of increasing the complexity of analysis pipelines, we consider improving the cell description by adding information about intensity and amount of neutrophilderived trail formation [68,69] and neutrophil autofluorescence [70,71]. This could be tested after modification of the image acquisition step implying detection of transmitted light images by a high-resolution camera with a high readout speed (or global shutter) at intervals of one second or shorter. This would allow eliminating cell-movementassociated blurring effects and by that improve the accuracy in image processing with regard to cell segmentation and tracking as well as morphological information. Besides, it would pave the way for detailed analysis of dynamic transitions between the two states of N- and S-morphology, as well as performing comparative analyses of potentially different S-morphologies under various conditions. In addition, high-speed imaging would enable estimating within-donor heterogeneity, which is particularly essential regarding the neutrophil population microheterogeneity, *i.e.* existence of neutrophil sub-sets with different functions, distinct morphology as well as receptor repertoires [72–74]. Extension of this feasibility study to a larger cohort of blood donors and inclusion of BSI patients will be the next step for exploring the potential of this approach for translational research.

Declaration of Competing Interest

The authors declare that they have no known competing financial interests or personal relationships that could have appeared to influence the work reported in this paper.

Acknowledgements

This work was supported by the Leibniz ScienceCampus InfectoOptics Jena, which is financed by the funding line Strategic Networking of the Leibniz Association. Furthermore, we received financial support from the German Research Foundation (DFG) through the CRC/TR 124 FungiNet with project number 210879364 (Project B4 to MTF, Project C3 to OK). This work was supported by the Federal Ministry of Education and Research, Germany (grant number 13GW0456B) in the context of InfectoGnostics Research Campus Jena.

Appendix A. Supplementary data

Supplementary data to this article can be found online at https://doi.org/10.1016/j.csbj.2022.05.007.

References

[1] WisplinghoffH,Bischoff T, Tallent SM, Seifert H, Wenzel RP, Edmond MB. Nosocomial bloodstream infections in US hospitals: Analysis of 24,179 cases from a prospective nationwide surveillance study. Clin Infect Dis 2004;39:309–17.

[2] KettDH, Azoulay E, Echeverria PM, Vincent J-L. Candida bloodstream infections in intensive care units: Analysis of the extended prevalence of infection in intensive care unit study. Crit Care Med 2011;39:665–70.
[3] HornDL, Fishman JA, Steinbach WJ, Anaissie EJ, Marr KA, Olyaei AJ, et al. Presentation of the PATH Alliance® registry for prospective data collection and analysis of the epidemiology, therapy, and outcomes of invasive fungal infections. Diagn Microbiol Infect Dis 2007;59:407–14.
[4] Perlroth J, Choi B, Spellberg B. Nosocomial fungal infections: Epidemiology, diagnosis, and treatment. Med Mycol 2007;45:321–46.
[5] HünnigerK, Lehnert T, Bieber K, Martin R, Figge MT, Kurzai O. A Virtual Infection Model Quantifies Innate Effector Mechanisms and Candida albicans Immune Escape in Human Blood. PLoS Comput Biol 2014;10:e1003479.
[6] Echenique-RiveraH, Muzzi A, Del Tordello E, Seib KL, Francois P, Rappuoli R, et al. Transcriptome Analysis of Neisseria meningitidis in Human Whole Blood and Mutagenesis Studies Identify Virulence Factors Involved in Blood Survival. PLoS Pathog 2011;7:e1002027.
[7] TenaGN, Young DB, Eley B, Henderson H, Nicol MP, Levin M, et al. Failure to Control Growth of Mycobacteria in Blood from Children Infected with Human Immunodeficiency Virus and Its Relationship to T Cell Function. J Infect Dis 2003;187:1544–51.
[8] PlestedJS, Welsch JA, Granoff DM. Ex vivo model of meningococcal bacteremia using human blood for measuring vaccine-induced serum passive protective activity. Clin Vaccine Immunol 2009;16:785–91.
[9] SprongT, Brandtzaeg P, Fung M, Pharo AM, Høiby EA, Michaelsen TE, et al. Inhibition of C5a-induced inflammation with preserved C5b-9-mediated bactericidal activity in a human whole blood model of meningococcal sepsis. Blood 2003;102:3702–10.
[10] LehnertT, Timme S, Pollmächer J, Hünniger K, Kurzai O, Figge MT. Bottom-up modeling approach for the quantitative estimation of parameters in pathogen-host interactions. Front Microbiol 2015;6:608.
[11] DugganS, Essig F, Hünniger K, Mokhtari Z, Bauer L, Lehnert T, et al. Neutrophil activation by Candida glabrata but not Candida albicans promotes fungal uptake by monocytes. Cell Microbiol 2015;17:1259–76.
[12] Essig F, Hünniger K, Dietrich S, Figge MT, Kurzai O. Human neutrophils dump Candida glabrata after intracellular killing. Fungal Genet Biol 2015;84:37–40.
[13] BrandesS, Mokhtari Z, Essig F, Hünniger K, Kurzai O, Figge MT. Automated segmentation and tracking of non-rigid objects in time-lapse microscopy videos of polymorphonuclear neutrophils. Med Image Anal 2015;20:34–51.
[14] BrandesS, Dietrich S, Hünniger K, Kurzai O, Figge MT. Migration and interaction tracking for quantitative analysis of phagocyte–pathogen confrontation assays. Med Image Anal 2017;36:172–83.
[15] LehnertT, Prauße MTE, Hünniger K, Praetorius JP, Kurzai O, Figge MT. Comparative assessment of immune evasion mechanisms in human whole-blood infection assays by a systems biology approach. PLoS ONE 2021;16: e0249372.
[16] PraußeMTE, Lehnert T, Timme S, Hünniger K, Leonhardt I, Kurzai O, et al. Predictive Virtual Infection Modeling of Fungal Immune Evasion in Human Whole Blood. Front Immunol 2018;9:560.
[17] TimmeS, Lehnert T, Prauße MTE, Hünniger K, Leonhardt I, Kurzai O, et al. Quantitative simulations predict treatment strategies against fungal infections in virtual neutropenic patients. Front Immunol 2018;9:667.
[18] LehnertT, Leonhardt I, Timme S, Thomas-Rüddel D, Bloos F, Sponholz C, et al. Ex vivo immune profiling in patient blood enables quantification of innate immune effector functions. Sci Reports. 2021. 111. 2021. 11. 1–16.
[19] Al-ZabenN, Medyukhina A, Dietrich S, Marolda A, Hünniger K, Kurzai O, et al. Automated tracking of label-free cells with enhanced recognition of whole tracks. Sci Rep 2019;9:3317.
[20] Belyaev I, Praetorius JP, Medyukhina A, Figge MT. Enhanced segmentation of label-free cells for automated migration and interaction tracking. Cytom Part A. 2021. cyto.a.24466.
[21] HoffsteinST, Friedman RS, Weissmann G. Degranulation, membrane addition, and shape change during chemotactic factor-induced aggregation of human neutrophils. J Cell Biol 1982;95:234–41.
[22] Wang L, Castro CE, Boyce MC. Growth strain-induced wrinkled membrane morphology of white blood cells. Soft Matter 2011;7:11319–24.
[23] JumaaMAA, Dewitt S, Hallett MB. Topographical interrogation of the living cell surface reveals its role in rapid cell shape changes during phagocytosis and spreading. Sci Rep 2017;7:1–11.
[24] SchusterM, Moeller M, Bornemann L, Bessen C, Sobczak C, Schmitz S, et al. Surveillance of Myelodysplastic Syndrome via Migration Analyses of Blood Neutrophils: A Potential Prognostic Tool. J Immunol 2018;201:3546–57.
[25] SeiderK, Brunke S, Schild L, Jablonowski N, Wilson D, Majer O, et al. The facultative intracellular pathogen Candida glabrata subverts macrophage cytokine production and phagolysosome maturation. J Immunol 2011;187:3072–86.
[26] Gonzalez RC, Woods RE. Digital Image Processing. 3rd ed. Pearson; 2007.
[27] Zuiderveld K. Contrast Limited Adaptive Histogram Equalization. Graph. Gems, Elsevier. 1994. 474–85.
[28] Sobel I. An Isotropic 3x3 Image Gradient Operator. Present Stanford AI Proj. 1968. 2014.
[29] Pomerantsev AL. Acceptance areas for multivariate classification derived by projection methods. J. Chemom. 22. John Wiley & Sons, Ltd. 2008. 601–9.
[30] Pomerantsev AL, Rodionova OY. Concept and role of extreme objects in PCA/SIMCA. J Chemom 2014;28:429–38.
[31] Pomerantsev AL, Rodionova OY. Popular decision rules in SIMCA: Critical review. J Chemom 2020;34.
[32] WOLD S, SJÖSTRÖM M. SIMCA: A Method for Analyzing Chemical Data in Terms of Similarity and Analogy. 1977. 243–82.
[33] TsugawaH, Tsujimoto Y, Arita M, Bamba T, Fukusaki E. GC/MS based metabolomics: development of a data mining system for metabolite identification by using soft independent modeling of class analogy (SIMCA). BMC Bioinf 2011;12:131.
[34] KhanmohammadiM, Nasiri R, Ghasemi K, Samani S, Bagheri GA. Diagnosis of basal cell carcinoma by infrared spectroscopy of whole blood samples applying soft independent modeling class analogy. J Cancer Res Clin Oncol 2007;133:1001–10.
[35] MasithohRE, Yuliyanda I. NIR reflectance spectroscopy and SIMCA for classification of crops flour. IOP Conf. Ser. Earth Environ. Sci., vol. 355, Institute of Physics Publishing. 2019. 012004.
[36] DrögeJBM, Rinsma WJ, Van 'T Klooster HA, Tas AC, Van Der Greef J. An evaluation of SIMCA. Part 2 — classification of pyrolysis mass spectra of pseudomonas and serratia bacteria by pattern recognition using the SIMCA classifier. J Chemom. 1987. 1. 231–41.
[37] MazivilaSJ, Páscoa RNMJ, Castro RC, Ribeiro DSM, Santos JLM. Detection of melamine and sucrose as adulterants in milk powder using near-infrared spectroscopy with DD-SIMCA as one-class classifier and MCR-ALS as a means to provide pure profiles of milk and of both adulterants with forensic evidence: A short communication. Talanta. 2020. 216. 120937.
[38] NevesMDG, Poppi RJ. Authentication and identification of adulterants in virgin coconut oil using ATR/FTIR in tandem with DD-SIMCA one class modeling. Talanta 2020;219:121338.
[39] Pearson K. LIII. On lines and planes of closest fit to systems of points in space. London, Edinburgh, Dublin Philos Mag J Sci 1901;2:559–72.
[40] Kucheryavskiy S. mdatools – R package for chemometrics. Chemom Intell Lab Syst 2020;198:103937.
[41] Hastie T, Tibshirani R, Friedman J. The Elements of Statistical Learning. New York, NY: Springer, New York; 2009.
[42] Michal Majka. naivebayes: High Performance Implementation of the Naive Bayes Algorithm in R. 2019.
[43] Wilcox RR, Erceg-Hurn DM. Comparing two dependent groups via quantiles. J Appl Stat 2012;39:2655–64.
[44] Harrell FE, Davis CE. A new distribution-free quantile estimator. Biometrika 1982;69:635–40.
[45] Mair P, Wilcox R. Robust statistical methods in R using the WRS2 package. Behav Res Methods. 2019. 522. 2019. 52. 464–88.
[46] Quade D. Using weighted rankings in the analysis of complete blocks with additive block effects. J Am Stat Assoc 1979;74:680–3.
[47] Holm S. A Simple Sequentially Rejective Multiple Test Procedure. Scand J Stat 1979;6:65–70.
[48] Pohlert P. PMCMRplus: Calculate Pairwise Multiple Comparisons of Mean Rank Sums Extended. R package version 1.4.4. 2020.
[49] McGraw KO, Wong SP. A Common Language Effect Size Statistic. Psychol Bull 1992;111:361–5.
[50] Dick J, Bolker B. canprot: Compositional Analysis of Differentially Expressed Proteins in Cancer. 2020.
[51] Hedges LV, Olkin I. Statistical Methods for Meta-Analysis. Orlando: Academic Press Inc (Verlag); 1985.
[52] Gibbons RD, Hedeker DR, Davis JM. Estimation of Effect Size From a Series of Experiments Involving Paired Comparisons. J Educ Stat 1993;18:271–9.
[53] Torchiano M. Effsize – A package for efficient effect size computation. 2016.
[54] Wilson EB. Probable Inference, the Law of Succession, and Statistical Inference. J Am Stat Assoc 1927;22:209–12.
[55] Agresti A, Coull BA. Approximate is better than "Exact" for interval estimation of binomial proportions. Am Stat 1998;52:119–26.
[56] PropCIs SR. Various confidence interval methods for proportions. R Packag Version 2018:03.
[57] Fleiss JL, Levin B, Paik MC. Statistical Methods for Rates and Proportions. John Wiley & Sons, Inc. 2003.
[58] Kohl M. MKpower: Power Analysis and Sample Size Calculation. 2020.
[59] Wilcox RR. Comparing Two Independent Groups Via Multiple Quantiles. Stat 1995;44:91–9.
[60] Hochreiter S, Schmidhuber J. Long Short-Term Memory. Neural Comput 1997;9:1735–80.
[61] WitkowskaE, Jagielski T, Kamin´ska A, Kowalska A, Hryncewicz-Gwóz´dz´ A, Waluk J. Detection and identification of human fungal pathogens using surface-enhanced Raman spectroscopy and principal component analysis. Anal Methods 2016;8:8427–34.
[62] LamLMT, Dufresne PJ, Longtin J, Sedman J, Ismail AA. Reagent-free identification of clinical yeasts by use of attenuated total reflectance fourier transform infrared spectroscopy. J Clin Microbiol 2019;57.
[63] NormandA-C, Gabriel F, Riat A, Cassagne C, Bourgeois N, Huguenin A, et al. Optimization of MALDI-ToF mass spectrometry for yeast identification: a multicenter study. Med Mycol 2020;58:639–49.
[64] PfeifferCD, Samsa GP, Schell WA, Reller LB, Perfect JR, Alexander BD. Quantitation of Candida CFU in initial positive blood cultures. J Clin Microbiol 2011;49:2879–83.
[65] ArendN, Pittner A, Ramoji A, Mondol AS, Dahms M, Rüger J, et al. Detection and Differentiation of Bacterial and Fungal Infection of Neutrophils from Peripheral Blood Using Raman Spectroscopy. Anal Chem 2020;92:10560–8.
[66] Lux F, Matula P. Cell Segmentation by Combining Marker-Controlled Watershed and Deep Learning. 2020.

[67] BadrinarayananV, Kendall A, Cipolla R. SegNet: A Deep Convolutional Encoder-Decoder Architecture for Image Segmentation. IEEE Trans Pattern Anal Mach Intell 2017;39:2481–95.
[68] YounY-J, Shrestha S, Lee Y-B, Kim J-K, Lee JH, Hur K, et al. Neutrophil-derived trail is a proinflammatory subtype of neutrophil-derived extracellular vesicles. Theranostics 2021;11:2770–87.
[69] MarkiA, Buscher K, Lorenzini C, Meyer M, Saigusa R, Fan Z, et al. Elongated neutrophil-derived structures are blood-borne microparticles formed by rolling neutrophils during sepsis. J Exp Med 2021;218.
[70] MoniciM, Pratesi R, Bernabei PA, Caporale R, Ferrini PR, Croce AC, et al. Natural fluorescence of white blood cells: spectroscopic and imaging study. J Photochem Photobiol B Biol 1995;30:29–37.
[71] MonselA, Lécart S, Roquilly A, Broquet A, Jacqueline C, Mirault T, et al. Analysis of autofluorescence in polymorphonuclear neutrophils: A new tool for early infection diagnosis. PLoS ONE 2014;9:e92564.
[72] BeyrauM, Bodkin JV, Nourshargh S. Neutrophil heterogeneity in health and disease: a revitalized avenue in inflammation and immunity. Open Biol 2012;2:120134.
[73] Silvestre-Roig C, Hidalgo A, Soehnlein O. Neutrophil heterogeneity: Implications for homeostasis and pathogenesis. Blood 2016;127:2173–81.
[74] Hong CW. Current understanding in neutrophil differentiation and heterogeneity. Immune Netw 2017;17:298–306.

3.3 Human neutrophils produce antifungal extracellular vesicles against *Aspergillus fumigatus*

FORMULAR 1

Manuskript Nr. (laufende Nummer in der Dissertation) **3**

Titel des Manuskriptes: Human Neutrophils Produce Antifungal Extracellular Vesicles against *Aspergillus fumigatus*.

Autoren: Shopova I. A., Belyaev I., Dasari P., Jahreis S., Stroe M.C., Cseresnyés Z., Zimmermann A.K., Medyukhina A., Svensson C.M., Krüger T., Szeifert V., Nietzsche S., Conrad T., Blango M.G., Kniemeyer O., von Lilienfeld-Toal M., Zipfel P. F., Ligeti E., Figge M. T., Brakhage A. A.

Bibliographische Informationen (falls publiziert oder zur Publikation angenommen: Zitat):

MBio, 2020; 11(2). DOI: 10.1128/mBio.00596-20

Der Kandidat / Die Kandidatin ist (bitte ankreuzen)

☐ Erstautor/-in, ☐ Ko-Erstautor/-in, ☐ Korresp. Autor/-in, ☒ Koautor/-in.

Status (falls nicht publiziert; „zur Publikation eingereicht“, „in Vorbereitung“):

Anteile (in %) der Autoren / der Autorinnen an der Publikation (anzugeben ab 20%)

Autor/-in	**Konzeptionell**	**Datenanalyse**	**Experimentell**	**Verfassen des Manuskriptes**	**Bereitstellung von Material**
Shopova I. A.	50	30	60	50	0
Belyaev I.	10	30	20	10	0
Others	40	40	20	40	100
Total:	100	100	100	100	100

AMERICAN SOCIETY FOR MICROBIOLOGY | mBio®

RESEARCH ARTICLE
Host-Microbe Biology

Human Neutrophils Produce Antifungal Extracellular Vesicles against *Aspergillus fumigatus*

Iordana A. Shopova,[a,b] Ivan Belyaev,[c,i] Prasad Dasari,[d] Susanne Jahreis,[e] Maria C. Stroe,[a,b] Zoltán Cseresnyés,[c] Ann-Kathrin Zimmermann,[a,b] Anna Medyukhina,[c] Carl-Magnus Svensson,[c] Thomas Krüger,[b] Viktória Szeifert,[f] Sandor Nietzsche,[g] Theresia Conrad,[h] Matthew G. Blango,[b] Olaf Kniemeyer,[b] Marie von Lilienfeld-Toal,[e] Peter F. Zipfel,[a,d] Erzsébet Ligeti,[f] Marc Thilo Figge,[a,c] Axel A. Brakhage[a,b]

[a]Institute of Microbiology, Friedrich Schiller University, Jena, Germany
[b]Department of Molecular and Applied Microbiology, Leibniz Institute for Natural Product Research and Infection Biology (HKI), Jena, Germany
[c]Research Group Applied Systems Biology, Leibniz Institute for Natural Product Research and Infection Biology (HKI), Jena, Germany
[d]Department of Infection Biology, Leibniz Institute for Natural Product Research and Infection Biology (HKI), Jena, Germany
[e]Clinic of Internal Medicine II, Haematology and Oncology, Jena University Hospital, Jena, Germany
[f]Department of Physiology, Semmelweis University, Budapest, Hungary
[g]Centre for Electron Microscopy, Jena University Hospital, Jena, Germany
[h]Research Group Systems Biology and Bioinformatics, Leibniz Institute for Natural Product Research and Infection Biology (HKI), Jena, Germany
[i]Friedrich Schiller University, Jena, Germany

ABSTRACT Polymorphonuclear granulocytes (PMNs) are indispensable for controlling life-threatening fungal infections. In addition to various effector mechanisms, PMNs also produce extracellular vesicles (EVs). Their contribution to antifungal defense has remained unexplored. We reveal that the clinically important human-pathogenic fungus *Aspergillus fumigatus* triggers PMNs to release a distinct set of antifungal EVs (afEVs). Proteome analyses indicated that afEVs are enriched in antimicrobial proteins. The cargo and the release kinetics of EVs are modulated by the fungal strain confronted. Tracking of afEVs indicated that they associated with fungal cells and even entered fungal hyphae, resulting in alterations in the morphology of the fungal cell wall and dose-dependent antifungal effects. To assess as a proof of concept whether the antimicrobial proteins found in afEVs might contribute to growth inhibition of hyphae when present in the fungal cytoplasm, two human proteins enriched in afEVs, cathepsin G and azurocidin, were heterologously expressed in fungal hyphae. This led to reduced fungal growth relative to that of a control strain producing the human retinol binding protein 7. In conclusion, extracellular vesicles produced by neutrophils in response to *A. fumigatus* infection are able to associate with the fungus, limit growth, and elicit cell damage by delivering antifungal cargo. This finding offers an intriguing, previously overlooked mechanism of antifungal defense against *A. fumigatus*.

IMPORTANCE Invasive fungal infections caused by the mold *Aspergillus fumigatus* are a growing concern in the clinic due to the increasing use of immunosuppressive therapies and increasing antifungal drug resistance. These infections result in high rates of mortality, as treatment and diagnostic options remain limited. In healthy individuals, neutrophilic granulocytes are critical for elimination of *A. fumigatus* from the host; however, the exact extracellular mechanism of neutrophil-mediated antifungal activity remains unresolved. Here, we present a mode of antifungal defense employed by human neutrophils against *A. fumigatus* not previously described. We found that extracellular vesicles produced by neutrophils in response to *A. fumigatus* infection are able to associate with the fungus, limit growth, and elicit cell damage by delivering antifungal cargo. In the end, antifungal extracellular vesicle biology

Citation Shopova IA, Belyaev I, Dasari P, Jahreis S, Stroe MC, Cseresnyés Z, Zimmermann A-K, Medyukhina A, Svensson C-M, Krüger T, Szeifert V, Nietzsche S, Conrad T, Blango MG, Kniemeyer O, von Lilienfeld-Toal M, Zipfel PF, Ligeti E, Figge MT, Brakhage AA. 2020. Human neutrophils produce antifungal extracellular vesicles against *Aspergillus fumigatus*. mBio 11:e00596-20. https://doi.org/10.1128/mBio.00596-20.

Editor Antonio Di Pietro, Universidad de Córdoba

Copyright © 2020 Shopova et al. This is an open-access article distributed under the terms of the Creative Commons Attribution 4.0 International license.

Address correspondence to Axel A. Brakhage, axel.brakhage@uni-jena.de.

This article is a direct contribution from Axel A. Brakhage, a Fellow of the American Academy of Microbiology, who arranged for and secured reviews by David Perlin, Hackensack Meridian Health Center for Discovery and Innovation, and James Kronstad, University of British Columbia.

Received 16 March 2020
Accepted 17 March 2020
Published 14 April 2020

provides a significant step forward in our understanding of *A. fumigatus* host pathogenesis and opens up novel diagnostic and therapeutic possibilities.

KEYWORDS *Aspergillus fumigatus*, azurocidin, cathepsin G, extracellular vesicle, fluorescent image analysis, fungi, microvesicle, neutrophils, polymorphonuclear leukocytes

The clinical management of invasive aspergillosis, a severe systemic infection mainly caused by the ubiquitous saprophytic fungus *Aspergillus fumigatus*, is a challenging endeavor. Invasive aspergillosis is characterized by high mortality rates related to the difficult diagnosis, the occurrence of resistance to antifungals, and the lack of novel antifungal therapies (1–6). Invasive aspergillosis can occur in patients with congenital or therapy-induced myeloid cell defects, whereas healthy individuals that continuously inhale fungal spores (conidia; 2 to 3 μm) usually remain symptom free. Data from neutropenic mice and patients have shown that polymorphonuclear granulocytes (PMNs) are indispensable for antifungal defense (7–16); however, the exact mechanism of PMN-dependent fungal killing remains unresolved.

PMNs orchestrate immune surveillance against pathogenic fungi via oxidative burst (14, 17, 18), degranulation (19, 20), phagocytosis (21), cytokine release (7), and extracellular trap formation (11, 16, 22, 23). Neutrophil extracellular traps are only slightly fungistatic, and this alone does not explain the full antifungal activity of PMNs (22, 23). In addition to these effector mechanisms, PMNs also produce PMN-derived extracellular vesicles (EVs), which represent extracellular phosphatidylserine-containing microparticles (50 nm to 1 μm) that elicit pleiotropic immunomodulatory effects in recipient host cells (24–28). PMN-derived EVs serve many functions *in vivo* (29–32), including antibacterial (33–35) and antiviral (36) defense, and have been used as diagnostic markers for sepsis (37). Previous work also indicated that opsonization of bacteria is required for the production of antibacterial PMN-derived EVs (34).

In this report, we demonstrate the immune functionality of PMN-derived EVs against the important filamentous fungal pathogen *A. fumigatus*. We phenotypically characterized the EVs produced by PMNs in response to *A. fumigatus* infection and further detail the properties, locations, and antifungal effects of these EVs on the fungus.

RESULTS

PMNs release EVs in response to *A. fumigatus* infection. The confrontation of PMNs with *A. fumigatus* conidia is known to result in the rapid internalization of the fungus and the production of reactive oxygen intermediates and neutrophil extracellular traps over time (22, 38). In response to opsonized bacterial pathogens, neutrophils have been shown to release antibacterial EVs (34, 39), yet the role of EVs in antifungal defense in mammals remains unexplored. As such, we enriched and characterized PMN-derived EVs produced from viable human PMNs (>95% purity, >98% viability) during infection with opsonized wild-type (wt) *A. fumigatus* conidia (see Fig. S1A in the supplemental material). To limit PMN apoptosis and the subsequent production of apoptotic bodies, we first determined the apoptotic fate of PMNs over the course of interaction with *A. fumigatus* by monitoring propidium iodide (PI) and annexin V staining of cells using flow cytometry (Fig. 1A). Both EVs and apoptotic cells expose on the outer leaflet of the cell membrane phosphatidylserine, which can be detected by annexin V. However, in contrast to apoptotic bodies, EVs remain intact and thus impermeable to PI (24–28). By size discrimination using flow cytometry, we could also distinguish between cellular apoptosis and the release of apoptotic bodies (annexin V-positive and PI-positive [PI^+] EVs) (Fig. 1A and Fig. S1B to E). Coincubation of human PMNs with fungi for 4 h at a multiplicity of infection (MOI) of 5 conidia to 1 PMN triggered minimal cell death in the PMN population (<10%) and limited apoptotic body release compared to an MOI of 10 (Fig. 1A). An MOI of 5 was thus used throughout the remainder of the study to phenotypically characterize PMN-derived EVs.

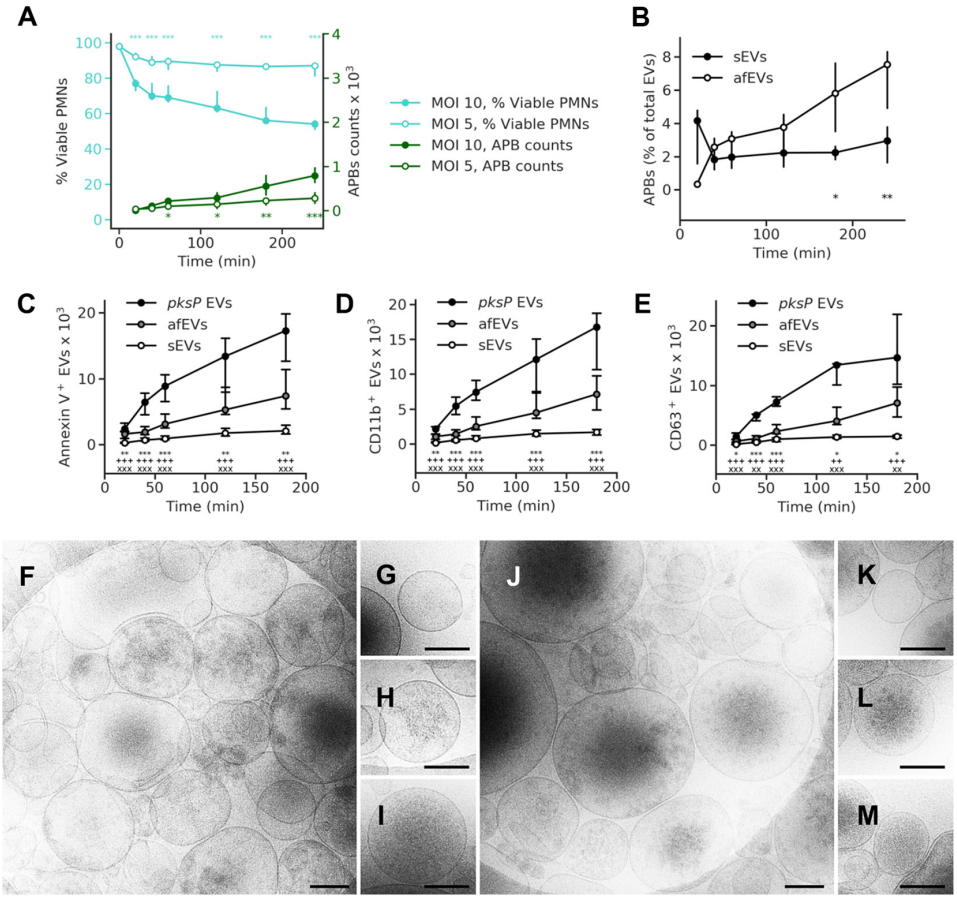

FIG 1 *A. fumigatus* induces EV release by human neutrophils. (A) Time course of apoptotic body (APB) occurrence (green lines) and fungus-induced cell death (teal lines) at MOIs of 5 and 10 ($n = 10$ [15] and $n = 12$ [17] for apoptotic body counts for MOIs of 5 and 10, respectively; $n = 4$ [20] and $n = 5$ [15] for viability data for MOIs of 5 and MOI 10, respectively) (numbers in brackets are total number of technical replicates). (B) Percentage of apoptotic bodies per total number of EVs. (C to E) Time course of total EV release and the levels of the EV surface markers annexin V ($n = 27$ [40] for sEVs, $n = 16$ for afEVs and *pksP* EVs) (C), CD11b ($n = 23$ for sEVs, $n = 16$ for afEVs and *pksP* EVs) (D), and CD63 ($n = 13$ for sEVs, $n = 9$ for afEVs and *pksP* EVs) (E). sEVs were collected from uninfected cells. Symbols represent significant differences between *pksP* EVs and afEVs (*), *pksP* EVs and sEVs (+), afEVs and sEVs (x). The data in panels A and B to E are presented as the medians and interquartile ranges of the absolute numbers of EVs per 10^7 PMNs. *P* values were determined by the Mann-Whitney test. *, $P < 0.05$; **, ++, and xx, $P < 0.01$; *** and xxx, $P < 0.001$. (F to M) Cryo-TEM images of sEVs (F to I) and afEVs (J to M) at 2 h postinteraction. Representative images display sEVs (G to I) and afEVs (K to M) with different appearances. Bars, 200 nm.

We were particularly interested in the phosphatidylserine-containing and PI-negative fraction of EVs, which was previously linked to host immunity and which can be interrogated by flow cytometry (24–28). Labeling of EVs with cell surface markers for the α-chain of the integrin receptor CR3 (CD11b) and the tetraspanin CD63 revealed an increase in the size of the populations of EVs produced in response to infection with wt *A. fumigatus* (antifungal EVs [afEVs]) relative to the size of the populations of spontaneously released EVs (sEVs) from uninfected cells (Fig. 1B to E; Fig. S1F and G and S2A and B). When we compared the afEV formation induced by stimulation of PMNs with wt and *pksP* mutant conidia, which lack the pigment and the virulence determinant dihydroxynaphthalene melanin (25, 40–43), we discovered that melanin-deficient conidia doubled the production of EVs analyzed here (Fig. 1C to E). This finding suggests that fewer EVs are produced against melanized wt conidia, consistent with a known repressive role for dihydroxynaphthalene melanin against the host immune response during infection (44). For clarity, we have defined EVs induced by wt conidia

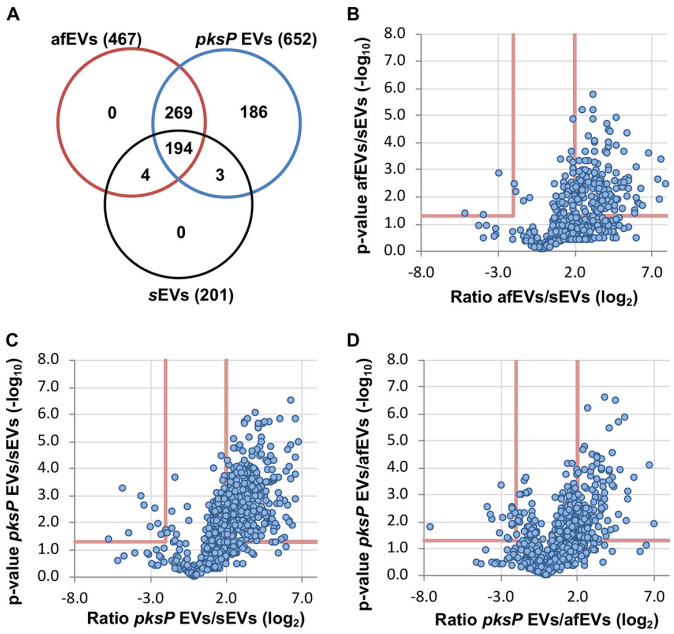

FIG 2 Analysis of the EV proteome by LC-MS/MS reveals that neutrophil-derived EVs retain a core proteome cargo after infection. (A) Venn diagram (created with Venny [version 2.1.0] software) indicating the overlap of proteins identified from each EV population using label-free quantification. (B to D) Volcano plots comparing proteins identified in afEVs, *pksP* EVs, and sEVs using the LFQ-based proteomics method.

as antifungal EVs (afEVs), EVs induced by *pksP* mutant conidia as *pksP* EVs, and spontaneously produced EVs as sEVs. Despite this major difference in EV production, PMN viability was similar for wt and *pksP* mutant conidium-infected cells (Fig. S2C); however, *pksP* conidia did exhibit higher opsonization (Fig. S2D) (42). The vesicular nature of the detected EVs was verified by detergent treatment using 1% (vol/vol) Triton X-100, which led to the disappearance of the signals for both annexin V and EV surface marker staining (Fig. S1F and G). Cryo-transmission electron microscopy (cryo-TEM) imaging (Fig. 1F to M) confirmed a heterogeneous population of circular structures with lipid bilayers for both afEVs and sEVs (26, 45). Both types of EVs appeared to contain cargo with different spatial organizations (Fig. 1G to I and K to M), including practically empty EVs (Fig. 1G and K), granular structures (Fig. 1H and L), and a homogeneous distribution of cargo (Fig. 1I and M). The meaning of the different grade of granularity awaits further attention.

afEVs are enriched for antimicrobial proteins. We next addressed the cargo of EVs in response to infection. We purified proteins from afEVs, *pksP* EVs, and sEVs from about 10 liters of fresh human blood. Equal amounts of protein were labeled with tandem mass tags (TMT) or left unlabeled for a subsequent label-free quantification (LFQ), followed by detection with nanoscale liquid chromatography (nLC)-tandem mass spectrometry (MS/MS); see the two data sets at https://doi.org/10.6084/m9.figshare.11973174). LFQ analysis revealed an expanded proteome in the afEVs and *pksP* EVs compared to the sEVs, which is suggestive of additional functionality (Fig. 2A). We next compared (i) *pksP* EVs and afEVs, (ii) afEVs and sEVs, and (iii) *pksP* EVs and sEVs. We observed that the afEVs and *pksP* EVs were, again, quite different from the sEVs, but even the afEVs differed from the *pksP* EVs (Fig. 2B to D). Analysis using the TMT method of quantification also indicated differences in each population, consistent with the LFQ data (Fig. S3A to C). Since EVs are often enriched for membrane proteins, we next predicted transmembrane domain-containing proteins using three different

TABLE 1 Selected examples of differentially produced proteins with known antimicrobial activity

UniProt accession no.	Protein	TMT ratio		
		pksP EVs/afEVs	afEVs/sEVs	*pksP* EVs/sEVs
A0A0U1RRH7	Histone H2A	1.32	14.08	18.55
U3KQK0	Histone H2B	1.12	6.27	7.04
P68431	Histone H3.1	0.82	16.84	13.79
P08246	Neutrophil elastase	0.62	4.64	2.86
P05164	Myeloperoxidase	1.19	2.16	2.57
P08311	Cathepsin G	0.73	3.07	2.24
P20160	Azurocidin	0.70	3.46	2.41
P59665	Defensin 1	2.04	13.41	27.37

tools (TMHMM [46], SignalP [47], and WoLF PSORT [48]) and identified 17 proteins in the TMT data set and 29 proteins in the LFQ data set (Table S1).

In comparison to sEVs, both afEVs and *pksP* EVs contained a broader spectrum of proteins and, more importantly, larger amounts of antimicrobial peptides, such as neutrophil elastase (NE), myeloperoxidase (MPO), cathepsin G, azurocidin, and defensin 1 (Table 1). CD11b and CD63 were enriched in afEVs and *pksP* EVs compared to sEVs, thus confirming the flow cytometry data (Fig. 1D and E; see the two data sets at https://doi.org/10.6084/m9.figshare.11973174). In addition, afEVs contained larger amounts of metabolic enzymes, such as glucose-6-phosphate isomerase and transketolase, the cell surface glycoprotein CD177, and F-actin. Proteins of the antimicrobial calprotectin complex (S100-A8, S100-A9) exhibited the highest absolute abundance in afEVs (see the two data sets at https://doi.org/10.6084/m9.figshare.11973174). Finally, afEVs and *pksP* EVs were more similar in protein content in comparison to that in sEVs (Table 1; see the two data sets at https://doi.org/10.6084/m9.figshare.11973174).

The comparison of the proteins from all EV subsets revealed that 60 proteins were shared between all groups, suggesting that these proteins are part of the core EV protein set. Gene Ontology (GO)-term enrichment analysis of the 60 shared proteins revealed the overrepresentation of proteins involved in Fcγ receptor signaling, Arp2/3 complex-mediated actin nucleation, the interleukin-8 signaling pathway, cytoskeletal rearrangements, and the positive regulation of actin polymerization (Fig. 2; Fig. S3D). In comparison to the findings described in the literature, we found 164 proteins in common between the study of Timar et al. (34) and this study. We detected 118 proteins unique to the study of Timar et al. (34) and 448 proteins unique to our study using LFQ-based proteomics. Infection with wt or *pksP* conidia led to the formation of afEVs and *pksP* EVs with distinct proteome cargos, characterized by increased levels of antimicrobial peptides and metabolic proteins. These findings suggest an antimicrobial function for afEVs.

afEVs influence fungal growth by inhibition of hyphal extension. To prove a potential antifungal activity of afEVs, we collected afEVs and *pksP* EVs from PMNs, coincubated them in different concentrations with resting conidia, and monitored fungal growth by confocal laser scanning microscopy (CLSM) (Fig. 3A and Fig. S4A and B). The area of objects (single hyphae or clusters) was considered the growth measure. The concentration of EVs was measured in "doses" and is more fully described in Materials and Methods. One dose of EVs was defined as the number of *pksP* EVs produced by 10^7 PMNs infected with *pksP* mutant conidia at 2 h postinfection. At this time point, we found a relatively large amount of produced EVs (Fig. 1C) associated with a relatively low fraction of apoptotic bodies (Fig. 1B). The doses for each condition were normalized according to abundance from the observations in Fig. 1C. The afEVs generated by PMNs infected with wt conidia strongly inhibited the growth of wt and *pksP* hyphae in all donors when higher doses of EVs were applied (Fig. 3B to E and Fig. S4C to F). These experiments revealed donor heterogeneity in response to four different blood donors, suggesting that the antifungal potential of EVs may differ between individuals. Higher (triple) doses of *pksP* EVs, as well as lower (single) doses of

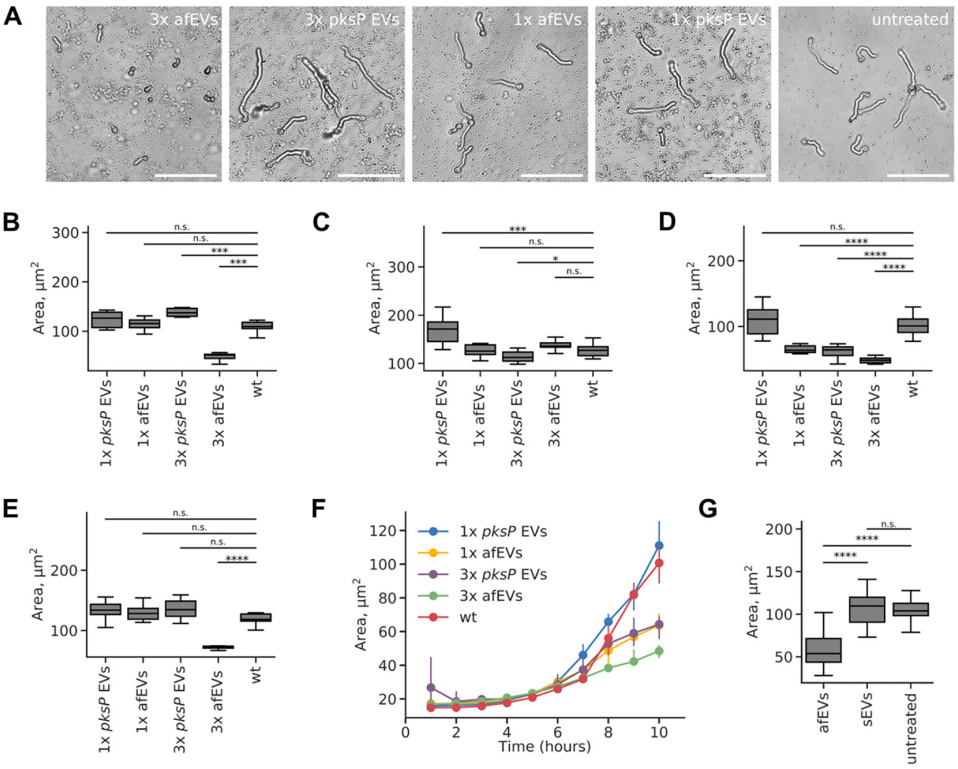

FIG 3 afEVs elicit antifungal effects on wt fungus. (A) Representative bright-field images after 10 h of incubation of wt fungal hyphae with afEVs and *pksP* EVs. Single (1×) or triple (3×) doses of EVs were applied. (B to E) Growth of wt fungal hyphae after 10 h of coincubation with afEVs and *pksP* EVs derived from four different donors. The size of the hyphae was assessed by automated analysis of 2D image data, and the results are displayed as the median hyphal area in each field of view; data are represented as medians and interquartile range of the median hyphal area in each field of view ($n = 10$ fields of view per condition per time point). (F) Representative growth curves of the wt fungal strain in the presence and the absence of EVs for the donor for which the results are shown in panel D. (G) Effects of sEVs on wt conidia compared to those of afEVs on wt conidia ($n = 3$ independent experiments, 20 fields of view per experiment per condition). *P* values were determined by the Mann-Whitney test. n.s., not significant; *, $P < 0.05$; ***, $P < 0.001$; ****, $P < 0.0001$.

afEVs, were efficient in the growth arrest of hyphal filaments for one donor only (Fig. 3D; Fig. S4E). The antifungal effects of afEVs for all donors were not due to the delayed germination of conidia but, rather, resulted from the inhibition of hyphal extension (Fig. 3A and F; Fig. S4A, B, and G). Interestingly, sEVs had no impact on the growth of fungi (Fig. 3G). Thus, PMNs produce tailored afEVs with distinct functional properties in response to coincubation with *A. fumigatus*.

afEVs associate with fungal cells. As discussed above, we observed that afEVs are capable of arresting fungal growth. To study the interactions of afEVs with fungi, we collected three-dimensional (3D) confocal fluorescent image stacks of wt hyphae coincubated with afEVs and *pskP* hyphae coincubated with *pksP* EVs after 20 h of incubation. We quantified the interactions of EVs and hyphae using 3D image analysis to evaluate the densities of EVs within (inside) calcofluor white-stained hyphae (in which the EV volume inside the hyphae was normalized to the hyphal volume) compared to the corresponding EV densities outside the hyphal cell wall determined by staining. The densities of EVs inside the hyphae (indicating an association with or internalization of the EVs) were significantly higher than the EV densities outside the hyphae (in which EVs were unassociated with the hyphae) for both wt and *pksP* hyphal filaments (Fig. 4A; see the first two movies at https://doi.org/10.6084/m9.figshare.11973174). The 3D image analysis of the fluorescence signals re-

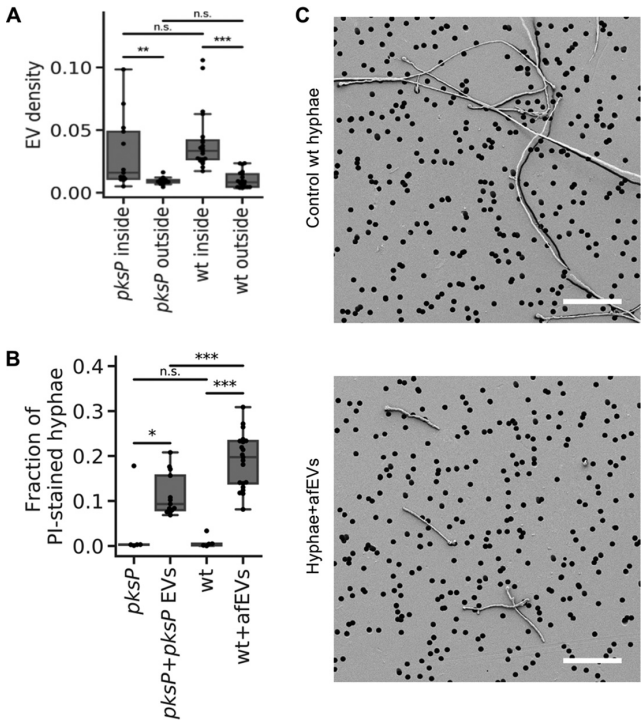

FIG 4 Effect of afEVs on hyphae. (A) Density of afEVs and *pksP* EVs inside and outside of wt and *pksP* mutant hyphae. (B) The fraction of PI-stained hyphae indicates permeable fungal hyphae and provides an estimation of the hypha-associated DNA signals in wt and *pksP* hyphae treated with afEVs and *pksP* EVs, respectively, compared to those in untreated control hyphae. The data in panels A and B for the EV groups were derived from 3 independent experiments ($n = 13$ and 21 technical replicates for *pksP* and wt, respectively). The data in panel B for the controls are representative of those from 1 experiment ($n = 5$ technical replicates). *P* values were determined by the Mann-Whitney test. n.s., not significant; *, $P < 0.05$; **, $P < 0.01$; ***, $P < 0.001$. (C) SEM images of 50-h-old cultures of wt hyphae treated with afEVs (bottom) versus healthy hyphae grown alone (top). Samples were immobilized on filter membranes with a defined pore size of 5 μm (black circles). Bars, 50 μm. SEM images represent observations from 2 independent experiments with 3 technical replicates.

vealed the extensive binding of EVs induced by conidia of both fungal strains to hyphae, despite the interrogation of equal volumes of EVs and hyphae (Fig. S5A and B).

We further assessed the ability of afEVs to associate with hyphae by evaluating the volume of hypha-associated EVs, which were defined as the sum of the volumes of afEVs bound to the cell wall or internalized into hyphae (see the first two movies at https://doi.org/10.6084/m9.figshare.11973174). The ability of afEVs to associate with hyphae was mainly dependent on the intrinsic properties of the donors' afEVs (Fig. S5C), while the relative volume density of afEVs had a much smaller effect (Fig. S5D and E). We next defined hypha-associated DNA staining as PI^+ signals colocalized with hyphae, which is indicative of hyphal cell damage. The amount of hypha-associated DNA staining from hyphae incubated with afEVs was significantly larger than the amount of hypha-associated DNA staining from control hyphae grown alone, as quantified by the hypha-associated DNA staining-positive volume normalized to the hyphal volume (Fig. 4B; see the second movie at https://doi.org/10.6084/m9.figshare.11973174). The 3D image analysis also showed that PI^+ staining of hyphae was associated with the interaction of hypha-associated EVs. In fact, more than 60% of the volume of PI^+ hyphae was associated with hypha-associated EVs (Fig. S5E; see the second movie at https://doi.org/10.6084/m9.figshare.11973174). All donor EVs were capable of eliciting PI staining of hyphae, but the extent of this effect was donor dependent (Fig. S5E). Our data imply that afEVs are antifungal and appear to cause cell

damage in a process likely associated with the physical interaction of hyphae and afEVs. In support of this finding, hyphae also appear to undergo hyperbranching away from the afEV layer in response to treatment (see the third movie at https://doi.org/10.6084/m9.figshare.11973174), again suggesting antifungal activity.

The effect of afEVs on fungi led us to test for physical long-term alterations of cell wall morphology. To visualize these changes, we obtained scanning electron microscopy (SEM) images of wt hyphae at 50 h after afEV treatment. The treated hyphal filaments (Fig. 4C) were again shorter, further confirming the antifungal nature of afEVs. Additional imaging showed slight alterations in the porousness of the cell surface, which included ruffling and invaginations that were not observed in hyphae grown without afEVs (Fig. S6).

Next, we took advantage of a previously reported mitochondrial green fluorescent protein (GFP) cell death reporter strain (AfS35/pJW103) produced to monitor the granulocyte killing of *A. fumigatus* (49). In this strain, a mitochondrion-localized GFP indicates filamentous, healthy mitochondria in living fungi, but the mitochondria become fragmented upon initiation of cell death pathways and ultimately lose their fluorescence at later time points. Using this strain, we were able to observe mitochondrial fragmentation and the limited growth of 20-h-old hyphae challenged with afEVs or an H_2O_2 control (3 mM) but not of those challenged with *pksP* EVs or sEVs (Fig. 5). These results are consistent with a potential fungicidal activity for afEVs and agree with the results from Fig. 3.

To further support our findings of afEVs in association with fungal cells, we performed 3D image analysis of afEV entry into GFP-expressing hyphae. The data obtained demonstrated that afEVs could be incorporated into the fungal cytoplasm (Fig. 6A to D; see the second movie at https://doi.org/10.6084/m9.figshare.11973174). Furthermore, we were able to differentiate four locations of EV-fungal interactions: (i) the largest fraction of afEVs, 50 to 70% (referred to as type I afEVs), were cell wall-associated EVs; (ii) afEVs embedded into the cell wall amounted to 0.5 to 2.5% of the EVs; (iii) 15 to 45% of the afEVs were found to be located at the interface between the cell wall and the cytoplasm; and (iv) intracytoplasmic afEVs represented 0.2 to 3% of all afEVs (Fig. 6A to D; see also the second movie at https://doi.org/10.6084/m9.figshare.11973174).

afEV proteins are toxic to fungal cells. We next assessed whether the antimicrobial proteins found in afEVs might contribute to the growth inhibition of hyphae when expressed heterologously in the fungus. The genes of two of these human proteins, cathepsin G and azurocidin, were selected because both proteins were enriched in afEVs and are also known to have antifungal effects. For example, cathepsin G knockout mice are highly susceptible to *A. fumigatus* infection (50, 51). The genes encoding these proteins were placed under inducible expression in *A. fumigatus* hyphae (Fig. S7A and B). As a control, we also placed the human retinol binding protein 7 (RBP7), a protein detected in EVs with no expected antifungal activity, under inducible expression in *A. fumigatus* hyphae as well (strain AfRBP7). Addition of the inducer doxycycline to cultures of the transgenic *A. fumigatus* strains (strains AfcathG and Afazuro) led to a massive growth reduction, whereas the control RBP7 strain (AfRBP7) revealed no change in dry weight (Fig. 7A and B). These findings are consistent with a potential activity of EV cargo proteins in limiting fungal growth when active in the fungus. The presence of the human proteins in hyphae after induction with doxycycline was confirmed by liquid chromatography (LC)-mass spectrometry (MS) measurements of fungal protein extracts (Fig. 7C).

DISCUSSION

Neutrophils are critical for the elimination of *A. fumigatus* from the human host (52); however, the exact extracellular mechanisms of how PMNs kill *A. fumigatus* hyphae are not known (52). *A. fumigatus*-triggered neutrophil extracellular traps are slightly fungistatic but do not account for the full activity of neutrophils (22, 23). Here, we show that *ex vivo*-applied human EVs triggered by wt conidia (afEVs) inhibit the growth of hyphae and elicit cell damage, adding a new mode of antifungal defense against *A.*

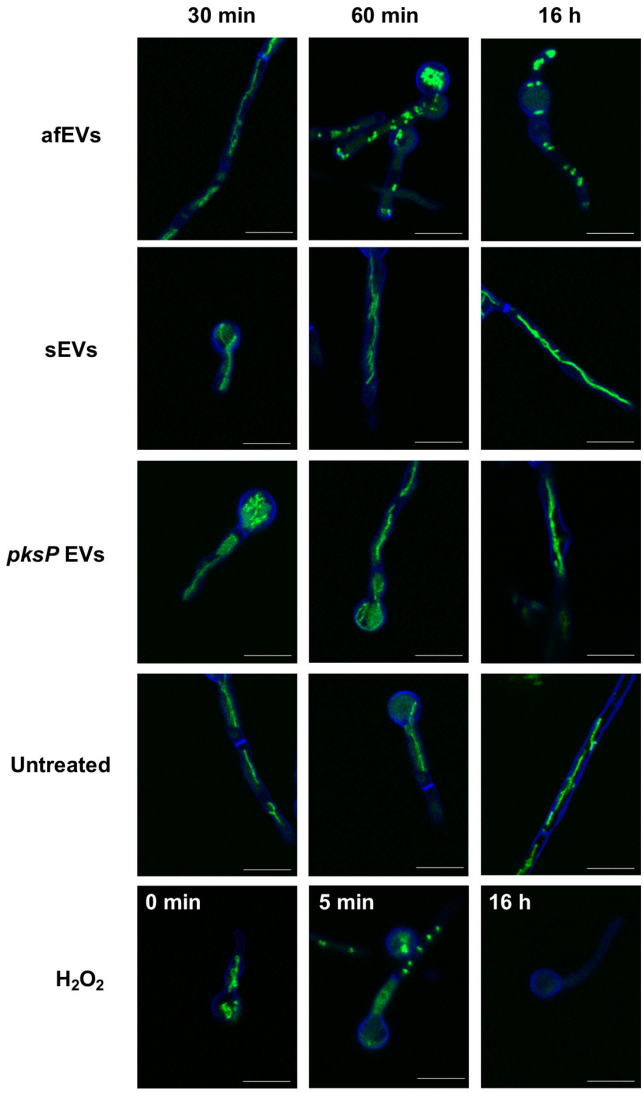

FIG 5 afEVs kill fungal hyphae. AfS35/pJW103 hyphae expressing a mitochondrial GFP reporter (green) grown for 20 h were stained with calcofluor white (blue) and incubated with sEVs, afEVs, *pksP* EVs, or 3 mM H_2O_2 as a positive control for cell death induction or left untreated and then monitored by CLSM. A healthy filamentous mitochondrial network is shown in green in an untreated sample. A fragmented mitochondrial network indicates cell death, as seen when 3 mM H_2O_2 was used as a positive control for cell death. Images are representative of those from 4 separate experiments with samples from different donors. Bars, 10 μm.

fumigatus. These results are consistent with previous findings from PMN-derived EVs showing antibacterial effects against *Staphylococcus aureus* (34). We speculate that afEVs are produced primarily as a result of fungus-driven PMN activation, as apoptotic bodies accounted for less than 10% of the total EV population.

afEV production was increased in response to *A. fumigatus* infection, as confirmed by flow cytometry. EVs increased with kinetics different from those previously reported for anti-*S. aureus* PMN-derived EVs, where maximum production was observed at 20 min (34). The interaction of PMNs with *A. fumigatus* conidia resulted in an enrichment of CD63 on afEVs, which was not observed in antibacterial EVs (34) and which is typically found only on EVs smaller than 100 nm. afEVs were also enriched in MPO, NE, and

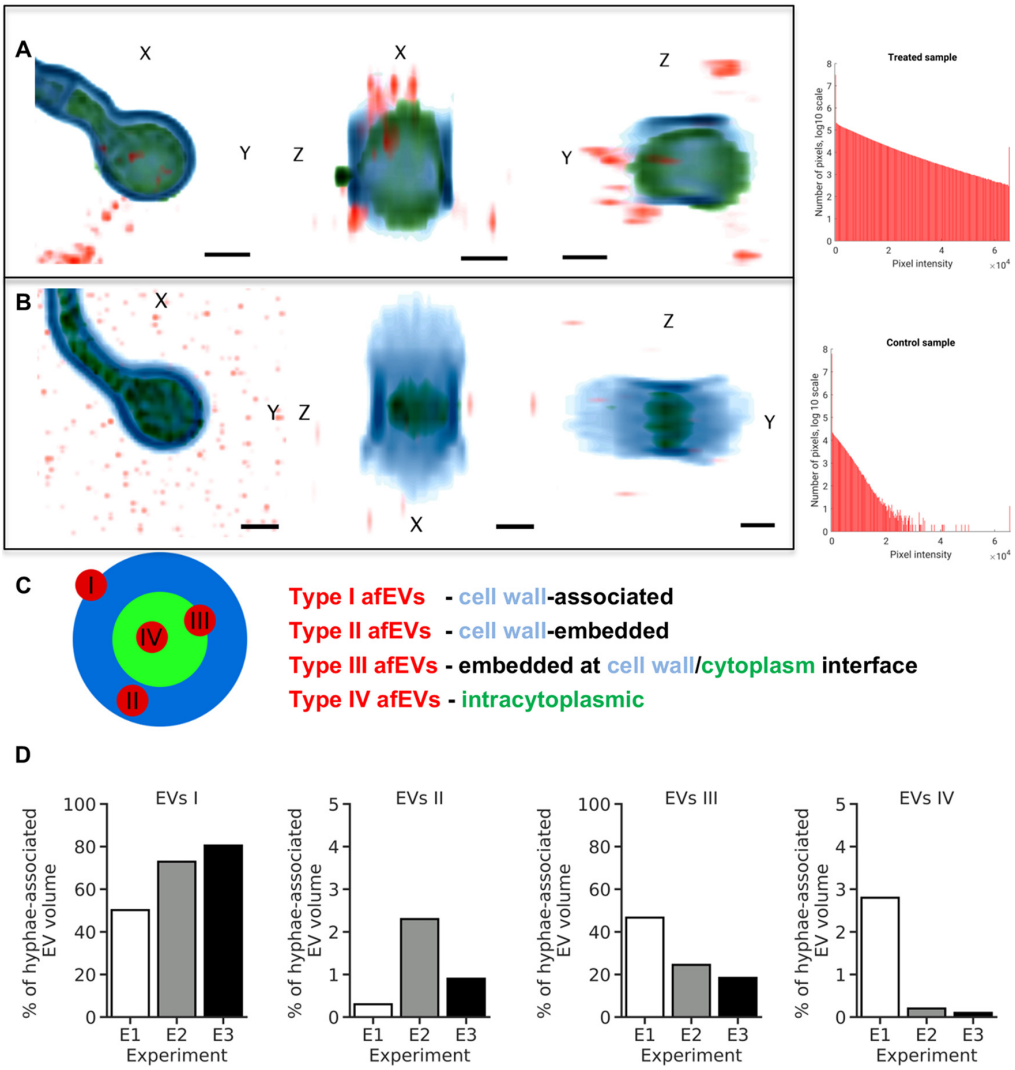

FIG 6 afEVs are internalized into the fungal cell wall and cytoplasm. afEV internalization into fungi was analyzed by 3D quantitative analysis of z-stacks with GFP-expressing *A. fumigatus* after 20 h of coincubation. (A, B) (Left) Representative cross sections of z-stacks showing lateral (*X* and *Y*) and axial (*Z*) dimensions of a hypha with internalized afEVs (A) and the corresponding control hypha (B). Internalized afEVs are in red (Alexa Fluor 647), the fungal cell wall is in blue (calcofluor white), and the fungal cytoplasm is in green (GFP). The image intensity was inverted. The darkest color corresponds to the highest fluorescence intensity. Bars, 2 μm. (Right) Histograms display the specificity of the signal of the Alexa Fluor 647 dye used to stain afEVs. As seen in the control z-stack, there is unspecific Alexa Fluor 647 staining, likely due to dye aggregation. (C) Schematic diagram of a cross section of hyphae and different stages of afEV internalization. afEVs were located in 4 areas, as indicated by the graphical representation. (D) Overview from the 3D image analysis of different locations of afEVs. Data are representative of those from 3 independent experiments with a total of 25 z-stacks.

cathepsin G, consistent with their antifungal function. Interestingly and further supporting the importance of the afEV cargo was the finding that cathepsin G, NE, and calprotectin knockout mice are all highly susceptible to infection with *A. fumigatus* (11, 50). It is possible that these proteins serve an EV-independent role in host defense; however, many of these proteins have been shown to be associated with EVs in our study and previous studies (26, 34).

Our proteomic analysis of EVs indicated that afEVs and *pksP* EVs contained an expanded proteome compared to that in sEVs; however, nearly all proteins from afEVs were found in *pksP* EVs. Despite this overlap, the abundance of these cargo proteins

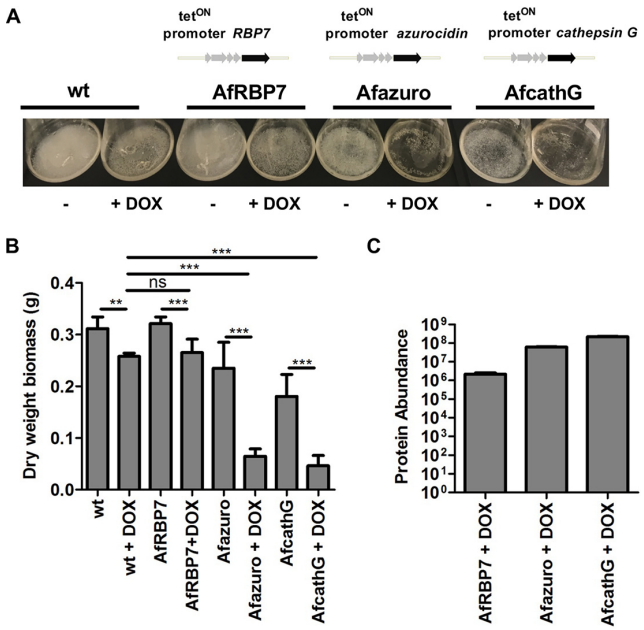

FIG 7 The intracellular production of human azurocidin and cathepsin G proteins is toxic to *A. fumigatus*. (A) *A. fumigatus* wt and mutant strains Afazuro, AfcathG, and AfRBP7 harboring the human azurocidin, cathepsin G, and *RBP7* genes, respectively, under the control of the tet^{ON} promoter. The cultures were grown for 24 h in the absence or the presence of doxycycline (DOX). (B) Biomass measurement of wt and *A. fumigatus* mutant strains Afazuro, AfcathG, and AfRBP7 with and without doxycycline. Data are representative of those from 3 independent experiments with 3 technical replicates. *P* values were determined by the Mann-Whitney test. ns, not significant; **, $P < 0.01$; ***, $P < 0.001$. (C) Detection of proteins produced in the *A. fumigatus* mutant strains. The bar plot shows the abundance level of the azurocidin protein for the Afazuro strain, the cathepsin G protein for the AfcathG strain, and RBP7 for the AfRBP7 strain, based on the intensity of the precursor ion. The data were generated from 3 analytical replicates.

was quite different. These results are consistent with a hypothesis that the abundance of EV cargo proteins dictates the antifungal nature of that EV population. Our results also suggest that the cargo of afEVs is tailored to the pathogen, as wt and *pksP* conidia elicited different responses. It is important to note that the *pksP* mutant utilized in these studies is not a knockout but instead was derived from a UV-mutagenized strain (53). Previous work has indicated that the phenotypes observed with this strain are due to the inactivation of *pksP* and that they could be fully complemented by the wt *pksP* gene (42, 53). Our findings also suggest a novel function for the fungal virulence factor dihydroxynaphthalene melanin (54, 55) in modulating EV biogenesis and protein cargo. Melanized conidia are less opsonized than nonmelanized conidia and, as a consequence, show reduced phagocytosis by neutrophils, which might lead to lower levels of EV production (42). This hypothesis is also supported by the observation that CD11b and CD63 receptors are differentially expressed on the surface of neutrophils during confrontation with *pksP* and wt conidia.

Our results demonstrate that afEVs associate with fungal hyphae, as evidenced by the high proportion of EVs colocalized with the cell wall of the fungus. In addition, since EVs were found intracellularly, inhibition and killing of the fungus might be due to a combination of these adherence and penetration mechanisms. Although we do not know the mechanisms that govern EV uptake, one hypothesis is that the Fcγ receptor found on the surface of EVs directs the EVs to opsonized fungal surfaces to facilitate entry. Once associated, the exact cargo that is required for the observed antifungal activity is also unknown at this time, but we suspect that it is due to a combination of factors. Human primary neutrophils cannot be genetically manipulated, so as a proof of

principle, we instead created *A. fumigatus* strains that produce cathepsin G and azurocidin using an inducible promoter system. The production of these proteins in the fungus clearly led to a massive growth defect, suggesting that delivery of these cargos could contribute to antifungal activity; however, this experiment offers only a proof of principle. In addition, we observed that fungal hyphae move away from afEVs by hyperbranching, suggesting that the fungus actively avoids afEVs. This finding is consistent with other observations of hyperbranching away from neutrophils during infection (56).

Our 3D image analysis and work with a mitochondrial GFP reporter strain illustrated the potential of afEVs to induce fungal cell damage, while they also revealed the afEV association with hyphae and a possible fungicidal capacity. Interestingly, PMN-generated reactive oxygen species (ROS) were recently shown to induce fungal cell death (14), and perhaps there is a connection between ROS-induced fungal cell death and afEV toxicity. More work will be required to fully elucidate the mechanism of fungal killing by afEVs. Our data did show that the intracellular production of antimicrobial peptides could contribute to a severe inhibition of fungal growth. On the other hand, neutrophil EV-associated effector functions are also known to contribute to innate immune pathology. For example, the surface-bound neutrophil elastase of EVs has been shown to cause extracellular matrix destruction and disease in the lungs of patients with chronic obstructive pulmonary disease (57).

In conclusion, our results suggest that human PMNs release afEVs in response to an *A. fumigatus* infection. These EVs contain a cargo of antimicrobial proteins that inhibit hyphal growth and kill hyphae. We envision that the analysis of EVs produced in bronchoalveolar lavage fluid represents a potentially useful tool for diagnostic and/or prognostic markers of invasive aspergillosis. Although we hypothesize that afEVs serve as an important factor in the control of pathogenesis during *A. fumigatus* infection, much work remains to be done to completely unveil the function of these important intercellular mediators.

MATERIALS AND METHODS

Ethics statement. This study was approved by the Institutional Review Board of the Jena University Hospital (approval numbers 2395-10/08 and 5074-02/17) in agreement with the Declaration of Helsinki. Informed consent was obtained for study participation. PMNs were isolated from fresh venous blood collected from healthy adult volunteers after obtaining written consent.

Strains, growth conditions, and fungal biomass determination. *A. fumigatus* ATCC 46645, the GFP-expressing strain AfS148 (58), the melanin-free *pksP* mutant (53), and the mitochondrial GFP reporter strain AfS35/pJW103 (49) were maintained on malt extract (Sigma-Aldrich) agar plates supplemented with 2% (wt/vol) agar for 5 days at 37°C. When appropriate, *A. fumigatus* ATCC 46645 and the overexpression strains *A. fumigatus* Afazuro, AfcathG, and AfRBP7 were cultivated on *Aspergillus* minimal medium (AMM) for 3 days at 37°C, as described previously (59). All conidia were harvested in sterile deionized water, filtered through 40-μm-pore-size cell strainers (BD Biosciences, Heidelberg, Germany), washed, and resuspended in deionized sterile water. Spore suspensions were counted in a Thoma chamber and stored at 4°C for no longer than 1 week. Freshly harvested spore suspensions were used for each experiment.

For biomass determination, 10^8 conidia/ml were inoculated in 100 ml AMM, supplemented with 10 μg/ml doxycycline when needed for induction of the tetracycline-controlled transcriptional activation (tet^{ON}) promoter, and grown at 37°C at 200 rpm for 24 h. Mycelia were collected, washed, filtered through Miracloth, and dried at 60°C for 3 days before weighing.

Opsonization of fungi. Fresh venous blood was drawn from adult male healthy volunteers, aged 20 to 35 years, after they provided informed written consent and used for preparation of normal human serum (NHS). The volunteers had not taken any anti-inflammatory medications for >10 days and had not consumed alcohol for >3 days prior to donation. NHS was obtained by pooling serum prepared from fresh venous blood from seven healthy human donors. The serum was stored at −80°C until use. The conidia were opsonized in 50% (vol/vol) NHS and 50% (vol/vol) Hanks' balanced salt solution (HBSS) (HyClone, GE Healthcare) for 1 h at 37°C at 500 rpm in duplicate. The conidia were pelleted by centrifugation at 16,000 × *g* at 4°C for 10 min and subsequently washed three times with HBSS prior to confrontation assays with PMNs.

To measure C3 deposition on the conidial surface after opsonization, the conidia were washed three times with Dulbecco's phosphate-buffered saline (DPBS) and then incubated with a 1:1,000 dilution of polyclonal goat anti-human C3 serum (Comptech) in 3% (wt/vol) bovine serum albumin (BSA) for 1 h at room temperature (RT). This was followed by addition of a 1:400 dilution of Alexa Fluor 647-conjugated donkey anti-goat IgG (Invitrogen) secondary antibody in 3% (wt/vol) BSA for 1 h at RT. The fluorescence of 10,000 conidial cells was measured by flow cytometry (with a BD LSR II flow cytometer), and the

median fluorescence intensity of each conidial population was calculated using FlowJo software (Becton, Dickinson, USA).

PMN isolation. PMNs were isolated from fresh venous blood from healthy adult volunteers with a purity above 95% and a viability at 98% as previously described in detail (26) with slight modifications, as follows: blood was collected in K_2EDTA BD Vacutainer tubes (BD Biosciences), and Biocoll separation solution (Biochrom; GE Healthcare) or PolymorphPrep solution (Progen) was used for gradient centrifugation. Neutrophil purity was determined using an antibody cocktail, as follows: CD3-phycoerythin (clone SK7; dilution, 1:50), CD14-V500 (clone M5E2; dilution, 1:200), CD16-allophycocyanin (APC)-Cy7 (clone 3G8; dilution, 1:50), CD19-Alexa Fluor 700 (clone HIB19; dilution, 1:100), CD56-fluorescein isothiocyanate (FITC) (clone NCAM16.2; dilution, 1:100), and CD66b-peridinin chlorophyll protein (PerCP)-Cy5.5 (clone G10F5; dilution, 1:66), obtained from BD Pharmingen, and CCR3-APC (clone 5E8; dilution, 1:40), obtained from BioLegend. The cells (1×10^6) were blocked with 5% (vol/vol) mouse serum and then stained for CCR3 for 10 min at 37°C. Subsequently, an antibody cocktail mix was applied for staining of the remaining antigens from the above-mentioned panel for an additional 30 min at RT. For cell damage assays at each time point, 2×10^6 neutrophils in 200 μl of HBSS were incubated with PI (5 μg) and Alexa Fluor 647-annexin V (5 μl) for 15 min at RT. Then, the cells were centrifuged at $400 \times g$ for 5 min and resuspended in 500 μl DPBS. The fluorescence of 10^4 gated neutrophils was measured by flow cytometry with a BD LSR II flow cytometer (BD Biosciences) and BD FACSDiva software (version 8.0.1; BD Biosciences). The data were analyzed with FlowJo software.

EV isolation and characterization. EVs were prepared by following a procedure described by Timar et al. (34) with slight modifications. PMNs at a density of 1×10^7 cells/ml were confronted with opsonized wt *A. fumigatus* ATCC 46645 or opsonized *A. fumigatus pksP* mutant conidia at an MOI of 10 or 5 in HBSS with Ca^{2+} and Mg^{2+} (HyClone, GE Healthcare) on a linear shaker (100 rpm) at 37°C for 4 h. EVs produced by uninfected PMNs (sEVs) served as a negative control. At the selected incubation time points, PMNs were sedimented for 10 min at $1{,}000 \times g$ at 4°C on 45° fixed-angle rotor (model FA-45-30-11; Eppendorf). The supernatant was filtered by gravity through sterile polyvinylidene difluoride (PVDF) 5.0-μm-pore-size Millex syringe filters (Merck-Millipore). The EV suspensions were stained with a cocktail of fluorescence-conjugated monoclonal antibodies (PerCP-Cy5.5-anti-human CD63 [clone H5C6; BioLegend], RPE-CD11b [Dako], and FITC-annexin V [BioLegend]) for 20 min at RT and centrifuged on a 45° fixed-angle rotor (model FA-45-30-11; Eppendorf) for 20 min at 4°C at $19{,}500 \times g$. Corresponding single-stained antibody isotype controls were also prepared (PerCP-Cy5.5 mouse IgG1, κ isotype [clone MOPC-21; BioLegend]; mouse IgG1, κ isotype RPE-CD11b [Dako]). After centrifugation, the supernatant was carefully aspirated and EV pellets were resuspended in the original incubation volume in HBSS.

The size distribution of PMN-derived EVs was recorded with a Nanotrac Flex 180° dynamic light scattering system (Microtrac) at 22°C. At least 20 measurements per sample were performed, and the average hydrodynamic radius was calculated with the sphere approximation using FLEX11 software.

Flow cytometry measurements of EVs were conducted on a BD LSR Fortessa flow cytometer using BD FACSDiva software (version 8.0.1) (BD Biosciences), applying an optimized EV flow protocol (60). Briefly, pure HBSS was used to record instrument noise. The upper size limit detection threshold was set by fluorescent rainbow particles with a midrange intensity and a size of 3.0 to 3.4 μm (BioLegend) resuspended in HBSS. Stained EV suspensions were enumerated in the fluorescent gate above the gate of the negative isotype-labeled controls. Once measured, samples were treated with 1% (vol/vol) Triton X-100 to verify the vesicular nature of the detected events. Detergent-resistant events (false positives) were subtracted from the total measured events using FlowJo software (version 10.0.7) from TreeStar.

Electron microscopy (cryo-TEM and SEM). For ultrastructural investigations, isolated EVs were imaged by cryo-transmission electron microscopy (cryo-TEM), and the effects of EVs on fungi were studied by scanning electron microscopy (SEM).

For cryo-TEM imaging, sEVs and afEVs collected at the time point of 2 h were freshly prepared using neutrophils from the same male donor and immediately subjected to imaging. Five microliters of purified pelleted EVs in HBSS was applied to carbon-coated copper grids (type R1.2/1.3; Quantifoil Micro Tools GmbH), and the excess liquid was blotted automatically for 2 s from the reverse side of the grid with a strip of filter paper. Subsequently, the samples were rapidly plunged into liquid ethane (cooled to −180°C) in a cryobox (Carl Zeiss NTS GmbH). Excess ethane was removed with a piece of filter paper. The samples were transferred with a cryo-transfer unit (Gatan model 626-DH) into the precooled cryo-TEM (Philips model CM 120), operated at 120 kV, and viewed under low-dose conditions. The images were recorded with a 2k complementary metal oxide semiconductor (CMOS) camera (model F216; TVIPS, Gauting, Germany).

SEM analysis was used to investigate the effect of the afEVs on the growth of *A. fumigatus*. Therefore, wt conidia were coincubated with the triple dose of PMN-derived EVs for 50 h in HBSS at 37°C in the dark. At the end of the coincubation time, samples were fixed in 2.5% (vol/vol) glutaraldehyde in HBSS on Isopore membrane TMTP filters with a pore size of 5 μm (Merck-Millipore) for 30 min, followed by washing thrice with HBSS buffer (for 10 min each time). Then, the samples were dehydrated in ascending ethanol concentrations (30, 50, 70, 90, and 96% [vol/vol]) for 10 min at each concentration by thoroughly rinsing the membranes and soaking up the liquids with blotting paper. Subsequently, the ethanol was changed to hexamethyldisilazane (Merck) in two steps (50%, 96% [vol/vol]), and the samples were air dried. Afterwards, the samples were sputter coated with gold (thickness, approximately 4 nm) using an SCD005 sputter coater (Bal-Tec, Liechtenstein) to avoid surface charging and investigated with a field emission (FE) SEM LEO-1530 Gemini microscope (Carl Zeiss NTS GmbH).

LC-MS/MS-based proteome analysis of EVs. For proteome analysis of EVs, purified sEVs, afEVs, and *pksP* EVs were collected from a pool of 20 different donors in HBSS and stored at −80°C for no longer

than 1 week prior to protein extraction. EV suspensions were concentrated on 3-kDa-molecular-mass-cutoff polyethersulfone (PES) membrane centrifugal filters (VWR International) for 5 min at 14,000 rpm at 4°C (Sigma 3-KIS centrifuge). Samples were snap frozen in liquid N_2 and delipidated by protein precipitation, based on the protocol of Wessel and Flügge (61). Proteins were resolubilized in 50 μl 50 mM triethyl ammonium bicarbonate (TEAB) in 1:1 trifluoroethanol (TFE)-H_2O and denatured for 10 min at 90°C. Protein quantification was performed using a Direct Detect system (Merck-Millipore). Each sample was set to 40 μg of total protein in 100 μl in 100 mM TEAB. Proteins were reduced with 10 mM Tris(2-carboxyethyl)phosphine (TCEP) at 55°C for 60 min and alkylated with 12.5 mM iodoacetamide (IAA) at RT for 30 min in the dark. Proteins were digested for 2 h at 37°C with C-type lysozyme (Lys-C) and for 16 h at 37°C with trypsin gold (both from Promega). For TMT 6-plex labeling (Thermo Fisher Scientific, Waltham, MA), the digested peptides were treated according to the manufacturer's instructions. Labeled peptides were pooled and fractionated offline on HyperSep strong-cation-exchange (SCX) columns (Thermo Fisher Scientific).

LC-MS/MS analyses and protein database searches were performed as described by Baldin et al. (62) with the following modifications. Gradient elution using eluent A (0.1% [vol/vol] formic acid in water) and eluent B (0.1% [vol/vol] formic acid in 90:10 acetonitrile-water [vol/vol]) was as follows: 0 to 4 min at 4% eluent B, 15 min at 5.5% eluent B, 30 min at 7% eluent B, 220 min at 12.5% eluent B, 300 min at 17% eluent B, 400 min at 26% eluent B, 450 min at 35% eluent B, 475 min at 42% eluent B, 490 min at 51% eluent B, 500 min at 60% eluent B, 515 to 529 min at 96% eluent B, and 530 to 600 min at 4% eluent B. Precursor ions were measured in full scan mode within a mass range of *m/z* 300 to 1,500 at a resolution of 140,000 full width at half maximum (FWHM) using a maximum injection time of 120 ms and an automatic gain control (AGC) target of 3×10^6 (TMT) or 1×10^6 (LFQ). The isolation width was set to *m/z* 0.8 (TMT) or 2.0 (LFQ) atomic mass units. Tandem mass spectra were searched for by the use of Proteome Discoverer (PD) software (version 2.1; Thermo Fisher Scientific, Waltham, MA) against the UniProt database of *Homo sapiens* (as of 22 August 2016) using the algorithms of the programs Mascot (version 2.4.1; Matrix Science), Sequest HT, and MS Amanda (63). Dynamic modifications were oxidation of Met (LFQ) and a TMT 6-plex reaction at Tyr (not considered for quantification). Static modifications were the carbamidomethylation of Cys by iodoacetamide (LFQ) and a TMT 6-plex reaction at Lys and the peptide N terminus. The TMT significance threshold for differentially abundant proteins was set to factor of $\geq$1.5 (up- or downregulation). The data were further manually evaluated based on the average reporter ion count ($\geq$2 for medium confidence, $\geq$4 for high confidence). Furthermore, the average variability was observed as a function of the differential regulation and the reporter ion count. Label-free quantification was performed by the precursor ions area method of PD software (version 2.1). The mass tolerance was set to 2 ppm, and the signal-to-noise ratio had to be above 3. The abundance values were normalized based on the total peptide amount. The significance threshold for differential protein abundance was set to a factor of $\geq$2.0 (up- or downregulation).

Functional annotation of the EV proteome. The data set of differentially regulated proteins was filtered by the human serum proteome represented by Piper and Katzmann (64) and, in addition, by keratin, epidermal proteins, and complement component 5α, which were not considered for the proteome comparison. The filtering and the overlap analyses were performed in R using the packages provided by Bioconductor software (65). The GO-term enrichment analysis of the overlapping proteins of the TMT data sets was performed using the FungiFun2 tool (66). The results contain categories determined by Fisher's exact test and Benjamini-Hochberg-corrected *P* values below 0.05.

Analysis of heterologously expressed human azurocidin and cathepsin G. Protein preparation, LC-MS/MS analysis, and a database search for the identification of proteins were essentially performed as previously described (62), except for the following changes. The LC gradient elution was as follows: 0 min at 4% eluent B, 5 min at 5% eluent B, 30 min at 8% eluent B, 60 min at 12% eluent B, 100 min at 20% eluent B, 120 min at 25% eluent B, 140 min at 35% eluent B, 150 min at 45% eluent B, 160 min at 60% eluent B, 170 to 175 min at 96% eluent B, and 175.1 to 200 min at 4% eluent B. Mass spectrometry analysis was performed on a QExactive HF instrument (Thermo Fisher Scientific) at a resolution of 120,000 FWHM for MS1 scans and 15,000 FWHM for MS2 scans. Tandem mass spectra were searched against the UniProt database (7 August 2018; https://www.uniprot.org/proteomes/UP000002530) of *Neosartorya fumigata* (Af293) and the human protein sequences of azurocidin, cathepsin G, and RBP7, using Proteome Discoverer (PD) software (version 2.2; Thermo Fisher Scientific) and the algorithms of Sequest HT (a version of PD software [version 2.2]) and MS Amanda (version 2.0) software. Modifications were defined as dynamic Met oxidation and protein N-terminal acetylation as well as static Cys carbamidomethylation.

Determination of EV effects on fungi by CLSM. For determining the effects of EVs on fungi, EVs were dosed according to cell equivalents. One EV dose was defined as the number of EVs produced by 10^7 PMNs infected with *pksP* mutant conidia at an MOI of 5 at 2 h postinfection, which represented the maximal observed production of EVs (Fig. 1C) and which corresponded to approximately 10^9 EVs/ml by nanoparticle tracking analysis with a Malvern NS300 instrument (camera setting, 14; detection threshold, 4). At this time point, *pksP* conidia stimulated double the amount of EVs as wt conidia and 12-fold more than sEVs from the same number of cells. Consequently, the doses were adjusted to appropriately compare equal numbers of EVs. Freshly prepared and portioned EVs were coincubated with 30 μl of a suspension of 10^6 conidia/ml in HBSS in 12-well chambers (Ibidi GmbH). A confocal laser scanning microscopy (CLSM) system (Zeiss LSM 780; Carl Zeiss SAS) was employed; see "CLSM setup" below for details. Images were acquired once per hour from 10 different fields of view per well in a microtiter plate. The two-dimensional (2D) confocal images were recorded at a pixel size of 208 by 208 nm, whereas 3D image stacks had a voxel volume of 0.025 (19 samples) or 0.034 (15 samples) μm^3.

After 20 h, the samples were stained with annexin V-FITC (dilution, 1:60; BioLegend), PI (to a final concentration of 0.0167 μg/μl), and calcofluor white (to a final concentration of 0.167 μg/μl) in order to assess EV entry into hyphae and to collect image z-stacks by CLSM. When the GFP-expressing *A. fumigatus* strain AfS148 was used, the staining cocktail consisted of annexin V-Alexa Fluor 647 and calcofluor white, whereas PI staining was omitted in order to avoid spectral overlaps.

For investigation of EV-mediated fungal killing, we took advantage of a previously described mitochondrial GFP-expressing reporter strain, AfS35/pJW103 (49). When growing normally, this fungal strain shows a normal filamentous network of mitochondria, indicated by mitochondrion-specific fluorescence. For these experiments, 10^6 conidia/ml of strain AfS35/pJW103 were grown in HBSS in 8-well chambers (Ibidi GmbH) for 20 h prior to coincubation with freshly prepared EV fractions. Here, we used EVs collected from equal amounts of PMNs (10^7 PMNs). A CLSM system (Zeiss LSM 780; Carl Zeiss SAS) was used to monitor mitochondrial fragmentation (GFP signal) and cell growth (calcofluor white) over time. As a control, cell death was initiated using 3 mM H_2O_2, which causes the mitochondria to undergo fusion and form punctate structures within 1 h and then fade in fluorescence signal over time (49).

CLSM setup. The imaging data were collected with a Zeiss LSM 780 confocal laser scanning microscope (Carl Zeiss SAS). Images were taken using either a 10× (numerical aperture [NA], 0.4) or a 20× (NA, 0.7) objective lens in an inverted configuration, resulting in a total magnification of ×100 or ×200, respectively. In order to measure the point-spread function of the CLSM system, 5 μl of the blue, green, and deep-red calibration beads from a PS-Speck microscope point source kit (diameter, 170 nm; Invitrogen) was resuspended in the staining cocktail. The bead mixture was imaged under the same conditions applied for the z-stacks of the hypha-EV system. Individual 3D bead images were averaged per color by the use of the HuygensPro program, and the resulting 3D bead images were used to distill the measured point-spread function for all three colors. For the imaging of hyphae and EVs, the CLSM objective lens and stage were preheated to 37°C for 3 to 5 h prior to image scanning. Bright-field images were acquired from 10 different fields of view per well once per hour for 15 time points using a 20× (NA, 0.8) dry objective at 37°C in 5% (vol/vol) CO_2 atmosphere.

For the z-stacks, images were collected at an axial separation that was set according to the Nyquist criterion for the shortest wavelength, using the same z-step size for all channels. The axial range was adjusted to the thickness of the observed cells.

3D image analysis of EV internalization. For a quantitative analysis of the afEV-hypha interactions, the 3D shape of each object type was reconstructed based on four-dimensional (3D plus color) fluorescence images using the following procedure: the images were deconvolved using the HuygensPro program (Scientific Volume Imaging, Hilversum, The Netherlands) with a measured point spread function (PSF) (see "CLSM setup" above) that was recorded individually for each fluorescence channel. The deconvolved images were transferred to Imaris software (Bitplane, Zürich, Switzerland) for 3D reconstruction. The basic object types (hyphae, DNA, EVs) were reconstructed in Imaris software using manually adjusted templates. The reconstructed hyphae included objects only from the calcofluor white channel (see "Determination of EV effects on fungi by CLSM" above) that were larger than 20 μm^3 and that had no surface points on the sample border. The reconstruction process is presented in the first and second movies at https://doi.org/10.6084/m9.figshare.11973174. The control samples and those with GFP fluorescence were reconstructed using the same procedure. Hypha-associated DNA and hypha-associated EVs were identified by using a binary mask of the hyphae (channel 4; see the second movie at https://doi.org/10.6084/m9.figshare.11973174). Only those objects that were located either on the border or inside the hyphae, as identified by a threshold of the mean value of the calcofluor white fluorescence signal above 5×10^{-10}, were considered hypha associated. The binary mask of hypha-associated EVs was used to select hypha-associated DNA that interacted with EVs (hypha-associated DNA, mean value for the binary mask of hyphae; see the second movie at https://doi.org/10.6084/m9.figshare.11973174). Finally, the total volume of each object class at every field of view was computed. Additionally, the EV volume inside the hyphae was computed over the regions that were double positive for annexin V (EVs) and calcofluor white (hyphae), whereas the EV volume outside the hyphae was defined as the volume that was positive for annexin V but not calcofluor white. The EV densities inside and outside the hyphae were then defined as follows: EV density inside hyphae = (EV volume inside hyphae/hyphal volume) and EV density outside hyphae = [(EV volume outside hyphae)/(sample volume − hyphal volume)]. The sample volume was estimated based on the voxel size and the number of voxels in each sample (automatically performed by Imaris software).

Automated 2D image analysis of hyphal growth. For quantitative analysis of hyphal growth in bright-field microscopy images, the area of the regions of interest (ROI) corresponding to the conidia and the hyphae was computed automatically for each image. The image analysis algorithm was implemented in Matlab (Matlab 2017a; MathWorks). The code is available from the authors upon request. The procedure included (i) binarization of the image data, (ii) binary image enhancement, (iii) selection of the ROI based on morphological filtering, (iv) image postprocessing and filtering, and (v) measurement of the area of the ROI. Two of the original image sections, together with the resulting images after application of the aforementioned steps, are illustrated in Fig. S4A in the supplemental material. All parameters of the algorithm were adjusted to minimize the detection of noise and of out-of-focus objects, and the adjustment was confirmed by visual inspection of the images. The image data were saved in 16-bit CZI format and loaded into Matlab using the bfopen script from the Open Microscopy Environment (https://www.openmicroscopy.org/site/support/bio-formats5.3/developers/matlab-dev.html).

The images were processed in five steps. In step 1, binarization was performed using the function imbinarize from the Matlab ImageProcessing tool box with the following parameters: the adaptive

threshold type, a sensitivity factor for adaptive thresholding of 0.45, and a foreground darker than the background (ForegroundPolarity = dark). In step 2, enhancement of the binary image included the following steps: majority filter, which sets a pixel value to 1 if five or more pixels in its 3-by-3 neighborhood have values of 1 and to 0 otherwise; hole filling inside the ROI; and object removal for ROIs with an area of less than 200 pixels, which corresponds to the minimal area of resting conidia. The resulting image is referred to as image *S*. Step 3 was selection of the ROI, in which image *S* was split into two masks, masks *M* and *S′*, based on the object area, where image *M* contained all ROIs with an area of less than 1,000 pixels, which corresponded to resting, swollen, and germinated conidia, as well as parts of vesicle clumps, and image *S′*, which was all remaining large ROIs, which corresponded to hyphae; removal of all ROIs from mask *M* with a solidity value below 0.85, corresponding to vesicle clumps (the resulting mask is referred to as mask *M′*); and combination of masks *M′* and *S′* into one mask, mask *R*, by the logical sum operation of masks *M′* and *S′*. Step 4 was image postprocessing and filtering, consisting of the morphological closing of mask *R* with two line elements (10 pixels long; orientations, 45° and 135°) to connect broken contours and removal of all ROIs for which the 1st percentile of their Feret diameters was less than 17 pixels (the size of resting conidia). Removal of these ROIs removes the remaining vesicle clumps which have regions thinner than 17 pixels. For Feret diameter calculation, the tool box Feret diameter and oriented box was used (David Legland, https://www.mathworks.com/matlabcentral/fileexchange/30402-feret-diameter-and-oriented-box). Step 5 consisted of measurement of the area of the ROI, in which the area of each object was computed using the function regionprops with the parameter FilledArea and the median of the areas of all ROIs in an image was used to characterize fungal coverage in the image.

Generation of transgenic *A. fumigatus* strains. For expression of the human azurocidin gene (*AZU1*), the human cathepsin G gene (*CTSG*), and the human retinol binding protein 7 gene (*RBP7*) in *A. fumigatus*, a tetracycline-controlled transcriptional activation (tet^{ON}) system was used (67). The human azurocidin, cathepsin G, and retinol binding protein 7 cDNA sequences obtained from the NCBI database were codon optimized for *A. fumigatus* using the GENEius tool (https://www.eurofinsgenomics.eu/en/gene-synthesis-molecular-biology/geneius/) and synthesized together with the *tef* terminator (Eurofins Genomics). Each of the genes was PCR amplified from the corresponding synthetic template using the Phusion Flash high-fidelity PCR master mix (Thermo Fisher Scientific) with the primer pairs Azu_polictail_f and tef_r for azurocidin, cathG_polictail_f and tef_r for cathepsin G, and RBP7_polictail_F and tef_r for RBP7 (Table S2). The tet^{ON} promoter cassette was amplified from plasmid pSK562 with primers ptetOn_pYES2tail_F and pOliC_R, while the pyrithiamine resistance cassette (*ptrA*) was amplified from plasmid pSK275 with primers ptrA_teftail_F and ptrA_pYES2tail_R. Plasmid pYES2 was used as the backbone vector and amplified with primers pYES2_r and pYES2_f. The tet^{ON} cassette, each of the three human genes, and the *ptrA* cassette were assembled with the pYES2 backbone using the NEBuilder HiFi DNA assembly master mix (New England Biolabs) according to the manufacturer's instructions. The resulting 10-kb plasmids were sequenced and subsequently used to transform *A. fumigatus* ATCC 46645 as previously described (59). Transformants were selected with 0.1-μg/ml pyrithiamine.

Southern blot analysis to confirm genetic manipulation of the *A. fumigatus* strains was carried out as described before (68). For Northern blot analysis, 16-h-old precultures were treated with 10-μg/ml doxycycline. Mycelia were harvested at 3 h after the addition of doxycycline. RNA extraction and detection of RNA by Northern blotting were carried out as previously described (68).

Data availability. The mass spectrometry proteomics data have been deposited in the ProteomeXchange Consortium via the PRIDE partner repository with the data set identifier PXD005994 (69).

SUPPLEMENTAL MATERIAL

Supplemental material is available online only.

FIG S1, TIF file, 0.1 MB.
FIG S2, TIF file, 0.1 MB.
FIG S3, TIF file, 0.3 MB.
FIG S4, TIF file, 0.2 MB.
FIG S5, TIF file, 0.1 MB.
FIG S6, TIF file, 0.2 MB.
FIG S7, TIF file, 0.1 MB.
TABLE S1, PDF file, 0.1 MB.
TABLE S2, PDF file, 0.01 MB.

ACKNOWLEDGMENTS

We are thankful to all anonymous blood donors, to Ellen Ritter and Tobias Rachow (for blood draws), Frank Steiniger (for cryo-TEM imaging), and Sven Krappmann (for the AfS148 strain and the pSK562 plasmid). We kindly thank Johannes Wagener for providing the AfS103/pJW103 strain. We thank Silke Steinbach for excellent technical assistance. We thank Maria Straßburger and Thorsten Heinekamp for their contributions to the success of this project.

This work was supported by the Collaborative Research Center/Transregio 124

(Pathogenic fungi and their human host—networks of interaction—FungiNet), funded by the Deutsche Forschungsgemeinschaft (DFG; A1, B4, C6, Z2), to O.K., P.F.Z., M.T.F., and A.A.B.; the DFG-funded excellence graduate school Jena School for Microbial Communication (JSMC) to T.C., and Leibniz ScienceCampus InfectoOptics grant SAS-2015-HKI-LWC (Project BLOODi) to M.T.F.

The funders had no role in study design, data collection and analysis, the decision to publish, or preparation of the manuscript.

REFERENCES

1. Patterson TF, Thompson GR, III, Denning DW, Fishman JA, Hadley S, Herbrecht R, Kontoyiannis DP, Marr KA, Morrison VA, Nguyen MH, Segal BH, Steinbach WJ, Stevens DA, Walsh TJ, Wingard JR, Young JA, Bennett JE. 2016. Practice guidelines for the diagnosis and management of aspergillosis: 2016 update by the Infectious Diseases Society of America. Clin Infect Dis 63:e1–e60. https://doi.org/10.1093/cid/ciw326.
2. Maertens JA, Raad II, Marr KA, Patterson TF, Kontoyiannis DP, Cornely OA, Bow EJ, Rahav G, Neofytos D, Aoun M, Baddley JW, Giladi M, Heinz WJ, Herbrecht R, Hope W, Karthaus M, Lee D-G, Lortholary O, Morrison VA, Oren I, Selleslag D, Shoham S, Thompson GR, III, Lee M, Maher RM, Schmitt-Hoffmann A-H, Zeiher B, Ullmann AJ. 2016. Isavuconazole versus voriconazole for primary treatment of invasive mould disease caused by *Aspergillus* and other filamentous fungi (SECURE): a phase 3, randomised-controlled, non-inferiority trial. Lancet 387:760–769. https://doi.org/10.1016/S0140-6736(15)01159-9.
3. Marr KA, Schlamm HT, Herbrecht R, Rottinghaus ST, Bow EJ, Cornely OA, Heinz WJ, Jagannatha S, Koh LP, Kontoyiannis DP, Lee DG, Nucci M, Pappas PG, Slavin MA, Queiroz-Telles F, Selleslag D, Walsh TJ, Wingard JR, Maertens JA. 2015. Combination antifungal therapy for invasive aspergillosis: a randomized trial. Ann Intern Med 162:81–89. https://doi.org/10.7326/M13-2508.
4. Kosmidis C, Denning DW. 2015. The clinical spectrum of pulmonary aspergillosis. Thorax 70:270–277. https://doi.org/10.1136/thoraxjnl-2014-206291.
5. Dagenais TR, Keller NP. 2009. Pathogenesis of *Aspergillus fumigatus* in invasive aspergillosis. Clin Microbiol Rev 22:447–465. https://doi.org/10.1128/CMR.00055-08.
6. Osherov N, Kontoyiannis DP. 2017. The anti-Aspergillus drug pipeline: is the glass half full or empty? Med Mycol 55:118–124. https://doi.org/10.1093/mmy/myw060.
7. Kalleda N, Amich J, Arslan B, Poreddy S, Mattenheimer K, Mokhtari Z, Einsele H, Brock M, Heinze KG, Beilhack A. 2016. Dynamic immune cell recruitment after murine pulmonary *Aspergillus fumigatus* infection under different immunosuppressive regimens. Front Microbiol 7:1107. https://doi.org/10.3389/fmicb.2016.01107.
8. Bonnett CR, Cornish EJ, Harmsen AG, Burritt JB. 2006. Early neutrophil recruitment and aggregation in the murine lung inhibit germination of *Aspergillus fumigatus* conidia. Infect Immun 74:6528–6539. https://doi.org/10.1128/IAI.00909-06.
9. Mircescu MM, Lipuma L, van Rooijen N, Pamer EG, Hohl TM. 2009. Essential role for neutrophils but not alveolar macrophages at early time points following *Aspergillus fumigatus* infection. J Infect Dis 200:647–656. https://doi.org/10.1086/600380.
10. Dragonetti G, Criscuolo M, Fianchi L, Pagano L. 2017. Invasive aspergillosis in acute myeloid leukemia: are we making progress in reducing mortality? Med Mycol 55:82–86. https://doi.org/10.1093/mmy/myw114.
11. Bianchi M, Niemiec MJ, Siler U, Urban CF, Reichenbach J. 2011. Restoration of anti-*Aspergillus* defense by neutrophil extracellular traps in human chronic granulomatous disease after gene therapy is calprotectin-dependent. J Allergy Clin Immunol 127:1243–1252.e7. https://doi.org/10.1016/j.jaci.2011.01.021.
12. Matute JD, Arias AA, Wright NA, Wrobel I, Waterhouse CC, Li XJ, Marchal CC, Stull ND, Lewis DB, Steele M, Kellner JD, Yu W, Meroueh SO, Nauseef WM, Dinauer MC. 2009. A new genetic subgroup of chronic granulomatous disease with autosomal recessive mutations in p40 phox and selective defects in neutrophil NADPH oxidase activity. Blood 114:3309–3315. https://doi.org/10.1182/blood-2009-07-231498.
13. Alflen A, Prufer S, Ebner K, Reuter S, Aranda Lopez P, Scharrer I, Banno F, Stassen M, Schild H, Jurk K, Bosmann M, Beckert H, Radsak MP. 2017. ADAMTS-13 regulates neutrophil recruitment in a mouse model of invasive pulmonary aspergillosis. Sci Rep 7:7184. https://doi.org/10.1038/s41598-017-07340-3.
14. Shlezinger N, Irmer H, Dhingra S, Beattie SR, Cramer RA, Braus GH, Sharon A, Hohl TM. 2017. Sterilizing immunity in the lung relies on targeting fungal apoptosis-like programmed cell death. Science 357:1037–1041. https://doi.org/10.1126/science.aan0365.
15. Espinosa V, Dutta O, McElrath C, Du P, Chang YJ, Cicciarelli B, Pitler A, Whitehead I, Obar JJ, Durbin JE, Kotenko SV, Rivera A. 2017. Type III interferon is a critical regulator of innate antifungal immunity. Sci Immunol 2:eaan5357. https://doi.org/10.1126/sciimmunol.aan5357.
16. Bianchi M, Hakkim A, Brinkmann V, Siler U, Seger RA, Zychlinsky A, Reichenbach J. 2009. Restoration of NET formation by gene therapy in CGD controls aspergillosis. Blood 114:2619–2622. https://doi.org/10.1182/blood-2009-05-221606.
17. Boyle KB, Gyori D, Sindrilaru A, Scharffetter-Kochanek K, Taylor PR, Mocsai A, Stephens LR, Hawkins PT. 2011. Class IA phosphoinositide 3-kinase beta and delta regulate neutrophil oxidase activation in response to *Aspergillus fumigatus* hyphae. J Immunol 186:2978–2989. https://doi.org/10.4049/jimmunol.1002268.
18. Boyle KB, Stephens LR, Hawkins PT. 2012. Activation of the neutrophil NADPH oxidase by *Aspergillus fumigatus*. Ann N Y Acad Sci 1273:68–73. https://doi.org/10.1111/j.1749-6632.2012.06821.x.
19. Levitz SM, Farrell TP. 1990. Human neutrophil degranulation stimulated by *Aspergillus fumigatus*. J Leukoc Biol 47:170–175. https://doi.org/10.1002/jlb.47.2.170.
20. Zarember KA, Sugui JA, Chang YC, Kwon-Chung KJ, Gallin JI. 2007. Human polymorphonuclear leukocytes inhibit *Aspergillus fumigatus* conidial growth by lactoferrin-mediated iron depletion. J Immunol 178:6367–6373. https://doi.org/10.4049/jimmunol.178.10.6367.
21. Braem SG, Rooijakkers SH, van Kessel KP, de Cock H, Wosten HA, van Strijp JA, Haas PJ. 2015. Effective neutrophil phagocytosis of *Aspergillus fumigatus* is mediated by classical pathway complement activation. J Innate Immun 7:364–374. https://doi.org/10.1159/000369493.
22. Bruns S, Kniemeyer O, Hasenberg M, Aimanianda V, Nietzsche S, Thywissen A, Jeron A, Latge JP, Brakhage AA, Gunzer M. 2010. Production of extracellular traps against *Aspergillus fumigatus in vitro* and in infected lung tissue is dependent on invading neutrophils and influenced by hydrophobin RodA. PLoS Pathog 6:e1000873. https://doi.org/10.1371/journal.ppat.1000873.
23. McCormick A, Heesemann L, Wagener J, Marcos V, Hartl D, Loeffler J, Heesemann J, Ebel F. 2010. NETs formed by human neutrophils inhibit growth of the pathogenic mold *Aspergillus fumigatus*. Microbes Infect 12:928–936. https://doi.org/10.1016/j.micinf.2010.06.009.
24. Eken C, Gasser O, Zenhaeusern G, Oehri I, Hess C, Schifferli JA. 2008. Polymorphonuclear neutrophil-derived ectosomes interfere with the maturation of monocyte-derived dendritic cells. J Immunol 180:817–824. https://doi.org/10.4049/jimmunol.180.2.817.
25. Eken C, Sadallah S, Martin PJ, Treves S, Schifferli JA. 2013. Ectosomes of polymorphonuclear neutrophils activate multiple signaling pathways in macrophages. Immunobiology 218:382–392. https://doi.org/10.1016/j.imbio.2012.05.021.
26. Gasser O, Hess C, Miot S, Deon C, Sanchez JC, Schifferli JA. 2003. Characterisation and properties of ectosomes released by human polymorphonuclear neutrophils. Exp Cell Res 285:243–257. https://doi.org/10.1016/s0014-4827(03)00055-7.
27. Pliyev BK, Kalintseva MV, Abdulaeva SV, Yarygin KN, Savchenko VG. 2014. Neutrophil microparticles modulate cytokine production by natural killer cells. Cytokine 65:126–129. https://doi.org/10.1016/j.cyto.2013.11.010.
28. Majumdar R, Tavakoli Tameh A, Parent CA. 2016. Exosomes mediate LTB4 release during neutrophil chemotaxis. PLoS Biol 14:e1002336. https://doi.org/10.1371/journal.pbio.1002336.

29. HeadlandSE, Jones HR, Norling LV, Kim A, Souza PR, Corsiero E, Gil CD, Nerviani A, Dell'Accio F, Pitzalis C, Oliani SM, Jan LY, Perretti M. 2015. Neutrophil-derived microvesicles enter cartilage and protect the joint in inflammatory arthritis. Sci Transl Med 7:315ra190. https://doi.org/10.1126/scitranslmed.aac5608.
30. GasserO, Schifferli JA. 2005. Microparticles released by human neutrophils adhere to erythrocytes in the presence of complement. Exp Cell Res 307:381–387. https://doi.org/10.1016/j.yexcr.2005.03.011.
31. NieuwlandR, Berckmans RJ, McGregor S, Boing AN, Romijn FP, Westendorp RG, Hack CE, Sturk A. 2000. Cellular origin and procoagulant properties of microparticles in meningococcal sepsis. Blood 95:930–935. https://doi.org/10.1182/blood.V95.3.930.003k46_930_935.
32. WatanabeJ, Marathe GK, Neilsen PO, Weyrich AS, Harrison KA, Murphy RC, Zimmerman GA, McIntyre TM. 2003. Endotoxins stimulate neutrophil adhesion followed by synthesis and release of platelet-activating factor in microparticles. J Biol Chem 278:33161–33168. https://doi.org/10.1074/jbc.M305321200.
33. RossaintJ, Kuhne K, Skupski J, Van Aken H, Looney MR, Hidalgo A, Zarbock A. 2016. Directed transport of neutrophil-derived extracellular vesicles enables platelet-mediated innate immune response. Nat Commun 7:13464. https://doi.org/10.1038/ncomms13464.
34. TimarCI, Lorincz AM, Csepanyi-Komi R, Valyi-Nagy A, Nagy G, Buzas EI, Ivanyi Z, Kittel A, Powell DW, McLeish KR, Ligeti E. 2013. Antibacterial effect of microvesicles released from human neutrophilic granulocytes. Blood 121:510–518. https://doi.org/10.1182/blood-2012-05-431114.
35. HessC, Sadallah S, Hefti A, Landmann R, Schifferli JA. 1999. Ectosomes released by human neutrophils are specialized functional units. J Immunol 163:4564–4573.
36. Lim K, Hyun Y-M, Lambert-Emo K, Capece T, Bae S, Miller R, Topham DJ, Kim M. 2015. Neutrophil trails guide influenza-specific CD8^{+} T cells in the airways. Science 349:aaa4352. https://doi.org/10.1126/science.aaa4352.
37. HerrmannIK, Bertazzo S, O'Callaghan DJP, Schlegel AA, Kallepitis C, Antcliffe DB, Gordon AC, Stevens MM. 2015. Differentiating sepsis from noninfectious systemic inflammation based on microvesicle-bacteria aggregation. Nanoscale 7:13511–13520. https://doi.org/10.1039/c5nr01851j.
38. BehnsenJ, Narang P, Hasenberg M, Gunzer F, Bilitewski U, Klippel N, Rohde M, Brock M, Brakhage AA, Gunzer M. 2007. Environmental dimensionality controls the interaction of phagocytes with the pathogenic fungi *Aspergillus fumigatus* and *Candida albicans*. PLoS Pathog 3:e13. https://doi.org/10.1371/journal.ppat.0030013.
39. Lo˝rincz ÁM, Bartos B, Szombath D, Szeifert V, Timár CI, Turiák L, Drahos L, Kittel Á, Veres DS, Kolonics F, Mócsai A, Ligeti E. 2020. Role of Mac-1 integrin in generation of extracellular vesicles with antibacterial capacity from neutrophilic granulocytes. J Extracell Vesicles 9:1698889. https://doi.org/10.1080/20013078.2019.1698889.
40. JahnB, Boukhallouk F, Lotz J, Langfelder K, Wanner G, Brakhage AA. 2000. Interaction of human phagocytes with pigmentless *Aspergillus* conidia. Infect Immun 68:3736–3739. https://doi.org/10.1128/iai.68.6.3736-3739.2000.
41. JahnB, Langfelder K, Schneider U, Schindel C, Brakhage AA. 2002. PKSP-dependent reduction of phagolysosome fusion and intracellular kill of *Aspergillus fumigatus* conidia by human monocyte-derived macrophages. Cell Microbiol 4:793–803. https://doi.org/10.1046/j.1462-5822 .2002.00228.x.
42. TsaiHF, Chang YC, Washburn RG, Wheeler MH, Kwon-Chung KJ. 1998. The developmentally regulated *alb1* gene of *Aspergillus fumigatus*: its role in modulation of conidial morphology and virulence. J Bacteriol 180:3031–3038. https://doi.org/10.1128/JB.180.12.3031-3038.1998.
43. BlangoMG, Kniemeyer O, Brakhage AA. 2019. Conidial surface proteins at the interface of fungal infections. PLoS Pathog 15:e1007939. https://doi.org/10.1371/journal.ppat.1007939.
44. HeinekampT, Thywißen A, Macheleidt J, Keller S, Valiante V, Brakhage AA. 2012. *Aspergillus fumigatus* melanins: interference with the host endocytosis pathway and impact on virulence. Front Microbiol 3:440. https://doi.org/10.3389/fmicb.2012.00440.
45. Yáñez-MóM, Siljander PR-M, Andreu Z, Zavec AB, Borràs FE, Buzas EI, Buzas K, Casal E, Cappello F, Carvalho J, Colás E, Cordeiro-da Silva A, Fais S, Falcon-Perez JM, Ghobrial IM, Giebel B, Gimona M, Graner M, Gursel I, Gursel M, Heegaard NHH, Hendrix A, Kierulf P, Kokubun K, Kosanovic M, Kralj-Iglic V, Krämer-Albers E-M, Laitinen S, Lässer C, Lener T, Ligeti E, Line¯ A, Lipps G, Llorente A, Lötvall J, Manc˘ek-Keber M, Marcilla A, Mittelbrunn M, Nazarenko I, Nolte-'t Hoen ENM, Nyman TA, O'Driscoll L, Olivan M, Oliveira C, Pállinger É, Del Portillo HA, Reventós J, Rigau M, Rohde E, Sammar M, et al. 2015. Biological properties of extracellular vesicles and their physiological functions. J Extracell Vesicles 4:27066. https://doi.org/10.3402/jev.v4.27066.
46. KroghA, Larsson B, von Heijne G, Sonnhammer EL. 2001. Predicting transmembrane protein topology with a hidden Markov model: application to complete genomes. J Mol Biol 305:567–580. https://doi.org/10.1006/jmbi.2000.4315.
47. PetersenTN, Brunak S, von Heijne G, Nielsen H. 2011. SignalP 4.0: discriminating signal peptides from transmembrane regions. Nat Methods 8:785–786. https://doi.org/10.1038/nmeth.1701.
48. Horton P, Park KJ, Obayashi T, Fujita N, Harada H, Adams-Collier CJ, Nakai K. 2007. WoLF PSORT: protein localization predictor. Nucleic Acids Res 35:W585–W587. https://doi.org/10.1093/nar/gkm259.
49. RufD, Brantl V, Wagener J. 2018. Mitochondrial fragmentation in *Aspergillus fumigatus* as early marker of granulocyte killing activity. Front Cell Infect Microbiol 8:128. https://doi.org/10.3389/fcimb.2018.00128.
50. TkalcevicJ, Novelli M, Phylactides M, Iredale JP, Segal AW, Roes J. 2000. Impaired immunity and enhanced resistance to endotoxin in the absence of neutrophil elastase and cathepsin G. Immunity 12:201–210. https://doi.org/10.1016/s1074-7613(00)80173-9.
51. NewmanSL, Gootee L, Gabay JE, Selsted ME. 2000. Identification of constituents of human neutrophil azurophil granules that mediate fungistasis against *Histoplasma capsulatum*. Infect Immun 68:5668–5672. https://doi.org/10.1128/iai.68.10.5668-5672.2000.
52. GazendamRP, van de Geer A, Roos D, van den Berg TK, Kuijpers TW. 2016. How neutrophils kill fungi. Immunol Rev 273:299–311. https://doi.org/10.1111/imr.12454.
53. LangfelderK, Jahn B, Gehringer H, Schmidt A, Wanner G, Brakhage AA. 1998. Identification of a polyketide synthase gene (*pksP*)of *Aspergillus fumigatus* involved in conidial pigment biosynthesis and virulence. Med Microbiol Immunol 187:79–89. https://doi.org/10.1007/s004300050077.
54. JahnB, Koch A, Schmidt A, Wanner G, Gehringer H, Bhakdi S, Brakhage AA. 1997. Isolation and characterization of a pigmentless-conidium mutant of *Aspergillus fumigatus* with altered conidial surface and reduced virulence. Infect Immun 65:5110–5117. https://doi.org/10.1128/IAI.65.12.5110-5117.1997.
55. LangfelderK, Philippe B, Jahn B, Latge JP, Brakhage AA. 2001. Differential expression of the *Aspergillus fumigatus pksP* gene detected *in vitro* and *in vivo* with green fluorescent protein. Infect Immun 69:6411–6418. https://doi.org/10.1128/IAI.69.10.6411-6418.2001.
56. EllettF, Jorgensen J, Frydman GH, Jones CN, Irimia D. 2017. Neutrophil interactions stimulate evasive hyphal branching by *Aspergillus fumigatus*. PLoS Pathog 13:e1006154. https://doi.org/10.1371/journal.ppat.1006154.
57. GenschmerKR, Russell DW, Lal C, Szul T, Bratcher PE, Noerager BD, Abdul Roda M, Xu X, Rezonzew G, Viera L, Dobosh BS, Margaroli C, Abdalla TH, King RW, McNicholas CM, Wells JM, Dransfield MT, Tirouvanziam R, Gaggar A, Blalock JE. 2019. Activated PMN exosomes: pathogenic entities causing matrix destruction and disease in the lung. Cell 176: 113–126.e15. https://doi.org/10.1016/j.cell.2018.12.002.
58. LotherJ, Breitschopf T, Krappmann S, Morton CO, Bouzani M, Kurzai O, Gunzer M, Hasenberg M, Einsele H, Loeffler J. 2014. Human dendritic cell subsets display distinct interactions with the pathogenic mould *Aspergillus fumigatus*. Int J Med Microbiol 304:1160–1168. https://doi.org/10 .1016/j.ijmm.2014.08.009.
59. WeidnerG, d'Enfert C, Koch A, Mol PC, Brakhage AA. 1998. Development of a homologous transformation system for the human pathogenic fungus *Aspergillus fumigatus* based on the *pyrG* gene encoding orotidine 5′-monophosphate decarboxylase. Curr Genet 33:378–385. https://doi.org/10.1007/s002940050350.
60. Lőrincz ÁM, Timár CI, Marosvári KA, Veres DS, Otrokocsi L, Kittel Á, Ligeti E. 2014. Effect of storage on physical and functional properties of extracellular vesicles derived from neutrophilic granulocytes. J Extracell Vesicles 3:25465. https://doi.org/10.3402/jev.v3.25465.
61. WesselD, Flügge UI. 1984. A method for the quantitative recovery of protein in dilute solution in the presence of detergents and lipids. Anal Biochem 138:141–143. https://doi.org/10.1016/0003-2697(84)90782-6.
62. BaldinC, Valiante V, Kruger T, Schafferer L, Haas H, Kniemeyer O, Brakhage AA. 2015. Comparative proteomics of a *tor* inducible *Aspergillus fumigatus* mutant reveals involvement of the Tor kinase in iron regulation. Proteomics 15:2230–2243. https://doi.org/10.1002/pmic.201400584.
63. DorferV, Pichler P, Stranzl T, Stadlmann J, Taus T, Winkler S, Mechtler K. 2014. MS Amanda, a universal identification algorithm optimized for high accuracy tandem mass spectra. J Proteome Res 13:3679–3684. https://doi.org/10.1021/pr500202e.
64. Piper RC, Katzmann DJ. 2007. Biogenesis and function of multivesicular

bodies. Annu Rev Cell Dev Biol 23:519–547. https://doi.org/10.1146/annurev.cellbio.23.090506.123319.
65. Ihaka R, Gentleman R. 1996. R: a language for data analysis and graphics. J Comput Graph Stat 5:299–314. https://doi.org/10.2307/1390807.
66. PriebeS, Kreisel C, Horn F, Guthke R, Linde J. 2015. FungiFun2: a comprehensive online resource for systematic analysis of gene lists from fungal species. Bioinformatics 31:445– 446. https://doi.org/10 .1093/bioinformatics/btu627.
67. HelmschrottC, Sasse A, Samantaray S, Krappmann S, Wagener J. 2013. Upgrading fungal gene expression on demand: improved systems for doxycycline-dependent silencing in *Aspergillus fumigatus*. Appl Environ Microbiol 79:1751–1754. https://doi.org/10.1128/AEM.03626-12.
68. UnklesSE, Valiante V, Mattern DJ, Brakhage AA. 2014. Synthetic biology tools for bioprospecting of natural products in eukaryotes. Chem Biol 21:502–508. https://doi.org/10.1016/j.chembiol.2014.02.010.
69. Vizcaino JA, Csordas A, del-Toro N, Dianes JA, Griss J, Lavidas I, Mayer G, Perez-Riverol Y, Reisinger F, Ternent T, Xu QW, Wang R, Hermjakob H. 2016. 2016 update of the PRIDE database and its related tools. Nucleic Acids Res 44:D447–D456. https://doi.org/10.1093/nar/gkv 1145.

4 Discussion

Host-pathogen interactions are among most complex biological processes. The study of these processes is essential for our understanding of infectious disease, as well as their diagnostics, treatment, and prevention. To uncover spatiotemporal aspects of those interactions, different microscopy techniques are used followed by quantitative image analysis. The dynamic growth number of automated image analysis tools specifically developed for these tasks and data reflects the importance and high demand for such information. While some analyses, *e.g.* cell count or cell lineage trajectory detection, have become routine and could be done using dedicated proprietary or open-source software, others require *de novo* design of workflow algorithm.

The current work is devoted to the development of new workflow algorithms and software for quantitative analysis of effects occurring in the interaction of several most common pathogenic fungi (see Chapter 1.1) with the human innate immune system (see Chapter 1.2) and consists of two parts described in three publications.

4.1 *C. albicans* and *C. glabrata* alter neutrophil morphodynamics differently

The first part is focused on numerical analysis of changes in neutrophils morphodynamics after interaction with *C. albicans* or *C. glabrata* and their metabolites in whole blood infection assay using time-lapse microscopy data with the aim to contribute to an understanding of the interaction of those pathogens with components of the human innate immune system, neutrophils in particular. In preliminary exper-iments, it was observed that (i) neutrophils from infected samples tend to exhibit spreading morphology more often than those from mock-infected samples and (ii) neutrophils from *C. glabrata* infected samples tend to stay longer in the spreading form than those from *C. albicans* infected ones, *i.e.* neutrophils demonstrate different morphodynamics in different infection scenario. To perform quantitative measure-ments of those effects, a new workflow algorithm was designed.

4.1.1 Neutrophil segmentation and tracking

At the first step, each neutrophil within FoV must be accurately segmented and tracked. For these purposes, new methods were developed and implemented

differently the previously developed Algorithm for Migration and Interaction Tracking (AMIT) (Brandes *et al.,* 2015, 2017; Al-Zaben *et al.,* 2019). The full description of this new implementation can be found in my first-author publication ((Belyaev *et al.,* 2021), pp 27–39 in this dissertation). The distinct feature of this method is the accurate seg-mentation and tracking of cells with non-rigid shape in a population with a continuous spectrum of transition phases between spreading and non-spreading morphological appearances. These improvements were achieved, among other things, by the imple-mentation of a fusion-and-fission cluster detection approach, which does not rely on geometrical features of a single cell (*e.g.* footprint area) and, therefore, prevents frag-mentation of individual spreading cells, which can be as large as two or three non-spreading cells in close proximity.

Further tracking improvement is possible by implementing a machine learning algorithm that would distinguish cell clusters composed of cells in close proximity (CP-clusters) from those consisting of a cell on top of a cell (CT-clusters). This would pave the way to process those clusters by different algorithms. While CP-clusters should be processed as previously implemented in AMIT (or alternatively, as shown in Fig 4.1), CT-clusters might be processed differently: ether by tracking them independently without splitting or by implementing additional cluster split-ting algorithm which may reconstruct contours of cells within such a cluster. However, I think that such an oper-ation is possible to perform correctly for two-cell CT-clusters in high contrast DIC images only.

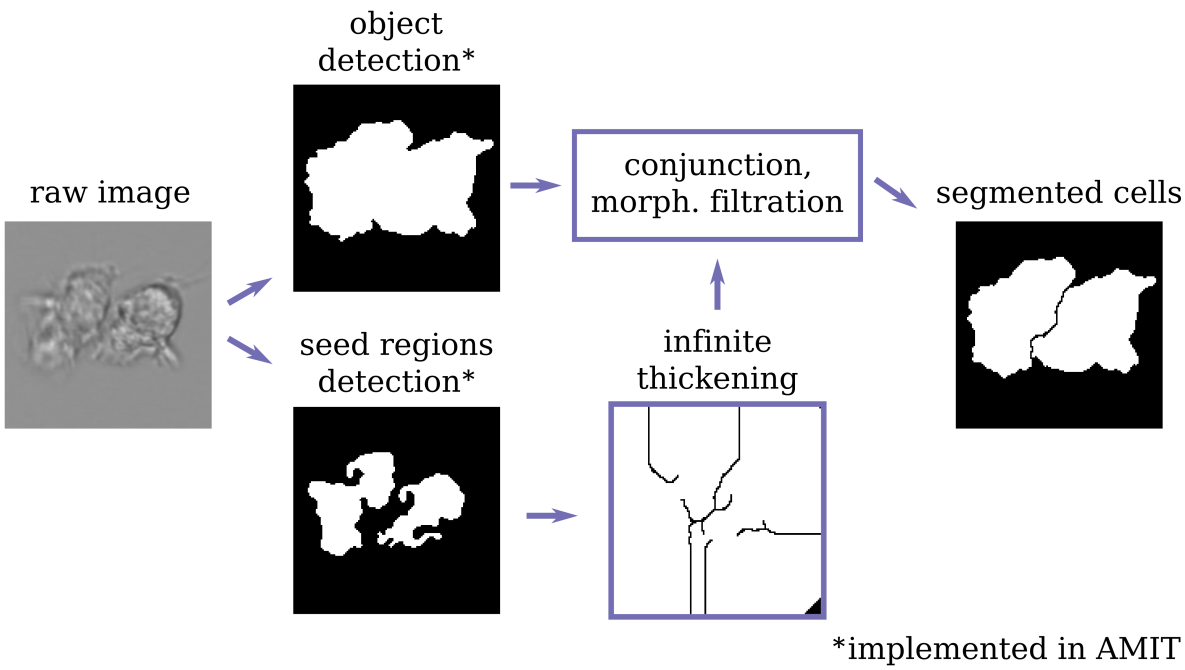

Fig. 4.1. An alternative approach for cluster splitting implemented using the *Matlab Image processing toolbox* in an earlier prototype of the segmentation algorithm (unpublished).

4.1.2 Analysis of neutrophil morphodynamics

The neutrophil morphodynamics was described using the morphology-focused feature extraction paradigm (see Chapter 1.5). To identify the morphological state of neutrophils in each time point, the one class classifier DD SIMCA (Pomerantsev 2008; Pomerantsev and Rodionova, 2014) was used. This method allowed to build the model of non-spreading neutrophils using unlabelled data from mock-infected samples, despite the fact that neutrophils in this infection scenario may rarely exhibit spreading morphology as well (see pp. 41–52 in this dissertation). With this approach, we quantita-tively confirmed and described the observed difference in neutrophil morphodynamics after *in vitro* whole blood infection assay ether with *C. albicans* or *C. glabrata* .

In addition, we demonstrated a way to use this measurable difference to distinguish between neutrophil populations affected by the two *Candida* species. However, considering the characteristics of the feature distributions, *i.e.* spreading cell fractions per frame and morphodynamical characteristics, it would be reasonable to refer to them as Bayesian biomarkers. Rather than providing a binary diagnostic outcome, these features indicate the probability of the specific pathogen presence. Going fur-ther, we speculated that morphodynamics could be used as an additional biomarker for rapid diagnostic/monitoring purposes, especially when the concentration of an analyte (fungal cells, their nucleic acids or metabolites) in patients' blood is below the bottom sensitivity limits of existing diagnostical tests. For example, T2Candida — the FDA and CE approved test for *Candida* species detection in blood — requires the presence of at least 1 CFU/mL (Mylonakis *et al.,* 2015; Clancy *et al.,* 2018; Clancy and Nguyen 2019). However, it was estimated that up to 50% of patients with candidemia have concentrations below this limit at the early stage of disease (Pfeiffer *et al.,* 2011), which reduces the chance for pathogen detection and identification. In such cases, neutrophils can be considered as primary sensors, and their morphodynamics may be regarded as a proxy signal, which can be detected with a higher probability. Yet, this approach must be evaluated in experiments with blood of patients with con-firmed candidemia, because, in my opinion, the applied whole blood infection (WBI) assay (Hünniger *et al.,* 2014) is merely replicating the acute reaction of the healthy immune system to a massive

invasion of pathogens (concentration of fungal cells is ~10^5 times higher than clinically observed values) and unable to replicate changes in neu-trophil population structure and biochemical background occurring in the course of the real disease (Yamashiro *et al.,* 2001; Pillay *et al.,* 2010; Leliefeld *et al.,* 2015; Silvestre-Roig *et al.,* 2016; Hong 2017; Tak *et al.,* 2017; Fraser *et al.,* 2018; Yang *et al.,* 2019). In fact, that WBI assay was designed to guarantee an acquisition of reliable statistics of phagocytosis events using flow cytometry. An alternative and more realistic model would be an multiorgan-on-chip assembly[8] (Picollet-D'hahan *et al.,* 2021; Ingber 2022), which must include at least blood circulatory system, hematopoietic organoid, liver, kidney and elements of central as well as peripheral nervous system which are also involved in the immune response (Felten *et al.,* 1987; Kenney and Ganta 2014; Godinho-Silva *et al.,* 2019). Ideally, all components of a single assembly must be raised from cells of a single immuno-competent donor using pluripotent (or induced pluripotent in case of an adult donor) stem cell technology (Kim *et al.,* 2020).

In addition, some other questions remain open. The first one is related to a possible difference in external morphology of spreading neutrophils in different infection scenarios (*e.g.* dynamics of protrusions formation (Hind *et al.,* 2016) and neutrophil trails production (Hong 2018)), which could be answered with an improved imaging technique, *e.g.* using de Sénarmont or Brace–Koehler compensators (Murphy and Davidson, 2012b), which offer the introduction of bias retardation much more precisely than it is possible with the used system that relies on the translation of the objective Nomarski prism across the optical pathway. In addition to an improved rendering of fine morphological structures in resulting images, this method can be easily standardised, which would lead to the high reproducibility of results in other laboratories. The second question is related to the stability of these characteristics within the same pop-ulation, i.e. would we observe the same statistics in different parts of the same sample. Based on that result, it would be possible to estimate a minimal blood volume for such an analysis. However, this analysis would require a new microscopy design which would allow simultaneous imaging of several FoV with high spatial and temporal resolutions with sufficiently high magnification to grasp details of neutrophil external morphology. And finally, a molecular mechanism responsible for differences in their morpho-dynamics is as of yet unknown, even at the hypothesis level.

[8] syn. 'patient-on-chip' platform or 'body-on-chips' multi-organ systems

4.2 Human neutrophils produce antifungal extracellular vesicles against *A. fumigatus*

The second part of this thesis is covered by the publication (Shopova *et al.,* 2020, pp. 54–72 in this dissertation) where we reveal that the clinically important human-pathogenic fungus *A. fumigatus* triggers neutrophil to release a distinct set of antifungal EVs (afEVs). With multiple techniques, we demonstrated that afEVs could suppress the growth of hyphae or damage developed ones. The quantitative analysis of some effects was done using AIA. While a growth kinetics analysis based on 2D transmitted light time-lapse microscopy data could be performed in a fully automated manner, the reconstruction of 3D structures of hyphae and afEVs based on 4D micros-copy data (3 spatial coordinates plus colour) was operator-aided due to variation in fluorescent intensity of hyphae between experimental runs. It is likely due to the fact that during staining, we rely on diffusion of colourants rather than intensive mechanical mixing to prevent the destruction of floating afEVs and hyphae layer in liquid media as it is depicted in the Fig. 4.2.

Lately, it occurs that propidium iodide positive (PI^+) signal is associated not exclusively with DNA. In literature and manufacturer's guideline (Suzuki *et al.,* 1997; invitrogen 2006), it is indicated that PI binds to the nucleotide pair of guanine and cytosine, therefore stains not only the DNAs but also the RNAs, necessitating treat-ment with nucleases to distinguish between RNA and DNA staining. Consequently, most PI+ entities in our samples represent cytoplasm

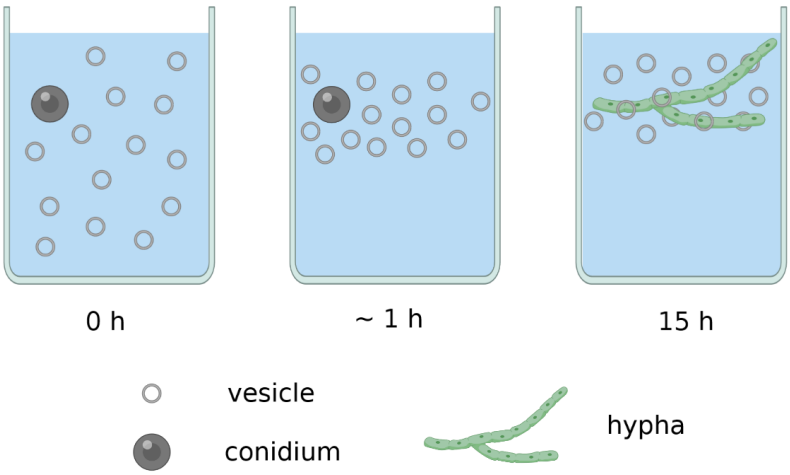

Fig. 4.2. The schematic illustration of a state of a colloidal suspension of hyphae and EVs in the Hanks' Balanced Salt Solution (HBSS) at 0 h, after ~ 1 h and 15 h of co-incubation. Created with BioRender.com.

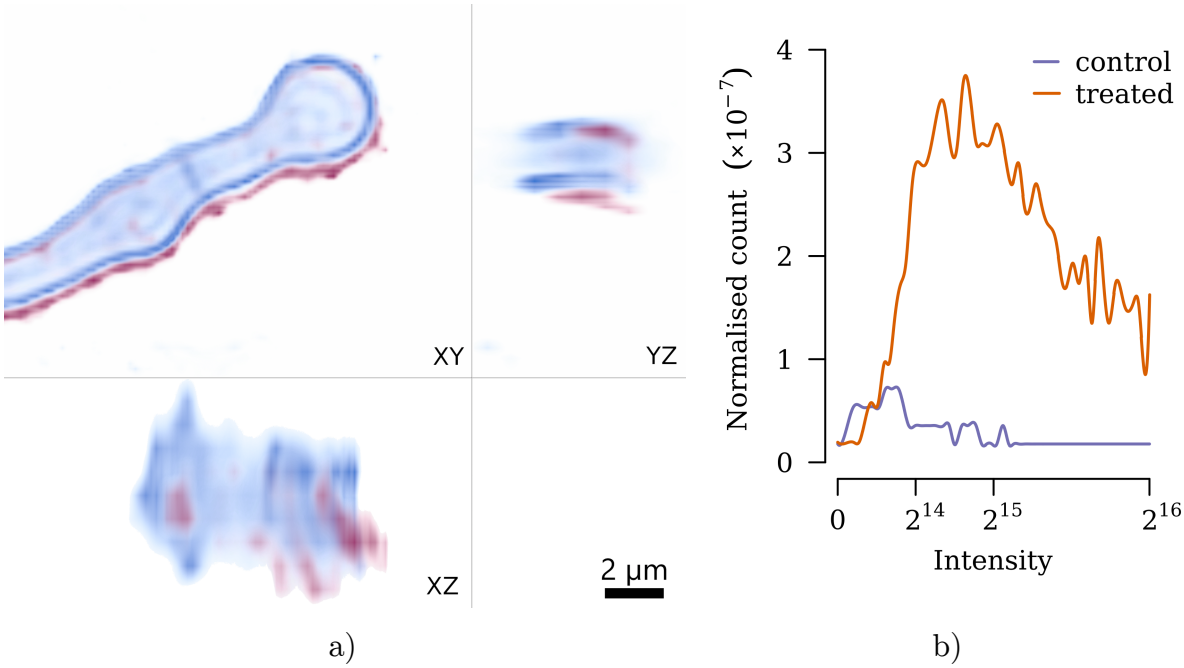

Fig. 4.3. Characterisation of PI^+ signal. a) localisation of PI probe around a hypha in a sample treated with afEVs. Blue colour corresponds to the calcofluor-white-positive signal, which marks polysaccharides in the fungal cell wall, red to the PI^+ signal, indicating nucleic acids' presence. For illustration purposes, intensities were inverted: darker colour — higher intensity. b) envelopes of voxels' intensity normalised histograms for hyphae-associated PI^+ signal, extracted using reconstructed 3D volumes, in a single control and treated samples. For details of the reconstruction, see the p. 68.

with dissolved RNA located in and around damaged hyphae (see Fig. 4.3 a). Also, such an interpretation aligns with the ratio between the amount of DNA and the cytoplasm. In addition, it seems that all PI^+ entities in the control samples and most of the entities in the treated samples have non-specific PI bonding, because for the specific bonding the intensity of fluores-cence is 20–30 fold higher (invitrogen, 2006). Some qualitative comparisons are pre-sented in Fig. 4.3 b. However, for a proper quantitative comparison, the fluorescence detector and image processing pipeline have to be calibrated using reference standards (Resch-Genger and DeRose, 2010; Kedziora *et al.,* 2011). Nevertheless, these misinter-pretations and overlooked occurrences do not obscure that afEVs cause hyphal damage. However, the results in the respective publication were acquired in an artificial environment: we observed a delay of development and degradation of hyphae in a concentrated emulsion of afEVs produced by neutrophils isolated from healthy donors' blood. In future experiments, it would be interesting to see real-time neutrophils action against developing hyphae using organ-on-chip models (*e.g.* (Hoang *et al.,* 2022)) and lattice light-sheet microscopy aided by artificial intelligence, which would allow to detect neutrophil aggregation around hyphae and capture these events in greater details.

5 Summary

The rising number of invasive fungal infections increases the burden in the health care systems worldwide. Proper diagnostics, curing and prevention necessitate a deep understanding of the interaction of pathogenic fungi with the human organism. An infectious process unfolds in time and on different spatial scales — tissue, cellular and molecular. Microscopy imaging followed by automated image analysis has become an irreplaceable tool for discovering spatiotemporal aspects of this complex interaction. Nowadays, plenty of microscopy techniques and image analysis methods have been invented to serve these needs. However, quite often, it is necessary to improve existing instruments or create a new one to untangle yet another conundrum in host-pathogen interactions.

The current thesis is focused on developing analytical tools for quantitative analysis of the interaction of human neutrophils with three pathogenic fungi *(Candida albicans, C. glabrata* and *Aspegilus fumigatus),* which together cause the majority of invasive fungal disease cases.

The first part of the work is devoted to analysing neutrophil morphodynamics alteration caused by either *C. albicans* or *C. glabrata.* During microscopy examination of neutrophils isolated from the blood after whole blood infection assay with one of those two pathogens, it was found that neutrophils affected by those fungal pathogens exhibit a spreading morphology more often than neutrophils from mock-infected samples. More-over, neutrophils from *C. glabrata* - infected samples tend to be in spreading mode for a more extended time interval in comparison to those infected with *C. albicans* . To measure these effects quantitatively, a novel workflow algorithm was invented (Belyaev *et al.,* 2022).

In the first step, neutrophils need to be segmented and tracked. For this purpose, we deeply redesigned the Algorithm for Migration and Interaction Tracking (AMIT, (Brandes *et al.,* 2015, 2017; Al-Zaben *et al.,* 2019)) and made it capable of handling transmitted light microscopy data of a cell population with a continuous spectrum of morphological sates. This was achieved via (i) replacement of segmentation based on Gaussian mixtures models by morphological enhancement followed by thresholding of an image local intensity standard deviation map, and (ii) implementation of fusion-and-fission cluster detection and splitting subroutine. The modified algorithm (Belyaev *et al.,* 2021) has shown a noticeable improvement in cell detection and tracking quality in our in-house

data and demonstrated a moderate performance on public data sets. In addition to improved performance, AMIT-v3 has a low computational cost and, therefore, can be executed on an average workstation or even a laptop, which makes it suitable for imaging data from high throughput experiments and makes it a method of choice for quick exploratory analysis of new experimental setups.

In the second step, every neutrophil in each sample was described using the morphology-focused feature extraction paradigm. To identify neutrophil morphological state in each time point, the one class classifier and several morphological descriptors were used (Belyaev *et al.,* 2022). With this approach, we quantitatively described neutrophil morphodynamics and confirmed the observed difference after *in vitro* whole blood infec-tion assay with either *C. albicans* or *C. glabrata* . In addition, we demonstrated a way to use this measurable difference to distinguish between neutrophil populations affected by two close *Candida* species. Additional experiments are necessary to understand how this effect is distributed across the general human population and what changes could be detect in the neutrophil populations of real patients.

The final part of this thesis is devoted to the quantitative analysis of the antifun-gal activity of fungal-induced neutrophil-derived extracellular vesicles (afEVs) against *A. fumigatus.* In particular, using 2D time-lapse transmitted light microscopy in con-junction with automated image analysis, we demonstrated that afEVs inhibit hyphae development. However, this effect is concentration and donor-dependent due to variation of afEVs composition. In addition, using 4D fluorescence microscopy followed by recon-struction of 3D sample structure and quantitative analysis, we have shown that afEVs could erode hyphae cell wall, leading to cytoplasm leakage and osmotic collapse of hyphae. The hyphae erosion and collapse were additionally proven using scanning electron microscopy.

All presented workflow algorithms and tracking software could be used in other projects with minimal adjustment. However, the results of the presented projects were acquired for entirely artificial conditions, which cannot replicate infection processes and immune reactions in the human organism. Future experiments must be conducted using ‘body-on-chips’ multi-organ systems and artificial-intelligence-guided imaging. Such an approach would extend knowledge about fungal disease development on different organ-isational scales (local group of cells — tissue — organ — organism) simultaneously. Then acquired results would have a higher potential for translation into clinical practice.

6 Zusammenfassung

Die steigende Zahl invasiver Pilzinfektionen erhöht die Belastung für die Gesundheitssysteme weltweit. Eine angemessene Diagnostik, Heilung und Prävention er-fordern ein tiefes Verständnis der Interaktion pathogener Pilze mit dem menschlichen Organismus. Ein infektiöser Prozess entfaltet sich in der Zeit und auf verschiedenen räumlichen Ebenen - gewebebezogen, zellulär und molekular. Die mikroskopische Bildgebung mit anschließender automatisierter Bildanalyse ist zu einem unersetzlichen Instrument für die Entdeckung der räumlich-zeitlichen Aspekte dieser komplexen In-teraktion geworden. Heutzutage gibt es eine Vielzahl von Mikroskopietechniken und Bildanalyseverfahren, die diesen Anforderungen gerecht werden. Oftmals ist es jedoch notwendig, bestehende Instrumente zu verbessern oder neue zu entwickeln, um ein weiteres Rätsel der Wirt-Pathogen-Interaktionen zu lösen.

In der vorliegenden Arbeit geht es um die Entwicklung von Analyseinstrumenten für die quantitative Analyse der Interaktion menschlicher Neutrophiler mit drei path-ogenen Pilzen (*C. albicans, C. glabrata* und *A. fumigatus*), die zusammen die meisten invasiven Pilzerkrankungen verursachen.

Der erste Teil der Arbeit befasst sich mit der Analyse der durch *C. albicans* oder *C. glabrata* verursachten Veränderungen der Morphodynamik der Neutrophilen. Bei der mikroskopischen Untersuchung von Neutrophils, die nach einem Vollblutinfek-tionstest mit einem dieser beiden Erreger aus dem Blut isoliert wurden, wurde fest-gestellt, dass Neutrophils, die von diesen Pilzerregern befallen sind, häufiger eine spreizende Morphologie aufweisen als Neutrophils aus mock-infizierten Proben. Darüber hinaus neigen Neutrophils aus mit *C. glabrata* infizierten Proben im Vergleich zu mit *C. albicans* infizierten Proben dazu, sich über einen längeren Zeitraum auszubreiten. Um diese Effekte quantitativ zu messen, wurde ein neuer Workflow-Al-gorithmus entwickelt (Belyaev *et al.,* 2022).

Im ersten Schritt müssen die Neutrophils segmentiert und verfolgt werden. Zu diesem Zweck haben wir den Algorithmus für Migration und Interaktionsverfolgung (AMIT, (Brandes *et al.,* 2015, 2017; Al-Zaben *et al.,* 2019)) grundlegend überarbeitet und ihn in die Lage versetzt, Durchlichtmikroskopiedaten einer Zellpopulation mit einem kontinuierlichen Spektrum morphologischer Zustände zu verarbeiten. Dies wurde erreicht durch (i) den Ersatz der Segmentierung auf der Grundlage von Gaußschen Mischungsmodellen durch morphologische Verbesserung, gefolgt von einer

Schwellen-wertberechnung einer Karte der lokalen Intensitätsstandardabweichung eines Bildes, und (ii) die Implementierung einer Unterroutine zur Erkennung von Clustern durch Fusion und Spaltung. Der geänderte Algorithmus (Belyaev *et al.,* 2021) hat die Qualität der Zellerkennung und -verfolgung in unseren eigenen Daten deutlich verbessert und eine mäßige Leistung in öffentlichen Datensätzen gezeigt. Zusätzlich zur verbesserten Leistung hat AMIT-v3 einen geringen Rechenaufwand und kann daher auf einer durchschnittlichen Workstation oder sogar einem Laptop ausgeführt werden, was es für die Abbildung von Daten aus Experimenten mit hohem Durchsatz geeignet macht und es zu einer Methode der Wahl für die schnelle Sondierungsanalyse neuer Versuchsauf-bauten macht.

Im zweiten Schritt wurde jede PMN in jeder Probe mithilfe des Paradigmas der morphologieorientierten Merkmalsextraktion beschrieben. Um den morphologischen Zustand der Neutrophilen zu jedem Zeitpunkt zu bestimmen, wurden ein Klassifikator und mehrere morphologische Deskriptoren verwendet (Belyaev et. al., 2022). Mit diesem Ansatz konnten wir die Morphodynamik der PMN quantitativ beschreiben und die beobachteten Unterschiede nach einem In-vitro-Vollblutinfektionstest mit *C. albicans* oder *C. glabrata* bestätigen. Darüber hinaus haben wir eine Möglichkeit aufgezeigt, diesen messbaren Unterschied zu nutzen, um zwischen neutrophilen Populationen zu unterscheiden, die von zwei nahe beieinander liegenden Candida-Spezies befallen werden. Weitere Experimente sind notwendig, um zu verstehen, wie dieser Effekt in der allgemeinen menschlichen Bevölkerung verteilt ist und welche Veränderungen in den Neutrophilenpopulationen echter Patienten festgestellt werden könnten.

Der letzte Teil dieser Arbeit widmet sich der quantitativen Analyse der antimy-kotischen Aktivität von pilzinduzierten, neutrophilen extrazellulären Vesikeln (afEVs) gegen *A. fumigatus*. Insbesondere konnten wir mit Hilfe der 2D-Zeitraffer-Durchlicht-mikroskopie in Verbindung mit einer automatisierten Bildanalyse zeigen, dass afEVs die Hyphenentwicklung hemmen. Dieser Effekt ist jedoch konzentrations- und do-norabhängig, da die Zusammensetzung der afEVs variiert. Mit Hilfe der 4D-Fluo-reszenzmikroskopie, gefolgt von der Rekonstruktion der 3D-Probenstruktur und der quantitativen Analyse, konnten wir außerdem zeigen, dass afEVs die Zellwand der Hyphen erodieren können, was zum Austreten von Zytoplasma und zum osmotischen Kollaps der Hyphen führt. Die Erosion und der Kollaps der Hyphen wurden zusätzlich mit Hilfe der Rasterelektronen-mikroskopie nachgewiesen.

Alle vorgestellten Workflow-Algorithmen und Tracking-Software könnten mit minimalen Anpassungen auch in anderen Projekten eingesetzt werden. Allerdings wurden die Ergebnisse der vorgestellten Projekte unter völlig künstlichen Bedingungen gewonnen, die die Infektionsprozesse und Immunreaktionen im menschlichen Organis-mus nicht nachbilden können. Künftige Experimente müssen unter Verwendung von "Body-on-Chips"-Multi-Organ-Systemen und mit Hilfe von künstlicher Intelligenz ges-teuerter Bildgebung durchgeführt werden. Ein solcher Ansatz würde das Wissen über die Entwicklung von Pilzkrankheiten auf verschiedenen organisatorischen Ebenen (lokale Zellgruppe — Gewebe — Organ — Organismus) gleichzeitig erweitern. Die gewonnenen Ergebnisse hätten dann ein größeres Potenzial für die Umsetzung in die klinische Praxis.

Bibliography

A – Bir

Al-Zaben N., Medyukhina A., Dietrich S., Marolda A., Hünniger K., Kurzai O., Figge M.T. Automated tracking of label-free cells with enhanced recognition of whole tracks. Sci Rep, 2019; 9(1): 3317.

Allen E.R., Lempke S.L., Miller M.M., Bush D.M., Braswell B.G., Estes C.L., Benedict E.L., Mahon A.R., Sabo S.L., Greenlee-Wacker M.C. Effect of extracellular vesicles from *S. aureus*-challenged human neutrophils on macrophages. J Leukoc Biol, 2020; 108(6): 1841–50.

Allen R.D., David G.B., Nomarski G. The Zeiss-Nomarski differential interference equipment for transmitted-light microscopy. Z Wiss Mikrosk, 1969; 69(4): 193–221.

Almeida F., Rodrigues M.L., Coelho C. The Still Underestimated Problem of Fungal Diseases Worldwide. Front Microbiol, 2019; 10: 214.

Amulic B., Cazalet C., Hayes G.L., Metzler K.D., Zychlinsky A. Neutrophil function: from mechanisms to disease. Annu Rev Immunol, 2012; 30: 459–89.

Barry D.J., Durkin C.H., Abella J. V, Way M. Open source software for quantification of cell migration, protrusions, and fluorescence intensities. J Cell Biol, 2015; 209(1): 163–80.

Basile K., Halliday C., Kok J., Chen S.C.A. Fungal Infections Other Than Invasive Aspergillosis in COVID-19 Patients. J Fungi, 2022; 8(1): 58.

Beltman J.B., Marée A.F.M., de Boer R.J. Analysing immune cell migration. Nat Rev Immunol, 2009; 9(11): 789–98.

Belyaev I., Marolda A., Praetorius J.P., Sarkar A., Medyukhina A., Hünniger K., Kurzai O., Figge M.T. Automated characterisation of neutrophil activation phenotypes in *ex vivo* human *Candida* blood infections. Comput Struct Biotechnol J, 2022; 20: 2297–308.

Belyaev I., Praetorius J., Medyukhina A., Figge M.T. Enhanced segmentation of label-free cells for automated migration and interaction tracking. Cytom Part A, 2021; 99(12): 1218–29.

Birch D., Christensen M.V., Staerk D., Franzyk H., Nielsen H.M. Fluorophore labeling of a cell-penetrating peptide induces differential effects on its cellular distribution and affects cell viability. Biochim Biophys Acta - Biomembr, 2017; 1859(12): 2483–94.

Bon – Con

Bongomin F., Gago S., Oladele R., Denning D. Global and Multi-National Prevalence of Fungal Diseases—Estimate Precision. J Fungi, 2017; 3(4): 57.

Brakhage A.A., Zimmermann A.K., Rivieccio F., Visser C., Blango M.G. Host-derived extracellular vesicles for antimicrobial defense. microLife, 2021; 2(2): uqab003.

Brandes S., Dietrich S., Hünniger K., Kurzai O., Figge M.T. Migration and interaction tracking for quantitative analysis of phagocyte–pathogen confrontation assays. Med Image Anal, 2017; 36: 172–83.

Brandes S., Mokhtari Z., Essig F., Hünniger K., Kurzai O., Figge M.T. Automated segmentation and tracking of non-rigid objects in time-lapse microscopy videos of polymorphonuclear neutrophils. Med Image Anal, 2015; 20(1): 34–51.

Brinkmann V., Reichard U., Goosmann C., Fauler B., Uhlemann Y., Weiss D.S., Weinrauch Y., Zychlinsky A. Neutrophil Extracellular Traps Kill Bacteria. Science (80-), 2004; 303(5663): 1532–5.

Brown G.D., Denning D.W., Gow N.A.R., Levitz S.M., Netea M.G., White T.C. Hidden Killers: Human Fungal Infections. Sci Transl Med, 2012; 4(165): 165rv13.

Brunke S., Hube B. Two unlike cousins: *Candida albicans* and *C. glabrata* infection strategies. Cell Microbiol, 2013; 15(5): 701–8.

Buil J.B., Meijer E.F.J., Denning D.W., Verweij P.E., Meis J.F. Burden of serious fungal infections in the Netherlands. Mycoses, 2020; 63(6): 625–31.

Casalini G., Giacomelli A., Ridolfo A., Gervasoni C., Antinori S. Invasive Fungal Infections Complicating COVID-19: A Narrative Review. J Fungi, 2021; 7(11): 921.

Cavaco M., Pérez-Peinado C., Valle J., Silva R.D.M., Correia J.D.G., Andreu D., Castanho M.A.R.B., Neves V. To What Extent Do Fluorophores Bias the Biological Activity of Peptides? A Practical Approach Using Membrane-Active Peptides as Models. Front Bioeng Biotechnol, 2020; 8: 1059.

Clancy C.J., Nguyen M.H. Diagnosing candidemia with the T2Candida panel: an instructive case of septic shock in which blood cultures were negative. Diagn Microbiol Infect Dis, 2019; 93(1): 54–7.

Clancy C.J., Pappas P.G., Vazquez J., Judson M.A., Kontoyiannis D.P., Thompson G.R., Garey K.W., Reboli A., Greenberg R.N., Apewokin S., Lyon G.M., Ostrosky-Zeichner L., Wu A.H.B., Tobin E., Nguyen M.H., *et al.,* Detecting Infections Rapidly and Easily for Candidemia Trial, Part 2 (DIRECT2): A Prospective, Multicenter Study of the T2Candida Panel. Clin Infect Dis, 2018; 66(11): 1678–86.

Consortium OPATHY, Gabaldón T. Recent trends in molecular diagnostics of yeast infections: from PCR to NGS. FEMS Microbiol Rev, 2019; 43(5): 517–47.

Cse – Goo

Cseresnyes Z., Hassan M.I.A., Dahse H.M., Voigt K., Figge M.T. Quantitative Impact of Cell Membrane Fluorescence Labeling on Phagocytosis Measurements in Confrontation Assays. Front Microbiol, 2020; 11: 1193.

Dixit R., Cyr R. Cell damage and reactive oxygen species production induced by fluorescence microscopy: effect on mitosis and guidelines for non-invasive fluorescence microscopy. Plant J, 2003; 36(2): 280–90.

Donnelly J.P., Chen S.C., Kauffman C.A., Steinbach W.J., Baddley J.W., Verweij P.E., Clancy C.J., Wingard J.R., Lockhart S.R., Groll A.H., Sorrell T.C., Bassetti M., Akan H., Alexander B.D., Andes D., *et al.,* Revision and Update of the Consensus Definitions of Invasive Fungal Disease From the European Organization for Research and Treatment of Cancer and the Mycoses Study Group Education and Research Consortium. Clin Infect Dis, 2020; 71(6): 1367–76.

Driscoll M.K., Fourkas J.T., Losert W. Local and global measures of shape dynamics. Phys Biol, 2011; 8(5): 055001.

Duggan S., Essig F., Hünniger K., Mokhtari Z., Bauer L., Lehnert T., Brandes S., Häder A., Jacobsen I.D., Martin R., Figge M.T., Kurzai O. Neutrophil activation by *Candida glabrata* but not *Candida albicans* promotes fungal uptake by monocytes. Cell Microbiol, 2015; 17(9): 1259–76.

Enoch D.A., Yang H., Aliyu S.H., Micallef C. The Changing Epidemiology of Invasive Fungal Infections. In: Lion T, editor. Human Fungal Pathogen Identification, 1st ed. NY: Humana Press, New York; 2017. p. 17–65.

Felten D.L., Ackerman K.D., Wiegand S.J., Felten S.Y. Noradrenergic sympathetic innervation of the spleen: I. Nerve fibers associate with lymphocytes and macrophages in specific compartments of the splenic white pulp. J Neurosci Res, 1987; 18(1): 28–36.

Fisher M.C., Gow N.A.R., Gurr S.J. Tackling emerging fungal threats to animal health, food security and ecosystem resilience. Philos Trans R Soc B Biol Sci, 2016; 371(1709): 20160332.

Fraser J.A., Kemp S., Young L., Ross M., Prach M., Hutchison G.R., Malone E. Silver nanoparticles promote the emergence of heterogeneic human neutrophil subpopulations. Sci Rep, 2018; 8(1): 1–14.

Godinho-Silva C., Cardoso F., Veiga-Fernandes H. Neuro–Immune Cell Units: A New Paradigm in Physiology. Annu Rev Immunol, 2019; 37(1): 19–46.

Gonzalez R.C., Woods R.E. Digital Image Processing. 4th ed. Pearson; 2018.

Goodfellow I., Bengio Y., Courville A. Deep Learning. MIT Press; 2016.

Gor – Ing

Gordonov S., Hwang M.K., Wells A., Gertler F.B., Lauffenburger D.A., Bathe M. Time series modeling of live-cell shape dynamics for image-based phenotypic profiling. Integr Biol, 2016; 8(1): 73–90.

Hawksworth D.L., Lücking R. Fungal Diversity Revisited: 2.2 to 3.8 Million Species. Microbiol Spectr, 2017; 5(4).

Held M., Schmitz M.H.A., Fischer B., Walter T., Neumann B., Olma M.H., Peter M., Ellenberg J., Gerlich D.W. CellCognition: time-resolved phenotype annotation in high-throughput live cell imaging. Nat Methods, 2010; 7(9): 747–54.

Hidalgo A., Chilvers E.R., Summers C., Koenderman L. The Neutrophil Life Cycle. Trends Immunol, 2019; 40(7): 584–97.

Hind L.E., Vincent W.J.B., Huttenlocher A. Leading from the Back: The Role of the Uropod in Neutrophil Polarization and Migration. Dev Cell, 2016; 38: 161–9.

Hoang T.N.M., Cseresnyés Z., Hartung S., Blickensdorf M., Saffer C., Rennert K., Mosig A.S., von Lilienfeld-Toal M., Figge M.T. Invasive aspergillosis-on-chip: A quantitative treatment study of human *Aspergillus fumigatus* infection. Biomaterials, 2022; 283: 121420.

Hong C.W. Current Understanding in Neutrophil Differentiation and Heterogeneity. Immune Netw, 2017; 17(5): 298–306.

Hong C.W. Extracellular Vesicles of Neutrophils. Immune Netw, 2018; 18(6): e43.

Horobin R. Biological staining: mechanisms and theory. Biotech Histochem, 2002; 77(1): 3–13.

Hughes S., Troise O., Donaldson H., Mughal N., Moore L.S.P. Bacterial and fungal coinfection among hospitalized patients with COVID-19: a retrospective cohort study in a UK secondary-care setting. Clin Microbiol Infect, 2020; 26(10): 1395–9.

Hünniger K., Lehnert T., Bieber K., Martin R., Figge M.T., Kurzai O. A Virtual Infection Model Quantifies Innate Effector Mechanisms and Candida albicans Immune Escape in Human Blood. PLoS Comput Biol, 2014; 10(2): e1003479.

Huse M. Mechanical forces in the immune system. Nat Rev Immunol, 2017; 17(11): 679–90.

Imoto D., Saito N., Nakajima A., Honda G., Ishida M., Sugita T., Ishihara S., Katagiri K., Okimura C., Iwadate Y., Sawai S. Comparative mapping of crawling-cell morphodynamics in deep learning-based feature space. PLOS Comput Biol, 2021; 17(8): e1009237.

Ingber D.E. Human organs-on-chips for disease modelling, drug development and personalized medicine. Nat Rev Genet 2022, 2022; 1–25.

Inv – Lan

invitrogen. Propidium Iodide Nucleic Acid Stain [Online]. invitrogen. 2006 [accessed 2022 Mar 10]. Available from: https://www.thermofisher.com/document-connect/document-connect.html?url=https%3A%2F%2Fassets.thermofisher.com%2FTFS-Assets%2FLSG%2Fmanuals%2Fmp01304.pdf

Jensen E.C. Use of Fluorescent Probes: Their Effect on Cell Biology and Limitations. Anat Rec Adv Integr Anat Evol Biol, 2012; 295(12): 2031–6.

Johnson C.J., Cabezas-Olcoz J., Kernien J.F., Wang S.X., Beebe D.J., Huttenlocher A., Ansari H., Nett J.E. The Extracellular Matrix of *Candida albicans* Biofilms Impairs Formation of Neutrophil Extracellular Traps. PLOS Pathog, 2016; 12(9): e1005884.

Johnson C.J., Kernien J.F., Hoyer A.R., Nett J.E. Mechanisms involved in the triggering of neutrophil extracellular traps (NETs) by *Candida glabrata* during planktonic and biofilm growth. Sci Rep, 2017; 7(1): 13065.

Kato T., Makino F., Nakane T., Terahara N., Kaneko T., Shimizu Y., Motoki S., Ishikawa I., Yonekura K., Namba K. CryoTEM with a Cold Field Emission Gun That Moves Structural Biology into a New Stage. Microsc Microanal, 2019; 25(S2): 998–9.

Kedziora K.M., Prehn J.H.M., Dobrucki J., Bernas T. Method of calibration of a fluorescence microscope for quantitative studies. J Microsc, 2011; 244(1): 101–11.

Kenney M.J., Ganta C.K. Autonomic nervous system and immune system interactions. Compr Physiol, 2014; 4(3): 1177–200.

Kernien J.F., Johnson C.J., Bayless M.L., Chovanec J.F., Nett J.E. Neutrophils From Patients With Invasive Candidiasis Are Inhibited by *Candida albicans* Biofilms. Front Immunol, 2020; 11: 3179.

Kim J., Koo B.K., Knoblich J.A. Human organoids: model systems for human biology and medicine. Nat Rev Mol Cell Biol, 2020; 21(10): 571–84.

Köhler J.R., Hube B., Puccia R., Casadevall A., Perfect J.R. Fungi that Infect Humans. Heitman J, Howlett BJ, editors. Microbiol Spectr, 2017; 5(3).

Kolaczkowska E., Kubes P. Neutrophil recruitment and function in health and inflammation. Nat Rev Immunol, 2013; 13(3): 159–75.

Kolonics F., Szeifert V., Timár C.I., Ligeti E., Lőrincz Á.M. The Functional Heterogeneity of Neutrophil-Derived Extracellular Vesicles Reflects the Status of the Parent Cell. Cells, 2020; 9(12): 2718.

Lang W. Nomarski Differential Interference-Contrast Microscopy. What's New ZEISS, 1971; 76: 69–76.

Las – Mok

Lass-Flörl C., Samardzic E., Knoll M. Serology anno 2021—fungal infections: from invasive to chronic. Clin Microbiol Infect, 2021; 27(9): 1230–41.

Latgé J.P. Aspergillus fumigatus and Aspergillosis. Clin Microbiol Rev, 1999; 12(2): 310–50.

Latgé J.P., Chamilos G. *Aspergillus fumigatus* and Aspergillosis in 2019. Clin Microbiol Rev, 2019; 33(1).

Leliefeld P.H.C., Koenderman L., Pillay J. How Neutrophils Shape Adaptive Immune Responses. Front Immunol, 2015; 6: 471.

Letendre K., Donnadieu E., Moses M.E., Cannon J.L. Bringing Statistics Up to Speed with Data in Analysis of Lymphocyte Motility. PLoS One, 2015; 10(5): e0126333.

Ley K., Hoffman H.M., Kubes P., Cassatella M.A., Zychlinsky A., Hedrick C.C., Catz S.D. Neutrophils: New insights and open questions. Sci Immunol, 2018; 3(30): eaat4579.

von Lilienfeld-Toal M., Wagener J., Einsele H., Cornely O.A., Kurzai O. Invasive Fungal Infection. Dtsch Aerzteblatt Online, 2019; 116(16): 271–8.

Logan C., Martin-Loeches I., Bicanic T. Invasive candidiasis in critical care: challenges and future directions. Intensive Care Med, 2020; 46(11): 2001–14.

Ma X., Dagliyan O., Hahn K.M., Danuser G. Profiling cellular morphodynamics by spatiotemporal spectrum decomposition. PLOS Comput Biol, 2018; 14(8): e1006321.

Machacek M., Danuser G. Morphodynamic profiling of protrusion phenotypes. Biophys J, 2006; 90(4): 1439–52.

Maza P.K., Bonfim-Melo A., Padovan A.C.B., Mortara R.A., Orikaza C.M., Ramos L.M.D., Moura T.R., Soriani F.M., Almeida R.S., Suzuki E., Bahia D. *Candida albicans*: The Ability to Invade Epithelial Cells and Survive under Oxidative Stress Is Unlinked to Hyphal Length. Front Microbiol, 2017; 8: 1235.

Meijering E. A chronology of interpolation: From ancient astronomy to modern signal and image processing. Proc IEEE, 2002; 90(3): 319–42.

Mignot C. Color (and 3D) for Scanning Electron Microscopy. Micros Today, 2018; 26(3): 12–7.

Mokhtari Z., Mech F., Zitzmann C., Hasenberg M., Gunzer M., Figge M.T. Automated Characterization and Parameter-Free Classification of Cell Tracks Based on Local Migration Behavior. PLoS One, 2013; 8(12): e80808.

Mur – Pfe

Murphy D.B., Davidson M.W. Fluorescence Microscopy. In: Fundamentals of Light Microscopy and Electronic Imaging, 2nd ed. Hoboken, NJ, USA: John Wiley & Sons, Inc.; 2012a. p. 199–231. (Wiley Online Books).

Murphy D.B., Davidson M.W. Polarization Microscopy. In: Fundamentals of Light Microscopy and Electronic Imaging, 2nd ed. Hoboken, NJ, USA: John Wiley & Sons, Inc.; 2012b. p. 153–71. (Wiley Online Books).

Murphy D.B., Hoffman R., Spring K.R., Davidson M.W. Specimen Contrast in Optical Microscopy [Online]. Nikon Instruments Inc. 2022 [accessed 2022 May 10]. Available from: https://www.microscopyu.com/techniques/phase-contrast/specimen-contrast-in-optical-microscopy

Murphy K.M., Weaver C. Janeway's Immunobiology: Ninth International Student Edition. Garland Science, Taylor \& Francis Group, LLC; 2016.

Mylonakis E., Clancy C.J., Ostrosky-Zeichner L., Garey K.W., Alangaden G.J., Vazquez J.A., Groeger J.S., Judson M.A., Vinagre Y.M., Heard S.O., Zervou F.N., Zacharioudakis I.M., Kontoyiannis D.P., Pappas P.G. T2 Magnetic Resonance Assay for the Rapid Diagnosis of Candidemia in Whole Blood: A Clinical Trial. Clin Infect Dis, 2015; 60(6): 892–9.

Nicolás-Ávila J.Á., Adrover J.M., Hidalgo A. Neutrophils in Homeostasis, Immunity, and Cancer. Immunity, 2017; 46(1): 15–28.

Van Niel G., D'Angelo G., Raposo G. Shedding light on the cell biology of extracellular vesicles. Nat Rev Mol Cell Biol 2018 194, 2018; 19(4): 213–28.

Nomarski G. Microinterferometre differentiel a ondes polarisees. J Phys Rad, 1955; 16: 9S-13S.

Nomarski G. Interferential polarizing device for study of phase objects. US Pat. No. 2924142. 1960. p. 3.

North A.J. Seeing is believing? A beginners' guide to practical pitfalls in image acquisition. J Cell Biol, 2006; 172(1): 9–18.

Nucci M., Barreiros G., Guimarães L.F., Deriquehem V.A.S., Castiñeiras A.C., Nouér S.A. Increased incidence of candidemia in a tertiary care hospital with the COVID-19 pandemic. Mycoses, 2021; 64(2): 152–6.

Pfeiffer C.D., Samsa G.P., Schell W.A., Reller L.B., Perfect J.R., Alexander B.D. Quantitation of Candida CFU in Initial Positive Blood Cultures. J Clin Microbiol, 2011; 49(8): 2879–83.

Pic – Sil

Picollet-D'hahan N., Zuchowska A., Lemeunier I., Le Gac S. Multiorgan-on-a-Chip: A Systemic Approach To Model and Decipher Inter-Organ Communication. Trends Biotechnol, 2021; 39(8): 788–810.

Pillay J., Ramakers B.P., Kamp V.M., Loi A.L.T., Lam S.W., Hietbrink F., Leenen L.P., Tool A.T., Pickkers P., Koenderman L. Functional heterogeneity and differential priming of circulating neutrophils in human experimental endotoxemia. J Leukoc Biol, 2010; 88(1): 211–20.

Pomerantsev A.L. Acceptance areas for multivariate classification derived by projection methods. J Chemom, 2008; 22(11–12): 601–9.

Pomerantsev A.L., Rodionova O.Y. Concept and role of extreme objects in PCA/SIMCA. J Chemom, 2014; 28(5): 429–38.

Resch-Genger U., DeRose P.C. Fluorescence standards: Classification, terminology, and recommendations on their selection, use, and production (IUPAC Technical Report). Pure Appl Chem, 2010; 82(12): 2315–35.

Richard W. Dapson, Richard W. Horobin, John A. Kiernan. Glossary of Staining Methods, Reagents, Immunostaining, Terminology and Eponyms [Online]. 2021 [accessed 2021 Apr 7]. Available from: https://biologicalstaincommission.org/bscglossary.html

Rodrigues M.L., Nosanchuk J.D. Fungal diseases as neglected pathogens: A wake-up call to public health officials. PLoS Negl Trop Dis, 2020; 14(2): e0007964.

Ruhnke M., Groll A.H., Mayser P., Ullmann A.J., Mendling W., Hof H., Denning D.W. Estimated burden of fungal infections in Germany. Mycoses, 2015; 58: 22–8.

Russell A.E., Sneider A., Witwer K.W., Bergese P., Bhattacharyya S.N., Cocks A., Cocucci E., Erdbrügger U., Falcon-Perez J.M., Freeman D.W., Gallagher T.M., Hu S., Huang Y., Jay S.M., Kano S., *et al.,* Biological membranes in EV biogenesis, stability, uptake, and cargo transfer: an ISEV position paper arising from the ISEV membranes and EVs workshop. J Extracell Vesicles, 2019; 8(1): 1684862.

Salazar F., Brown G.D. Antifungal Innate Immunity: A Perspective from the Last 10 Years. J Innate Immun, 2018; 10(5–6): 373–97.

Shopova I.A., Belyaev I., Dasari P., Jahreis S., Stroe M.C., Cseresnyés Z., Zimmermann A.K., Medyukhina A., Svensson C.M., Krüger T., Szeifert V., Nietzsche S., Conrad T., Blango M.G., Kniemeyer O., von Lilienfeld-Toal M., Zipfel P. F., Ligeti E., Figge M. T., Brakhage A. A. Human Neutrophils Produce Antifungal Extracellular Vesicles against Aspergillus fumigatus. Pietro A Di, editor. MBio, 2020; 11(2).

Silvestre-Roig C., Hidalgo A., Soehnlein O. Neutrophil heterogeneity: Implications for homeostasis and pathogenesis. Blood, 2016; 127(18): 2173–81.

Sta – Wor

Stanzani M., Orciuolo E., Lewis R., Kontoyiannis D.P., Martins S.L.R., St. John L.S., Komanduri K. V. Aspergillus fumigatus suppresses the human cellular immune response via gliotoxin-mediated apoptosis of monocytes. Blood, 2005; 105(6): 2258–65.

Stringer C., Wang T., Michaelos M., Pachitariu M. Cellpose: a generalist algorithm for cellular segmentation. Nat Methods, 2021; 18(1): 100–6.

Suzuki T., Fujikura K., Higashiyama T., Takata K. DNA staining for fluorescence and laser confocal microscopy. J Histochem Cytochem, 1997; 45(1): 49–53.

Svensson C.M., Medyukhina A., Belyaev I., Al-Zaben N., Figge M.T. Untangling cell tracks: Quantifying cell migration by time lapse image data analysis. Cytom Part A, 2018; 93(3): 357–70.

Tak T., Wijten P., Heeres M., Pickkers P., Scholten A., Heck A.J.R., Vrisekoop N., Leenen L.P., Borghans J.A.M., Tesselaar K., Koenderman L. Human CD62Ldim neutrophils identified as a separate subset by proteome profiling and in vivo pulse-chase labeling. Blood, 2017; 129(26): 3476–85.

Taylor H.B., Liepe J., Barthen C., Bugeon L., Huvet M., Kirk P.D., Brown S.B., Lamb J.R., Stumpf M.P., Dallman M.J. P38 and JNK have opposing effects on persistence of in vivo leukocyte migration in zebrafish. Immunol Cell Biol, 2013; 91(1): 60–9.

Tsygankov D., Bilancia C.G., Vitriol E.A., Hahn K.M., Peifer M., Elston T.C. CellGeo: A computational platform for the analysis of shape changes in cells with complex geometries. J Cell Biol, 2014; 204(3): 443–60.

Urban C.F., Reichard U., Brinkmann V., Zychlinsky A. Neutrophil extracellular traps capture and kill Candida albicans yeast and hyphal forms. Cell Microbiol, 2006; 8(4): 668–76.

Waibel D.J.E., Shetab Boushehri S., Marr C. InstantDL: an easy-to-use deep learning pipeline for image segmentation and classification. BMC Bioinformatics, 2021; 22(1): 1–15.

Weisenburger S., Boening D., Schomburg B., Giller K., Becker S., Griesinger C., Sandoghdar V. Cryogenic optical localization provides 3D protein structure data with Angstrom resolution. Nat Methods, 2017; 14(2): 141–4.

Wéry N. Bioaerosols from composting facilities — a review. Front Cell Infect Microbiol, 2014; 4.

World Health Organization (WHO). International Classification of Diseases, Tenth Revision (ICD-10) [Online]. 1994 [accessed 2022 Feb 17]. Available from: https://icd.who.int/browse10/2019/en

Wor – Z

World Health Organization (WHO). International Classification of Diseases, Eleventh Revision (ICD-11) [Online]. 2019 [accessed 2022 Feb 17]. Available from: https://icd.who.int/browse11/l-m/en

Yamashiro S., Kamohara H., Wang J.M., Yang D., Gong W.H., Yoshimura T. Phenotypic and functional change of cytokine-activated neutrophils: inflammatory neutrophils are heterogeneous and enhance adaptive immune responses. J Leukoc Biol, 2001; 69(5): 698–704.

Yang P., Li Y., Xie Y., Liu Y. Different Faces for Different Places: Heterogeneity of Neutrophil Phenotype and Function. J Immunol Res, 2019; 2019: 1–18.

Zernike F. The concept of degree of coherence and its application to optical problems. Physica, 1938; 5(8): 785–95.

Zernike F. Phase contrast, a new method for the microscopic observation of transparent objects part II. Physica, 1942; 9(10): 974–86.

Declaration on honour

I hereby confirm that I am familiar with the valid doctoral examination regula-tions of the Faculty of Biological Sciences and that I have adhered to these regulations to the best of my knowledge. I have prepared this dissertation independently and only using the indicated tools, personal communications, data and sources. The persons who assisted me in selecting and analysing the data, preparing paper manuscripts and the dissertation's text are named as co-authors and in the acknowledgements. I have not used any assistance from external intermediaries or consulting services. No one has received any direct or indirect pecuniary benefits for the work related to the content of the dissertation presented. The dissertation presented has not been submitted as an examination material for any other state or academic examination. In particular, I have not submitted this dissertation or its fragments, nor other dissertation, to another university or faculty to acquire an academic degree.

_____/ Ivan Belyaev

Acknowledgements

I would like to extend my sincere thanks to my supervisor Prof. Dr Marc Thilo Figge, for accepting me as a doctoral student, for providing me with the challenging and interesting projects and for the opportunity to carry out my work at the Hans-Knöll-Institut in the Applied Systems Biology group. You supervised with a great engagement; the valuable suggestions and advice that I always appreciated, were complemented with freedom for my ideas.

I also wish to thank Prof. Dr Oliver Kurzai and Dr Anna Medyukhina for co-supervising this thesis.

I would also like to acknowledge the Jena School for Microbial Communication (JSMC) and the Friedrich Schiller University Jena for accepting me as a doctoral stu-dent, and the Leibniz ScienceCampus InfectoOptics in Jena for funding this work.

In addition, I would also like to extend my gratitude to my collaboration partners from the Fungal Septomics group, Dr Kerstin Hünniger and Dr Alessandra Marolda, who performed wet-lab experiments and provided the microscopy data on which the significant part of this work is based.

I appreciate the effort of Jan-Philipp Praetorius in the transfer of my tracking routine prototype into the ready-to-use software.

I am thankful to Dr Iordana Shopova for the informative discussions about neu-trophil biology and productive collaboration on the joint project.

I am grateful to have had discussions in the philosophy and methodology of applied data analysis with Dr Carl-Magnus Svensson and for the knowledge in microscopy received from Dr Zoltán Cseresnyés.

Special thanks to Dr Sergei Kucheryavskiy and Dr Sergei Zhilin, who assisted me in taking the first steps in digital image analysis as well as chemometrics, and influenced my way of thinking.

I would also like to thank all current and former members of the research group Applied Systems Biology and the twin group Systems Biology/Bioinformatics for the many lively discussions, joint events and the creation of a pleasant working environment.

Last but not least, I would also like to express my deepest gratitude to my parents, Lyubov and Alexandr Belyaev, for their patience and support.

Appendix

FORMULAR 2

Manuskript Nr. (laufende Nummer in der Dissertation) **1**

Kurzreferenz [Belyaev *et al.,* (2021), Cyt A.]

Beitrag des Doktoranden / der Doktorandin

Beitrag des Doktoranden / der Doktorandin zu Abbildungen, die experimentelle Daten wiedergeben (nur für Originalartikel):

Abbildung(en) # 1,3,4-6*	☒	100% (die in dieser Abbildung wiedergegebenen Daten entstammen vollständig experimentellen Arbeiten, die der Kandidat/die Kandidatin durchgeführt hat)
	☐	0% (die in dieser Abbildung wiedergegebenen Daten basieren ausschließllich auf Arbeiten anderer Koautoren)
	☐	Etwaiger Beitrag des Doktoranden / der Doktorandin zur Abbildung: _____% Kurzbeschreibung des Beitrages: *(z. B. „Abbildungsteile a, d und f“ oder „Auswertung der Daten“ etc)*
**Kann sich auf mehrere Abb. beziehen, wenn die Antwort dieselbe ist*		

FORMULAR 2

Manuskript Nr. (laufende Nummer in der Dissertation) **2**

Kurzreferenz [Belyaev *et al.,* (2022), Comput Struct Biotechnol J]

Beitrag des Doktoranden / der Doktorandin

Beitrag des Doktoranden / der Doktorandin zu Abbildungen, die experimentelle Daten wiedergeben (nur für Originalartikel):

Abbildung(en) # 2-7*	☒	100% (die in dieser Abbildung wiedergegebenen Daten entstammen vollständig experimentellen Arbeiten, die der Kandidat/die Kandidatin durchgeführt hat)
	☐	0% (die in dieser Abbildung wiedergegebenen Daten basieren ausschließllich auf Arbeiten anderer Koautoren)
	☐	Etwaiger Beitrag des Doktoranden / der Doktorandin zur Abbildung: _____% Kurzbeschreibung des Beitrages: *(z. B. „Abbildungsteile a, d und f“ oder „Auswertung der Daten“ etc)*
**Kann sich auf mehrere Abb. beziehen, wenn die Antwort dieselbe ist*		

FORMULAR 2

Manuskript Nr. (laufende Nummer in der Dissertation) **3**

Kurzreferenz [Shopova *et al.,* (2020), MBio]

Beitrag des Doktoranden / der Doktorandin

Beitrag des Doktoranden / der Doktorandin zu Abbildungen, die experimentelle Daten wiedergeben (nur für Originalartikel):

Abbildung(en) # 3,4,6*	☐	100% (die in dieser Abbildung wiedergegebenen Daten entstammen vollständig experimentellen Arbeiten, die der Kandidat/die Kandidatin durchgeführt hat)
	☐	0% (die in dieser Abbildung wiedergegebenen Daten basieren ausschließllich auf Arbeiten anderer Koautoren)
	☒	Etwaiger Beitrag des Doktoranden / der Doktorandin zur Abbildung: 80 % Kurzbeschreibung des Beitrages: *(z. B. „Abbildungsteile a, d und f“ oder „Auswertung der Daten“ etc)* Design and implementation of image processing workflows for the data extraction.
**Kann sich auf mehrere Abb. beziehen, wenn die Antwort dieselbe ist*		